Surface Structure Probe of Transition Metal-Based Oxygen Evolving Systems with Spectroscopy

by

Hoang Quoc Doan

A dissertation submitted in partial satisfaction of the

requirements for the degree of

Doctor of Philosophy

in

Chemistry

in the

Graduate Division

of the

University of California, Berkeley

Committee in charge:

Assistant Professor Tanja Cuk, Chair
Professor Stephen Leone
Associate Professor Junqiao Wu

Spring 2016

Surface Structure Probe of Transition Metal-Based Oxygen Evolving Systems with Spectroscopy

Abstract

Surface Structure Probe of Transition Metal-Based Oxygen Evolving Systems with Spectroscopy

by

Hoang Quoc Doan

Doctor of Philosophy in Chemistry

University of California, Berkeley

Assistant Professor Tanja Cuk, Chair

The goal of a carbon free H_2 economy using a photoelectrochemical cell to split water is a worthwhile endeavor to solve the looming energy crisis. Many scientists have taken up this cause and an abundance of studies exists characterizing, optimizing, and creating materials to integrate into a full artificial photosynthetic system. However, despite widespread attention, a viable industrial-scaled photoelectrochemical device has yet to emerge due to low efficiencies, slow kinetics, and high energetic barriers. To that end, going back to the fundamentals may be a necessary step to understand what is causing the bottleneck, particularly within the heterogeneous water oxidation catalysts. Herein, the surface electronic structure of transition metal-based semiconductors and their $3d$ valence electrons that actively participate in the oxygen evolution process are investigated using a number of spectroscopic techniques in an effort to unravel the mechanism and uncover important material properties. I focus on three major properties: 1) photo-excited carrier dynamics affecting the excited state electronic structure, 2) ground state electronic structure including covalent and atomic parameters, and 3) surface state-mediated interfacial hole transport.

First, the transient electronic structure of Co_3O_4, a promising water oxidation catalyst, is probed via transient absorption spectroscopy. With selective excitation of key optical transitions, both inter- and intravalence transitions involving the $3d$ electrons, the kinetics and spectrum are investigated. A wide range of pump and probe wavelengths, spanning the ultraviolet to the visible to the near infrared, are employed. Despite this range of pump and probe energies, the carrier dynamics were largely unaffected. Additionally, the kinetics and spectra show a unique independence to fluence and sample morphology. The kinetics reveal a photo-excited carrier density that quickly thermalizes when excited across the charge transfer transitions and converts into $d - d$ excitations. The recombination from these localized midgap d states occurs at a longer, nanosecond time scale. In addition to perturbing the system via photo-excitation, the electronic structure of Co_3O_4 was tuned using an applied potential in a technique called spectroelectrochemistry. Spectroelectrochemistry reinforced the results of the transient absorption spectroscopy and confirmed the identity of the midgap

d states through determination of the energetics of these 3*d* states as well as assignment of whether electrons or holes induced the absorptions or bleaches observed within the transient spectrum. Taken together, the results suggest a special type of intrinsic hole trap center that is a potentially promising long-lived state for utilization in photo-activation. Further, since the photo-excited hole is efficiently localized at these 3*d* sites, the most likely water oxidation reaction intermediate is an oxidized cobalt center, *i.e.* a Co(IV)=O species.

The second investigation probes the ground state 3*d* electronic structure of active and non-active water oxidation catalysts using X-ray absorption spectroscopy to determine an electronic structure-activity relationship. A set of molecular, homogeneous cobalt polyoxometalates serves as model systems for extracting electronic structure parameters, such as metal valence state (*i.e.* 2+ or 3+), metal coordination environment (*i.e.* tetrahedral or octahedral environments), structural distortions and covalency between the metal and oxygen ligands, from cobalt L-edge spectra. No definitive structure-activity relationship could be established because X-ray absorption spectroscopy could not distinguish between the number of metal atoms within the molecular structure or the identity of the heteroatom surrounding the metal(s) and ligands. These properties are what defines the extent of catalytic activity and point to the importance of using more sensitive techniques such as resonant inelastic X-ray scattering. However, ligand field multiplet theory was able to simulate well the experimental Co L-edge spectra for the well-defined model systems and report the ligand field parameter 10Dq to within an accuracy of ±1 eV and the strength of electron-electron interactions to within ±5% of atomic values. These parameters were subsequently applied to characterize a lesser-defined heterogeneous sample, a Co_3O_4 thin film.

Lastly, the final chapter addresses the surface structure dynamics under *in situ* conditions, *i.e.* during the influence of water, on GaN. GaN, a widely studied semiconductor for integration as a photoanode in the water oxidation reaction, possesses a unique surface chemistry and a mobility that is experimentally accessible. Using surface sensitive transient grating spectroscopy, a quantitative value for the hole mobilities of both an undoped and a n-doped GaN film were determined in air and at a semiconductor/electrolyte interface. It was found that interfacial carrier mobility is highly dependent on the surface intermediates. For n-doped GaN, a large density of dark surface states in the form of various adsorbed species exist that can localize holes and, further, allow the holes to hop from metal site to metal site along the surface, possibly assisted by proton-coupled electron transfer with the water molecules. This charge transfer pathway during dark equilibration between the semiconductor electrochemical potential and water oxidation potential more than doubles the interfacial hole diffusivity compared to its value in air. This was confirmed under both acidic and neutral conditions, 0.1 M HBr (pH = 2) and 0.1 M Na_2SO_4 (pH = 7). In contrast, the hole diffusivity of undoped GaN with no significant surface state density is unchanged with introduction of an electrolyte solution. The results suggest that charge transport and surface reactivity, which are generally treated independently, are connected phenomena.

To my loving parents and my patient husband

Contents

List of Figures

List of Tables

List of Abbreviations and Symbols

Λ	grating spacing
χ	electron affinity
ϵ_0	vacuum permittivity constant
ϵ_r	relative permittivity of the material
ϕ_{El}	potential of electrolyte
ϕ_M	reference material work function
ϕ_{SC}	semiconductor work function
e	elementary charge
10Dq	crystal field splitting energy
APCE	absorbed photon-to-current efficiency
C_H	capacitance of Helmholtz layer
C_{SC}	capacitance of space charge region
CB	conduction band
CoPOM	cobalt polyoxometalate
CPD	contact potential difference
CV	cyclic voltammetry
E^0	theoretical Nernstian potential
E_F	Fermi level potential
E_G	band gap energy
E_{VB}	valence band energy
EIS	electrochemical impedance spectroscopy
FLP	Fermi level pinning
HL	width of Helmholtz layer
L_p	hole diffusion length
LFM	ligand field multiplet
LMCT	ligand-to-metal charge transfer
LO	local oscillator
MMCT	metal-to-metal charge transfer
N_D	dopant density

NHE	normal hydrogen electrode
NIR	near-infrared
OCP	open circuit potential
OPA	optical parametric amplifier
Ox	oxidized redox couple
PEC	photoelectrochemical
q_{SS}	surface state charge
Red	reduced redox couple
RIXS	resonant inelastic X-ray scattering
S	surface recombination velocity
SC	space charge
SEM	scanning electron microscopy
SIR	Slater integral reduction
SPV	surface photovoltage
SS	surface states
STH	solar-to-hydrogen
TAS	transient absorption spectroscopy
TEY	total electron yield
TFY	total fluorescence yield
TGS	transient grating spectroscopy
TMOs	transition metal oxides
TR-IR	time-resolved infrared absorption spectroscopy
V_{BB}	band bending potential
V_{FB}	flat band potential
V_H	potential drop in the Helmholtz layer
V_{ph}	open-circuit photovoltage
VB	valence band
VBE	valence band edge
VSOCR	valence spin orbit coupling reduction
W_{SC}	depletion width
WLC	white light continuum
WOCs	water oxidation catalysts
XAS	X-ray absorption spectroscopy
XRD	X-ray diffraction

Acknowledgments

I am grateful to my advisor Professor Tanja Cuk for her mentorship and feedback. It was an honor to be her first graduate student. I also extend thanks to my committee members, Professor Stephen Leone and Professor Junqiao Wu for their support and guidance. I would like to acknowledge financial support from the National Science Foundation and the Chemistry Department at the University of California, Berkeley. Thanks to my undergraduate research advisor at Purdue University, Professor Joseph Francisco, and graduate mentor, Dr. Alex Davis, for introducing me to the exciting world of research and encouraging me to explore it further at the graduate level. Their passion and enthusiasm for scientific discovery were contagious.

Collaboration in science is paramount to success and that could not have been truer for me. As one of the first graduate students in Tanja's group, many people outside the group were instrumental to helping me on my project. Although not an exhaustive list, I want to thank the scientists at the Joint Center for Artificial Photosynthesis who allowed me access to their equipment for thin film deposition and characterization and answered all my questions, especially Dr. Joel Ager, Dr. Ian Sharp, and Dr. Le Chen.

My graduate experience would not have been as enjoyable without my cohorts in the Cuk group. Thank you for your encouragement and conversation, especially Stephanie Choing who has been a friend and peer since the beginning of my journey. I'm glad I got to share the many adventures of science, all the good, the bad, and the ugly together with her. It was an honor to work with Dr. Matthias Waegele whose chemical knowledge and strong work ethic helped guide me in my first years as a researcher.

Finally, I extend my deepest thanks to my parents and husband. My parent's sacrifice to get me an education in America has shown me the importance of taking advantage of all the opportunities I have available, to work hard, and to stay committed no matter the difficulty. Through example, they have shaped me into a resilient and independent female. My husband, Scott Brown, has shown me unbelievable patience and unconditional support. I am forever grateful for his presence in my life and I am so glad I got to experience the Bay Area with him at my side. Although they may not know exactly what I do, they are the reason for my success here.

Chapter 1

Introduction

World energy consumption is projected to nearly double within the next 50 years according to the International Energy Outlook 2010 compiled by the U.S. Energy Information Administration. In 2010, the world market consumed 536 terajoules of energy with 85.9% emerging from petroleum, coal, and natural gas. [1] Although fossil fuel reserves have been speculated to last for several more centuries, consumption of fossil fuels results in anthropogenic climate change due to increasing carbon dioxide (CO_2) emission. In the 5 years I have been in graduate school, between 2010 and 2015, a 0.44° C increase has been observed in the global surface temperature. This is already 22% of the total 2° C limit implemented by the International Energy Agency set for year 2100. At this rate, by the year 2100, the global surface temperature would increase by 8° C unless significant changes to energy consumption are made. [2] A carbon free, hydrogen economy using solar energy is one promising solution for the future where the inputs are water and sunlight and O_2 is the only byproduct. [3] With a power level of 1003 W m^{-2}, the incident solar light has abundant potential to meet world energy demands. There are four methods that utilize solar energy to produce H_2. Thermochemical, photobiological, and electrolysis processes utilize solar energy indirectly in the form of high temperatures, microorganisms and electricity, respectively, to split water. The fourth method, photoelectrochemical (PEC) water splitting, also commonly termed artificial photosynthesis, uses light directly and is considered the best long-term solution.

1.1 Photoelectrochemical Water Splitting

PEC water splitting is promising because it offers high conversion efficiency at normal operating conditions using low-cost semiconductor materials. However, the promise of high conversion efficiency, reliability and cost has yet to be optimized to industrial viability despite forty decades of research. Since Honda and Fujishima discovered semiconductor-based PEC water splitting using a TiO_2 electrode in 1972 [4], the solar-to-hydrogen (STH) conversion efficiency has been steadily increasing. Initially a reported $< 1\%$ STH efficiency for a tandem p-GaP/n-TiO_2 PEC device, was a significant achievement. [5] By 1987, researchers were

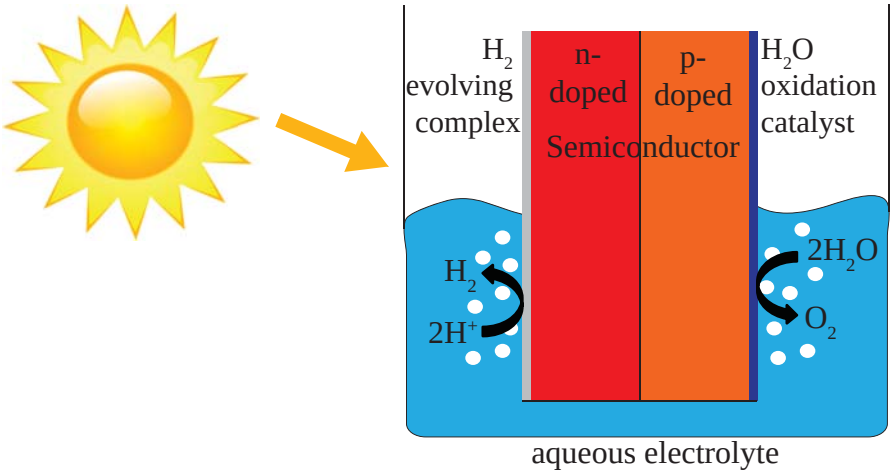

Figure 1.1: A representative picture of a single junction PEC device.

able to achieve almost 8% using p-InN and n-GaAs photoelectrodes. [6] This was followed by a RuO_2-catalyzed AlGaAs/Si junction able to sustain water splitting at 18.3% STH efficiency in 2000. [7] Now, a 24.4% STH efficiency was met by combining a concentrated photovoltaic module using a three junction cell with an electrochemical polymer-electrolyte cell. [8] Although there have been major advances as noted above, the theoretical maximum STH efficiency of $\sim 30\%$ has yet to be achieved for a purely PEC-driven device such as the one illustrated in Fig. 1.1. [7, 9]

Several limitations exist within the PEC architecture. The essential components include: 1) an antenna to absorb photons and produce photoexcited charge carriers, 2) a mechanism to physically move photoexcited charge carriers away from the generation site, 3) two efficient and selective catalysts to drive the two chemical reactions:

$$2H^+ + 2e^- \rightarrow H_2 \quad \mathrm{E}^0 = 0 \text{ V vs NHE} \tag{1.1}$$

$$2H_2O \rightarrow 4e^- + 4H^+ + 2O_2 \quad \mathrm{E}^0 = 1.23 \text{ V vs NHE} \tag{1.2}$$

where NHE is the normal hydrogen electrode. Semiconductors are good candidates because semiconductors have a band gap with a built-in electric field from band bending at an interface. The theoretical Nerstian potentials (E_0) for water reduction and oxidation of 0 V and 1.23 V vs NHE, respectively, are met by semiconductors with conduction band and valence band energies straddling these two potentials. However, those with band gaps optimized for the solar spectrum often suffer from instability linked to photocorrosion. Alternatively, semiconductors with larger band gaps are unable to utilize the full solar spectrum and result in low STH efficiencies. Although band bending helps to promote movement of photo-carriers away from the generation site, many semiconductors still suffer from high recombination rates and short lifetimes. Lastly, the catalytic process to drive the chemical reactions is still not completely understood, particularly the catalyst driving the more complex water oxidation half reaction, *i.e.* Eq. 1.2.

1.1.1 Water Oxidation Catalysis and Overpotential

The water oxidation half reaction is considered the limiting step in meeting maximum STH efficiencies. Several water oxidation catalysts (WOCs) have been explored. As $3d$ transition metal oxides (TMOs) are more abundant and robust, they are commonly tested as WOCs. For example, TMOs such as Co_3O_4, IrO_2, RuO_2, NiO, are commonly used as cocatalysts or electrocatalysts when paired with a solar absorbing material (often called the photoanode if it participates in the water oxidation half reaction) such as TiO_2, Fe_2O_3, WO_3, $BiVO_4$, GaN. [10, 11] These $3d$ TMOs possess large structural variety dependent on the preparation conditions. As a result, their catalytic activity can vary widely owing to their diverse electronic properties. However, the mechanism by which these TMOs are able to oxidize water may show similiarities, connected by the presence of the $3d$ states.

The oxidative level in the aforementioned $3d$ TMOs are generally larger than the 1.23 V versus NHE suggesting there is an overpotential associated with the reaction. [12] The overpotential is the driving force describing the extent of departure of the experimental potential necessary for the reaction to proceed from E^0.

$$Overpotential = \frac{(E_{exp} - E^0)}{e} \tag{1.3}$$

Typical photovoltages necessary to split water are 1.85 V - 2.05 V. [13] Since the Nernstian potential for the H_2O/O_2 redox couple is 1.23 V, this correlates to an overpotential of 0.6-0.8 V. This overpotential is two to three times larger for oxidation than for proton reduction (0.2 - 0.3 V). [14] Some $3d$ TMOs like RuO_2, Co_3O_4, and IrO_2 can lower the overpotential as low as 0.3 V but the kinetic origin of the overpotential is currently unknown. [15] Therefore, in order to achieve scalable PEC-driven H_2 production, the overpotential required for water oxidation still needs to be drastically reduced. This starts with a fundamental understanding of the four-electron transfer reaction mechanism at the catalytic surface. Although the initiation mechanism for water oxidation is generally accepted to occur through formation of surface-trapped holes where adsorbed OH radical, peroxo, oxyl and oxo species are possible intermediates, how the surface-trapped holes activate or direct molecular change on the semiconductor surface is not yet fully understood. [16–19]

1.2 Connecting Surface Charge to Reaction Intermediates

Heterogeneous water oxidation catalysis involves possibly four intermediate steps of adsorption and desorption where bonds are both being formed and broken between the atoms at the catalytic surface and water molecules. These new bonds, *i.e.* adsorbed species, catalyze the reaction by opening up lower energy pathways through new intermediates. In addition to forming those new bonds, an effective catalysis must also break bonds to evolve molecular oxygen via a desorption step. The manipulation of the rates of bond formation

and bond breaking are integral to reduce the overpotential and increase catalytic efficiency associated with WOCs. This starts with an understanding of the surface electronic properties and connecting charge carriers dynamics to the transformation of new molecular bonds. By understanding the intrinsic properties within a material, spectroscopic experiments can help answer the key mechanistic questions surrounding the initial step of water oxidation catalysis. This dissertation embodies two fundamental discoveries within that context.

For photocatalysis, photo-generated carriers can either localize at the transition metal or oxygen site in TMOs. Elucidation of the excited state electronic structure of Co_3O_4 suggests a large density of energetically low-lying $3d$ states that serve as efficient hole traps. As the photo-excited holes have significant localized, Co d-character, it can be inferred that the likely intermediate that forms at the catalytic surface is an oxo Co(IV) species which reinforces previous theories about the reaction mechanism on Co-based WOCs. For example, *in situ* time-resolved infrared experiments directly observed the Co(IV)=O intermediate on a Co_3O_4 nanoparticle and electrokinetic studies of the popular Co-Pi catalyst also found a rapid one electron, one proton equilibrium occurs between Co(III)-OH and Co(IV)=O. [20, 21] The altered metal valency from Co(III) to Co(IV) is suggested to stabilize the radical. This is in contrast to other proposed intermediates where the hole has more oxygen p-character (*i.e.* TM(III)-O$\cdot$). [19, 22, 23] Additionally, these d-d interband transitions are directly related to its efficient electro/photo-catalytic activity because long-lived electron-hole reactants are created. Although the absorption coefficient for these dipole forbidden transitions is smaller than the allowed charge transfer transitions, their intensities are still on par with the indirect transition intensity of silicon and can be utilized for photovoltaic and photocatalytic systems.

In addition to the recombination and trapping kinetics, how the carriers get to the reaction center, whether it be the metal or oxygen site, and what role does that transport play in the efficiency of the reaction must be considered. For example, in some PEC devices, the geometry promotes diffusion-limited current evolution. [7] In other words, the intrinsic carrier mobility of the semiconductor is another limiting factor. This phenomenon is explored in GaN, a promising photoanode for self-driven photoelectrolysis. [24, 25] An interdependence between interfacial mobility and surface reactivity is established through comparison of the diffusivity at multiple unique interfaces. For n-doped GaN, a large surface charge modifies the surface composition of water adsorbed species, forming several types of intermediates such as Ga-O($\cdot$)H and Ga-O($\cdot$) during dark equilibration with the electrolyte. These dark intermediates can also be assigned as efficient hole traps where hole transport occurs via hopping through the narrow band of localized states or, in molecular terms, between the neighboring surface bound intermediate sites. During the trapping/hopping process, hydrogen ions or protons at the interface are likely released and recaptured in a process commonly referred to as proton-coupled electron transfer to accommodate the surface charge. [26] This charge exchange provides a new current pathway for the interfacial charge carriers and results in an increased hole mobility.

1.3 Overview

To engineer a viable artificial photosynthetic system, rather than testing a class of materials with an almost unlimited number of candidates, a more fruitful endeavor would be to determine how the surface electronic structure affects the photo-hole reactant in the $3d$ transition metal, *e.g.* its lifetime, movement, and destination, or what features of the electronic structure cause effective catalysis and use this knowledge to predict the best semiconductor composition. To that end, the focus is a probe of the surface electronic structure properties that define the catalytic activity of several promising transition metal-based systems involved in oxygen evolution using spectroscopy to capture the complexity. First the solid state theory and characterization techniques for semiconductors are introduced followed by a brief summary on the properties at the semiconductor/electrolyte interface including surface state and Fermi level pinning effects and photoelectrochemical techniques to probe this interface. Next, I will discuss the work performed on a heterogeneous water oxidation catalyst, Co_3O_4 and our understanding of the electronic structure dynamics influencing carrier lifetimes using transient absorption spectroscopy (TAS) that selectively probes key transitions involving the $3d$ electrons. The energetics of these $3d$ states are further enforced with a secondary technique called spectroelectrochemistry that manipulates the oxidative level via an applied potential. A corollary study involving a Co_3O_4/ZnO heterojunction is briefly discussed in Appendix A in an effort to manipulate the photo-hole dynamics via a large built-in electric field. The fourth chapter provides a better understanding of how the ground state electronic structure affects catalysis and defines key covalent and atomic parameters of the transition metal through the use of X-ray absorption spectroscopy (XAS) on Co_3O_4 thin film and a set of inorganic, molecular water oxidation catalysts, cobalt polyoxometalates (CoPOMs). The potential of resonant inelastic X-ray scattering is noted in Appendix B based on one set of experimental data probing the valence band electronic structure of the oxygen atom in the CoPOM structure. Lastly, in the final chapter, I address the issue of photo-hole transport mechanisms using transient grating spectroscopy (TGS) on GaN films to reveal the significance of surface state effects from adsorbed species to the material properties. A detailed theory of transient grating spectroscopy is given along with three photoelectrochemical experiments that characterizes the GaN/electrolyte interface.

Chapter 2

Transition Metal-Based Semiconductors

Water oxidation occurs at the semiconductor/water interface through the transfer of charge between the water molecules and semiconductor surface species. Therefore, the semiconductor and its (photo-)dynamic surface is essential to explore. First, a general theory of solid state as it pertains to semiconductors in air is introduced followed by a description of the interfacial properties of semiconductors in electrolyte. An integral property controlling the behavior of semiconductors is a dense surface state population that can pin the electrochemical potential of the semiconductor. Finally, a brief description of a few (photo-) electrochemical and electrical techniques are given that serve as analytical tools to characterize the semiconductor.

2.1 Solid State Theory

Semiconductors are a framework of a periodic array of atoms. With a large number of atoms close together in a crystal lattice structure, the discrete energy levels overlap to form a nearly continuous band for electrons to freely move around. [27] Unlike in metals where empty and occupied orbitals overlap to form one continuous band, semiconductors or insulators have two distinct bands consisting of the maximally occupied valence band (VB) and the lowest empty conduction band (CB), which are separated by a small or significantly large band gap, respectively. The energetic positions of the VB and CB and magnitude of the band gap are dependent on the composition of the crystal structure. For example, mixed alloys such as a combination of ZnO and GaN or external dopants such as indium can reduce the band gap of GaN from ultraviolet to near infrared energies. [28–30] Within the band gap lies the Fermi level potential (E_F) describing the energy at which there is a 50% probability of electron occupation at thermodynamic equilibrium. This parameter is easily tuned via doping which is the incorporation of impurities into the crystal structure. [31, 32] Additionally, E_F, which describes the electrochemical potential, is externally tuned via an

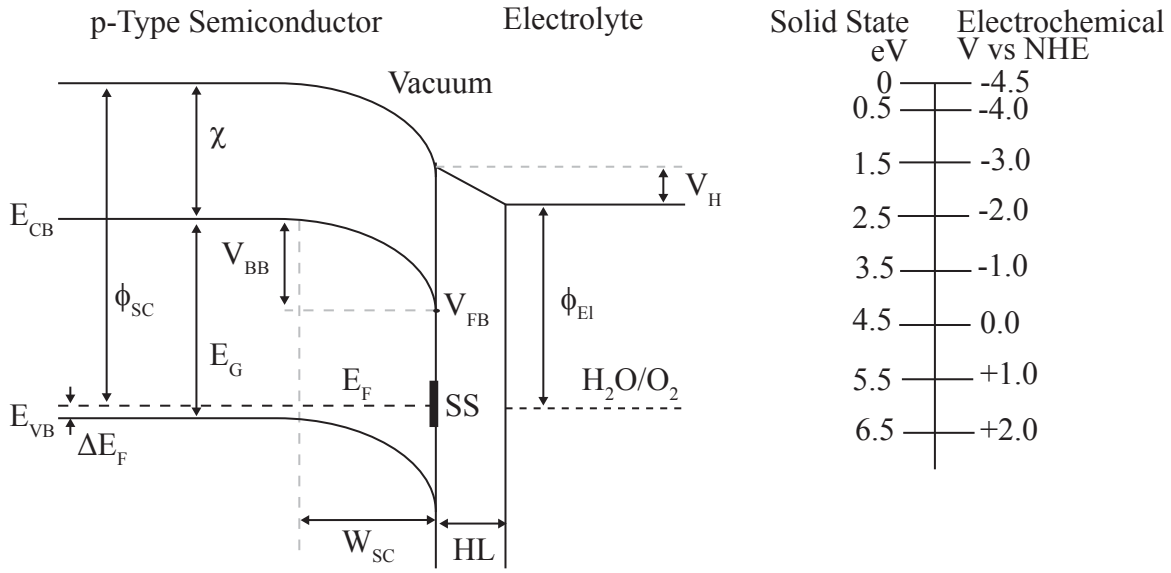

Figure 2.1: Band diagram at a p-type semiconductor/electrolyte interface equilibrated with the Nernst potential for water oxidation and comparison of solid state (eV) and electrochemical (V vs NHE) scale.

applied potential or through illumination with above band gap light. When donor (acceptor) impurities are introduced, an n-type (p-type) semiconductor forms, which shifts the E_F closer to the CB (VB) because there are extra electron (hole) energy levels. These constructs categorize the carrier mobility within the crystal lattice and affect the behavior of a semiconductor. A band diagram for a p-type semiconductor is given in Fig. 2.1 for a qualitative picture of these constructs. The vacuum level is the energy of a free electron with zero kinetic energy. The electron affinity (χ), is the energy required to remove an electron from the CB. The semiconductor work function (ϕ_{SC}) is the energy required to remove an electron from E_F. V_{BB} and V_{FB} are the band bending and flat band potential, respectively, while E_G and E_{VB} are the band gap and valence band energies, respectively. For a p-type semiconductor, ΔE_F is defined as the difference between E_F and E_{VB}. Surface states (SS) within the band gap also play a crucial role in semiconductor (photo)physics and are discussed further below. The properties of the electrolyte in contact with the semiconductor, considered in the next section, are the potential drop in the Helmholtz layer (V_H), potential of electrolyte (ϕ_{El}) and width of Helmholtz layer (HL).

For doped semiconductors, a band bending phenomenon occurs at equilibrium at the surface. The surface and bulk chemical compositions are inherently different due to the lattice termination and presence of adsorbed species. Therefore, in equilibrium where the chemical potential of the system must be equal, a depletion layer forms due to dark charge transfer of free carriers to screen the surface electric field. This shifts the band energies either upward for n-type or downward for p-type and results in a space charge (SC) region

that has an associated depletion width (W_{SC}). The extent of band bending is determined by the following equation,

$$V_{BB} = -\frac{W_{SC}^2 N_D e}{2\epsilon_0 \epsilon_r} \tag{2.1}$$

where N_D is the dopant density. e, ϵ_0 and ϵ_r are the elementary charge, vacuum permittivity constant and relative permittivity of the material, respectively. V_{BB} is measurable via the surface photovoltage (SPV) technique, which, then, can be used to calculate W_{SC}.

$$W_{SC} = \sqrt{\frac{2\epsilon_0 \epsilon_r V_{BB}}{e N_D}} \tag{2.2}$$

For example, p-type Co_3O_4 has a minimum V_{BB} of 100 meV which correlates to a W_{SC} of 1.2 nm where $\epsilon_0 = 8.854 \times 10^{-12} \frac{F}{m}$, $\epsilon_r = 12.9$, and $N_D = 1{\times}10^{20}$ cm^{-3}.

2.1.1 Solid State Characterization Techniques

Contact potential difference (CPD) is a contactless and nondestructive, steady state technique to measure ϕ_{SC} with respect to the work function of a known reference material (ϕ_M). The sample is placed in close contact with a vibrating metallic reference electrode, often called the Kevin probe, typically gold, in a capacitor-like configuration with distances kept between 0.1-1 mm. Under no external bias, the sample and the probe have equilibrated E_F, meaning that charge was exchanged between the two materials resulting in a potential drop across the gap between the sample and probe, *i.e.* a drop in the sample vacuum level (Fig. 2.2). The probe is vibrated to generate an alternating current with a certain frequency, generally 500-600 Hz. A compensating voltage source is tuned until that current flow is zero. The voltage at which current stops is the V_{CPD}, defined as

$$qV_{\text{CPD}} = \phi_M - \phi_{SC} \tag{2.3}$$

For Co_3O_4, V_{CPD} is -0.180 eV relative to gold (4.7 eV), *i.e.* $\phi_{SC} = 4.52$ eV. At the surface of the material, V_{BB} exists and can be measured using SPV, which flattens the band upon light saturation. When illuminating with monochromatic light of energy greater than the band gap, the space and surface charge will change as a result of photoexcited electrons and holes. Since the sample's work function is related linearly to the surface potential, photo-induced changes in the SPV records V_{BB} based on

$$V_{BB} = V_{\text{SPV}} \text{ (illuminated)} - V_{\text{CPD}} \text{ (dark)} \tag{2.4}$$

Positive changes correspond to excitation of electrons from the VB into a SS while negative changes correspond to excitation of electrons from a SS into the CB. Therefore, a positive SPV implies p-type behavior (*i.e.* holes are the majority carriers) whereas a negative SPV suggests n-type behavior (*i.e.* electrons are the majority carriers). CPD measurements with a Kelvin probe were performed using a Tektronix TDS 1001B oscilloscope with a Kelvin

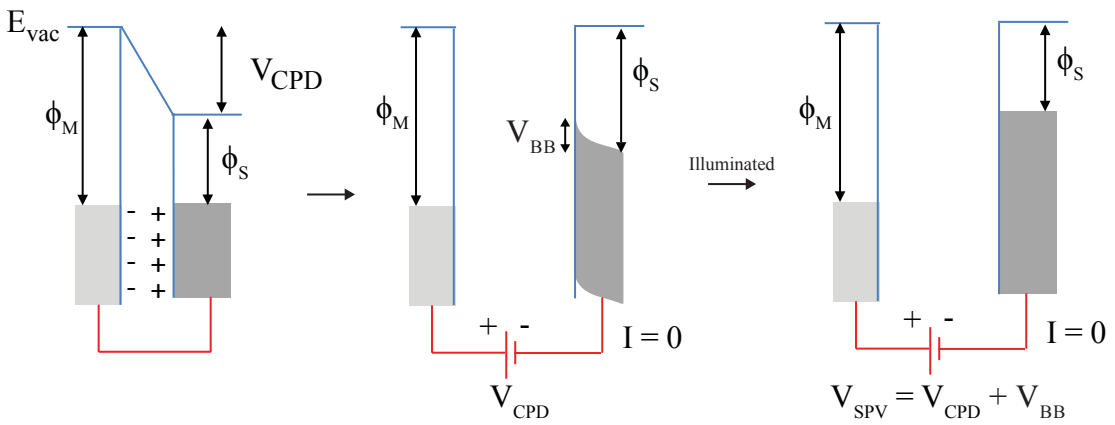

Figure 2.2: Contact potential difference and surface photovoltage measurements.

Control 07 (Besocke Delta Phi GmbH, Jülich, Germany) and Agilent E3620A (Agilent Technologies, Santa Clara, CA) system at the Joint Center for Artificial Photosynthesis.

Another useful characterization tool for solid state systems is X-ray diffraction (XRD), which can answer structural questions about the semiconductor, such as is the material amorphous or crystalline and what is the grain size and crystal orientation. Since the wavelength of an X-ray (10^{-10} m) is on par with atomic distances, X-rays probe interatomic distances and bond angles. X-rays are produced by bombarding a metal target such as Cu with a beam of electrons emitted from a hot tungsten filament. The incident electrons ionize electrons from the 1s orbital or K-shell of the metal. The relaxation process to fill the electron vacancy from the 2p orbital or L-shell results in an emitted X-ray to yield the Kα line. For example, the phase structure of Co_3O_4 was characterized with Cu Kα radiation ($\lambda = 1.5418$ $\mathring{A}$). When X-rays hit the semiconductor, it will get reflected at atomic sites. According to the Bragg equation, constructive interference occurs when the path difference between two diffracted waves from two planes of atoms in a solid is described by

$$n\lambda = 2dsin\theta \tag{2.5}$$

where n is a positive integer and d is distance between the two planes, *i.e.* lattice spacing, as depicted in Fig. 2.3. An XRD pattern forms by measuring the intensity of the diffracted X-rays as a function of 2θ. Only when the Bragg equation is met will a diffraction peak form. The peak width varies inversely with crystallize size. The crystallite size is the average size of a coherent scattering domain or a perfect arrangement of unit cells, called a perfect crystal. As crystallite size gets smaller, the peak gets broader suggesting more grain boundaries. Additionally, the greater number of peaks suggest a variety of grain orientations and, hence, illustrates polycrystallinity. If no peaks arise at any θ because all the reflected waves interfere destructively from the lack of periodicity, the material is amorphous. Quantitative extraction

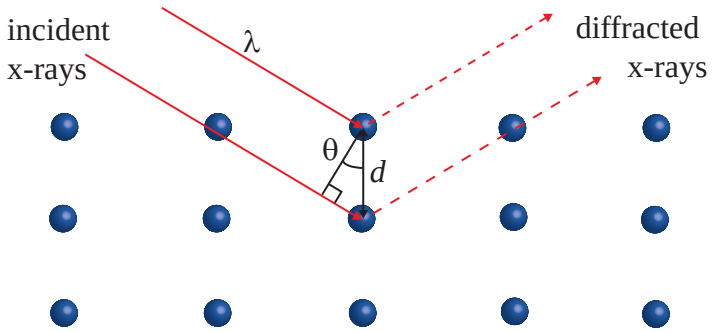

Figure 2.3: Bragg geometry for X-ray diffraction

of the crystallite size can be determined using Scherrer's equation.

$$D_p \text{ (crystal size)} = \frac{K\lambda}{FWHM \cdot \cos\theta} \tag{2.6}$$

where K is the Scherrer constant assumed to be 0.94, λ is the wavelength of the radiation, FWHM is the full width half maximum, and θ is half the diffraction angle. [33] Generally, the goal for semiconductor photocatalysts is to increase the crystal size in order to reduce recombination because grain boundaries are prolific recombination centers. Note that crystallite size and grain size are not necessarily the same, since a grain may be composed of multiple crystallites.

2.2 Semiconductor/Electrolyte Interface

When a semiconductor is immersed in an electrolyte solution, a new potential gradient forms across the two phases, *i.e.* at the electrode/electrolyte interface, due to charge transfer across the interface during dark equilibration of the Fermi level of the semiconductor with the Nernst potential of the redox couple in electrolyte. [32, 34] Charge transfer can occur by electrons in the conduction band to the oxidized redox couple (Ox) to form the reduced redox couple (Red) (eq. 2.7) or holes in the valence band to the reduced redox couple to form the oxidized species (eq. 2.8). The direction of electrons depends on the position of the semiconductor E_F with respect to the Nernstian potential of the redox couple.

$$\text{Ox} + e^-_{(CB)} \rightarrow \text{Red} \tag{2.7}$$

$$\text{Red} + h^+_{(VB)} \rightarrow \text{Ox} \tag{2.8}$$

The redistribution of charges at the semiconductor/electrolyte interface is described by an electric double layer, commonly referred to as the Helmholtz layer (HL), and modeled as a parallel-plate capacitor. Analogous to a solid-state capacitor, this is two layers of opposite charges separated at a fixed distance. One layer is the adsorption of ions on the electrode

and the other layer consists of oppositely charge ions in solution. There is a linear potential drop across these two layers and the capacitance (C_H) is

$$C_H = \frac{\epsilon_0 \epsilon_r}{4\pi d} \tag{2.9}$$

where ϵ_r is the dielectric constant of the medium and d is the distance between the layers. C_H is generally 10-100 μF cm^{-2} for aqueous solutions, which is much larger than the capacity of the SC region. [35] An additional capacitor-like model (C_{SC}) is used to describe the interface in terms of the semiconductor where the electric field felt by the charge carriers is a function of the distance from the surface. An equivalent circuit for the semiconductor/electrolyte system consists of two main capacitors.

$$\frac{1}{C_{eq}} = \frac{1}{C_{SC}} + \frac{1}{C_H} \tag{2.10}$$

Such a model describes the distribution of the potential (applied or photo-activated) at the semiconductor/electrolyte interface. As $C = \frac{q}{V}$, it is consistent with charge neutrality, *i.e.* $q_H = q_{SC}$, where the potential drop is dependent on the magnitude of the capacitance of the HL and SC region. Two limiting cases occur: 1) $C_H \gg C_{SC}$ and 2) $C_H \ll C_{SC}$. [36] For the first limiting case, most of the potential is dropped across the semiconductor and V_H is constant. The band edges are pinned while E_F shifts. In the second extreme, the potential drops across the electrolyte while V_{SC} is constant. This results in an unpinned band edge and a pinned E_F. The magnitude of C_{SC} is generally dependent on the doping and surface state density. [34, 37]

2.2.1 Surface States and Fermi Level Pinning

Formation of a surface breaks the translational symmetry of the crystal lattice causing dangling bonds and lattice defects. Further in contact with an electrolyte, that surface contains adsorbed species and possibly dark reaction intermediates. As a result localized SS with distinct energy levels within the band gap are generated. At a large enough density, these SS start mediating the dark equilibration process, providing the only pathway for charge transfer. In this case, the charge transfer occurs between the charges in the bulk and SS (Eq. 2.11) and between the SS and redox system (Eq. 2.12) in a two step process.

$$\begin{aligned} e^-_{(CB)} + SS_{(CB)} &\leftrightarrow SS^-_{(CB)} \\ h^+_{(VB)} + SS_{(VB)} &\leftrightarrow SS^+_{(VB)} \end{aligned} \tag{2.11}$$

$$\begin{aligned} \mathrm{Ox} + SS^-_{(CB)} &\leftrightarrow \mathrm{Red} \\ \mathrm{Red} + SS^+_{(VB)} &\leftrightarrow \mathrm{Ox} \end{aligned} \tag{2.12}$$

This surface charge q_{SS} = -q_{SC}. Generally, SS are highly efficient recombination centers that reduce minority carrier lifetimes and reduce efficiency of solar fuel devices. Therefore,

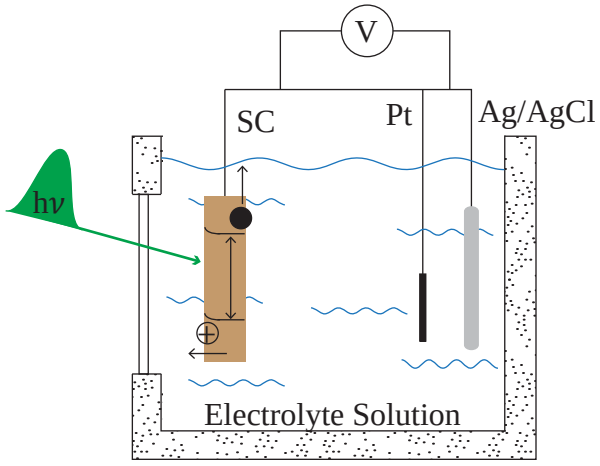

Figure 2.4: A representative picture of a three-electrode PEC cell.

passivation techniques are often used in order to saturate the surface sites. [38, 39] However, SS can also act as potential catalytic sites enhancing the kinetics by offering a competitive alternative pathway for charge carriers. [40]

As previously mentioned, the potential drop that occurs either with an externally applied potential or via illumination occurs mainly in the SC region within the semiconductor because of the greater charge distribution in the electrolyte solution (10^{20} cm^{-3}) than in an undoped or moderately doped semiconductor (10^{15} - 10^{19} cm^{-3}). [35] However, this is not the case in the presence of a large concentration of mid-gap surface states or a highly doped semiconductor. When the charge density is greater in the SS than the SC region, a process known as Fermi level pinning (FLP) occurs. The Fermi level becomes independent of the bulk dopant density and, hence, V_{BB} is fixed at the SS energy level while the band edges vary with applied potential. A new equivalent circuit exists for the semiconductor/electrolyte system consisting of three main capacitors:

$$\frac{1}{C_{eq}} = \frac{1}{C_{SC}} + \frac{1}{C_H} + \frac{1}{C_{SS}} \tag{2.13}$$

For an ideal semiconductor/electrolyte interface, the open-circuit photovoltage $V_{ph} = V_{redox}$ - V_{FB} where V_{redox} is the potential of the solution redox couple and V_{FB} is the flat band potential in the absence of that redox couple. When FLP occurs, V_{FB} behavior becomes dependent on V_{redox}. [41] The extent of FLP can vary where partial and complete FLP exists which can be determined based on the slope of V_{ph} vs V_{redox}.

2.2.2 Semiconductor Photoelectrochemistry

For electrochemical experiments, a three electrode set up is utilized (Fig. 2.4) and performed in a custom made Teflon cell. The working electrode is the semiconductor where the

reaction(s) of interest occurs. In order to measure the potential drop across the interface between the electrode surface and electrolyte solution, a secondary interfacial potential must be introduced via the counter electrode, typically a Pt wire. The third electrode is the reference electrode, which controls the potential between itself and the working electrode while current passes through the working and counter electrodes. The reference electrode used is a silver/silver chloride (Ag/AgCl (Sat.'d NaCl)) electrode (MF-2021, BASi, West Lafayette, IN). The standard redox potential for Ag/AgCl is 0.206 V vs NHE at 25° C. Measurements were typically performed on a CHI1140B Potentiostat (CH Instruments, Inc., Austin, TX). The electrolyte solution varies and is mentioned specifically for each case. For accurate measurements, ohmic contacts must be made to each electrode. The best ohmic contacts were made by contacting the working electrode with silver paste and a copper wire. For materials with lower resistivities, an InGa eutectic was additionally added. An insulating lacquer covers the contact to avoid current leakage so only a known area of the working surface is exposed to the solution.

A number of (photo-)electrochemical techniques are available to characterize the material's properties and how those properties change upon illumination. Cyclic voltammetry (CV) measures the current that develops under a varying voltage that is ramped in both the forward and reverse direction. The voltammograms provide information about the identify and stability of the semiconductor, the redox reactions and corresponding intermediates occurring at the surface and how far above the Nernst potential the reaction proceeds. For example, in a WOC catalyst immersed in an aqueous solution, a large anodic (negative) current peak may indicate O_2 evolution and at what potential the peak occurs can determine the overpotential. Additionally, when illuminated a potential shift in current onset can occur to define V_{FB}. Several parameters can be tuned to investigate the current-voltage response, *e.g.* pH, solution concentration, and redox couple. Electrochemical impedance spectroscopy (EIS) probes the potential distribution at the semiconductor/electrolyte interface based on the response to an alternating current at a defined frequency. It determines the capacity of C_{SC}. Using a Mott-Schottky relationship [42], described by

$$\frac{1}{C_{SC}^2} = \frac{2}{eA_s^2\epsilon_r\epsilon_0 N_D}(|V - V_{fb}| - \frac{kT}{e}) \tag{2.14}$$

where A_s is the electrode area and V is the applied potential. Both N_D and V_{FB} can be determined from the slope and intercept, respectively. Several assumptions are made for the Mott-Schottky relationship, which need to be kept in mind, including $C_H \gg C_{SC}$. [43] Often the response of C_{SC} can be separated from other interfacial structures and processes by selecting the appropriate frequency range. For example, the effects of SS are made negligible at high enough frequencies. [41] On the other hand, at low frequencies, EIS can be employed to characterize SS such as its energetic location and density. [44]

Chapter 3

Photoexcited Carrier Dynamics of Spinel Ordered Cobalt Oxide

Portions of the content and figures of this chapter are reprinted or adapted with permission from M.M. Waegele, H.Q. Doan, and T. Cuk, J. Phys. Chem. C 118, 3426 (2014).

3.1 Introduction

The large structural variety in $3d$ TMOs, owing to their unique electronic structures, make them promising candidates for integration into solar fuel devices, particularly as WOCs. [10, 45] Fast carrier trapping and recombination processes that limit the catalytic efficiencies within these materials are often mitigated by tuning the surface and bulk electronic properties. [46–49] The success of this strategy relies on understanding the underlying photoexcited carrier dynamics in these $3d$ TMOs, which are often convoluted with several types of possible optical transitions. Previous transient absorption measurements have already identified dopants, defects, and surface states as responsible for reducing the population of available photo-active holes. [46, 49–52] However, ligand-to-metal charge transfer (LMCT) between the oxygen and metal site, metal-to-metal charge transfer (MMCT) between neighboring metal sites, and intravalence d to d transitions within a metal site will also inherently control where, when, and how the photoexcited carriers trap or recombine. For example, there are distinct time scales observed within the transient dynamics of copper oxide superconductors or manganite dependent on excitation of the charge transfer or intravalence electronic transition, respectively. [53–56] In other cases, like in Fe_2O_3 systems, a probe dependence may or may not be observed in the charge dynamics attributed to the presence or lack of mid-gap states. [46, 49] To that end, the effects of the inter- and intravalence optical transitions are explored using a robust and abundant WOC, a spinel transition metal oxide (Co_3O_4) and the transient electronic structure detailed.

As the oxidative level of a semiconductor can be tuned by either light or an applied potential, a probe of the transient electronic structure of Co_3O_4 was performed using both

transient absorption spectroscopy or spectroelectrochemistry. The first section reviews the transient absorption technique that probes the changes in the absorptive property of Co_3O_4 along with the description of the laser system. In the next section, the sample preparation and characterization of the optical and electrochemical properties of the Co_3O_4 thin films are commented on. Lastly, the results of the experimental work are discussed in terms of the transient spectral and kinetic response of Co_3O_4 to selective excitation, morphology, fluence and selective detection. Further a connection of the transient optical study is made to the spectroelectrochemistry method in order to define the energetics of important midgap d states. This d manifold is linked to the independence of Co_3O_4 to the different tuning factors and existence of the long-lived nanosecond charge dynamics. The relevance of occupied d states is summarized in the context of an effective trap center prevalent to several $3d$ TMOs that could potentially be utilized in water splitting devices.

3.2 Transient absorption spectroscopy

The advent of the Ti:Al_2O_3 (Ti:sapphire) laser in the 1980's led to a boom in the ultrafast optical community, allowing for femtosecond resolution and studies of charge relaxation dynamics of electronic states in condensed matter systems. [57] Ultrafast TAS has emerged in order to measure the changes in the optical properties, namely the complex index of refraction $\tilde{\eta}$, as a function of time after excitation (kinetics) or as a function of excitation wavelength (spectrum) in solid state systems. Within the ultraviolet (UV), visible (vis), and near-infrared (NIR) region of radiation, TAS probes the electronic states and the transfer of electrons between them within a solid. Particularly, the transient absorption kinetics provide information regarding the decay rate of ultrashort-lived photoexcited carriers, probing the efficiency of trap states, electronic states, and surface states involved in scattering, recombination and charge transfer processes. The transient absorption spectrum provides information regarding the energies and identities of the available electronic states. Within this context, this technique is a powerful tool for understanding the photo-induced processes in heterogenous catalysis. [46, 58]

TAS, a two pulse pump probe technique, involves a single pump pulse that excites the sample to create electron-hole pairs. These charge carriers are monitored by a second incoming probe pulse that is time delayed with respect to the pump pulse. The percent intensity change of the transmitted probe beam is the observable and determined as

$$\frac{\Delta T}{T} = \frac{T_{pump,\ on} - T_{pump,\ off}}{T_{pump,\ off}} \tag{3.1}$$

This intensity is modulated by the excitation process in the sample, *e.g.* an increased transmittance due to a reduced population in the ground state ($+\Delta T$) is referred to as a bleach or a decreased transmittance from transitions between excited state to higher excited state is referred to as an induced absorption ($-\Delta T$). Without interference effects, the absorbance

I_A is related to the incident I_0, reflected I_R, and transmitted I_T by

$$I_A = I_0 - I_R - I_T \tag{3.2}$$

The change in absorbance, within the weak excitation limit, in terms of the Beer-Lambert Law is

$$\Delta A = log(1 - \frac{\Delta F_R}{1 - F_{R,off}}) - log(1 + \Delta F_T) \sim log(1 - \Delta F_R) - log(1 + \Delta F_T) \tag{3.3}$$

where $F_{R,off}$ is the static reflectance spectrum and assumed to be $\ll 1$. ΔF_R and ΔF_T is the observed fractional change in the reflected and transmitted intensity, respectively. For thin enough films, ΔF_R is small compared to ΔF_T and $\Delta A \sim -log(1 + \Delta F_T)$. The transient transmittance spectrum, then, provides information about the absorptive part or imaginary component $\tilde{\eta}$. However, in thin enough films, both the transmitted and reflected TA response comes from the absorptive property (k), as can be derived by solving for the thin film equations in the limit that $d \ll \delta$ where d is the thickness of the film and δ is the penetration depth of the light, described by $\frac{4\pi k}{\lambda}$. [59, 60] Further, for substrates that have a greater dielectric constant than air, the reflectance in air will be equal in magnitude but opposite in sign to the transmittance. [59, 60]

3.2.1 Laser system

The optical system is layed out in Fig. 3.1 and consists of a regeneratively amplified Ti:Sapphire laser system (Coherent Legend, Coherent, Inc., Santa Clara, CA) with a seed input from a mode-locked Ti:Sapph oscillator pumped with a Nd:YVO_4 diode. An 800 nm AlGaAs diode pumps an acousto-optical Q-switched Nd:YLF crystal and then passes through a nonlinear LBO to get 527 nm from intra-cavity frequency doubling to act as the pump source (Evolution, Coherent, Inc., Santa Clara, CA). The output pulse has a center wavelength of 800 nm and 150 fs pulse width at a 1 kHz repetition rate with <0.5% rms energy stability. Typical output power is 4.5 W. Part of the amplifier output was directed into an optical parametric amplifier (OPA) (OPerA-SOLO; Light Conversion, Vilnius, Lithuania) for generation of laser pulses ranging from 240 nm all the way to 20 μm. For experiments probing the spectral changes in the 450 - 1000 nm wavelength range, the output of the OPA was used as the pump and a broad white light continuum (WLC) was used as the probe.

The output of the OPA passes through a set of linear neutral density filters for continuous adjustment of pump power. The WLC, with intensity starting from 450 nm to 1000 nm as shown in Fig. 3.2, was produced by focusing 800 nm light into a 2 mm sapphire plate. A portion of the spectrum was removed using a 808 nm StopLine single-notch filter (NF03-808E-25, Semrock, Rochester, New York) with a 41 nm bandwidth in order to block the intense fundamental beam. After focusing the WLC onto the sample with a 150 mm lens, the transmitted or reflected probe beam was collimated, dispersed into an Acton SP-2300 monochromator (Princeton Instruments, Princeton, NJ) and detected on a silicon photodiode

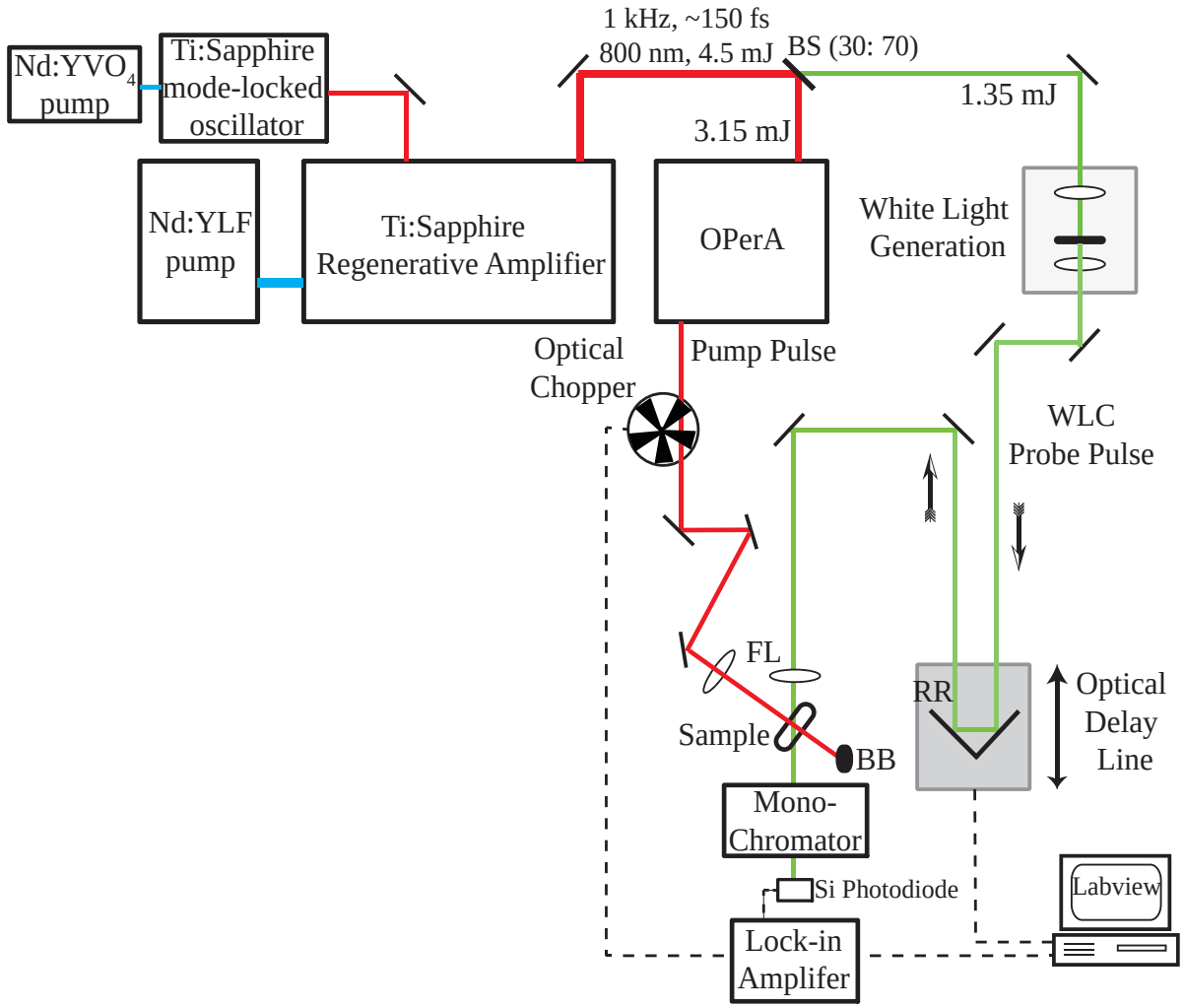

Figure 3.1: Laser System and PP Optical Layout. BS is beamsplitter, BB is beam block, RR is retroreflector, and FL is focusing lens

(DET10A, Thorlabs, Inc., Newton, NJ). For experiments probing the spectral changes in the 1200-1700 nm wavelength range, the OPA output was used as the probe and the fundamental 800 nm was the pump. Detection of infrared light was achieved by employing a liquid nitrogen-cooled InSb detector (INSB-2.0; Infrared Associates, Inc., Stuart, FL).

In all experiments, the pump beam was modulated by a mechanical chopper (SR540; Stanford Research Systems, Inc., Sunnyvale, CA). Detector output was digitized on a lock-in amplifier (SR810; Stanford Research Systems, Inc.; Sunnyvale, CA) and interfaced on a personal computer which provided automatized control over an optical pump probe delay stage (MTM250CC1, Newport, Inc., Irvine, CA) and monochromator. The pump beam hit the sample normal to the surface plane. The spot size of the pump was controlled by

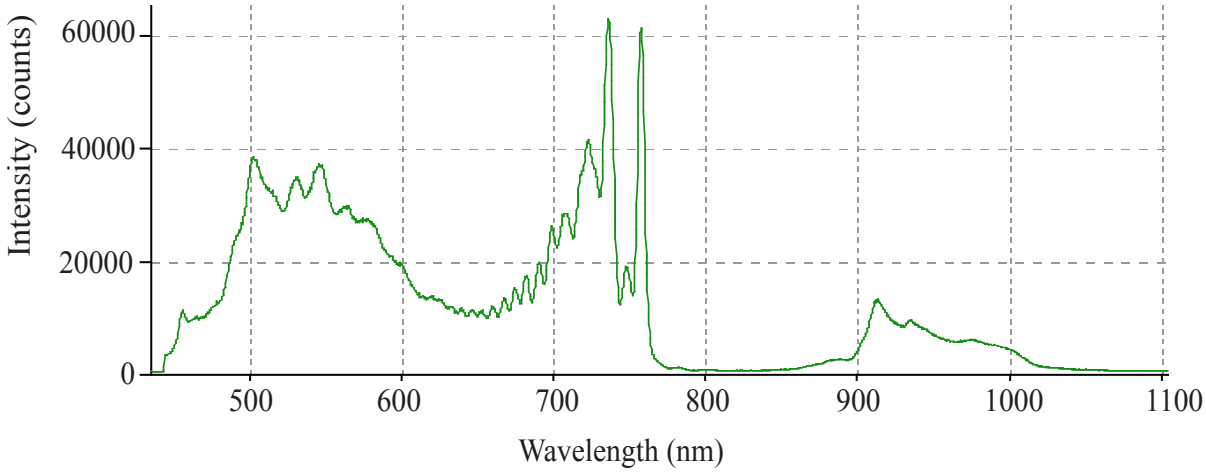

Figure 3.2: White light supercontinuum spectrum

adjusting the position of a 500 mm focusing lens relative to the sample and, depending on the wavelength, varied between 500 μm - 800 μm based on the full width half max of a gaussian. All spot sizes were determined by the knife-edge method with a standard deviation between measurements of $\pm$5%. The probe beam intersected the sample at an angle of 45° to the surface producing an elliptical spot size of approximately 120 μm $\times$ 85 μm. Time zero was defined as the midpoint of the sharp rising edge of the transient absorption kinetics. Although, with white light pulses, different wavelengths arrive at slightly different times, no chirp correction was performed for the transient spectrums because time precision was not necessary and the chirp was considered negliglible. Incident pump fluences were between 0.5 - 2 mJ cm^{-2}, corresponding to carrier densities on the order of 10^{20}-10^{21} cm^{-3}.

3.3 Properties of Spinel Cobalt Oxide

Co_3O_4 is a representative $3d$ TMO with four pronounced absorptions spanning all the relevant types of optical excitations, making it an ideal system to study. [61–63] As an effective water oxidation co-catalyst, Co_3O_4 possesses several key properties such as stability at multiple valence states, ability to accumulate oxidizing equivalents at metal cation sites, resistivity to photo-corrosion via formation of stable compounds and modest overpotentials. Several other TMOs, such as RuO_2 and IrO_2, can catalyze the water oxidation reaction with close to 100% quantum yield but these TMOs are not earth abundant and, therefore not as cost-effective as Co_3O_4. [10, 45] However, the catalytic efficiency of Co_3O_4 is not limited by photo-activation but, rather, the reaction rate is an intrinsic property of Co_3O_4. [45] Addressing catalysis in Co_3O_4, then, starts with a fundamental understanding of the photoexcited charge carrier dynamics as it relates to the electronic structure of the material.

3.3.1 Sample Preparation via Sputtering

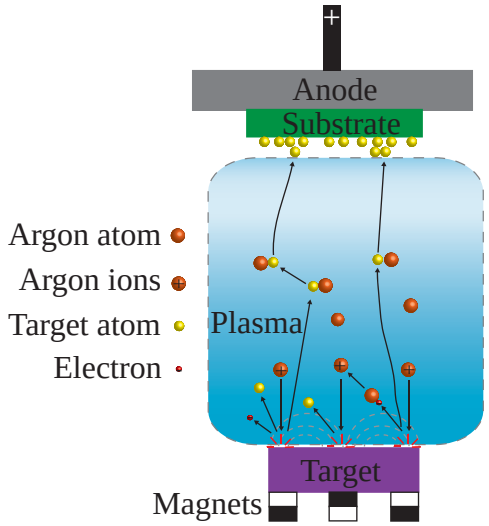

Figure 3.3: Diagram of RF magnetron sputtering

Co_3O_4 thin films were deposited on quartz, $MgAl_2O_4$ (110), indium tin oxide (ITO)-covered glass, ZnSe, or Si substrates using a physical vapor deposition method (PVD) in the form of radio frequency (RF) reactive magnetron sputter deposition, highlighted in Fig. 3.3. The method consists of electrically neutral argon (Ar) gas injected into a vacuum chamber. The Ar ionizes by a strong potential difference. The Ar^+ ion particle accelerates towards and strikes the surface of the target (cathode). After impact, a plume of Co neutral atoms and electrons are released. The Co neutral atoms propel towards a substrate (anode) where it is deposited to form a thin film.

Ar^+ returns to vacuum as a neutral Ar atom after hitting the target surface but is replenished by electron impact with the secondary electrons in a positive feedback system. A charge build-up at the surface can occur if there is no electron impact until Ar^+ particles are no longer attracted to the target. Therefore, it is necessary to apply an RF or AC power to the target instead of direct current (DC) so that the ion charge is expelled during the positive or neutral phase. A magnetic field below the target is introduced in a magnetron sputtering system. The strong magnetic field confines the secondary electrons emitted near the surface so the electrons do not reach the substrate and damage the thin film being formed. Secondly, the electrons spiral along the magnetic flux lines, which enhances the distance traveled and increases the probability of the electron ionizing an Ar atom. To form the oxide film, the Co neutral atoms must undergo a chemical reaction with O_2 before depositing onto the substrate. Therefore, a second gas source (O_2) is introduced into the vacuum chamber for reactive magnetron sputtering.

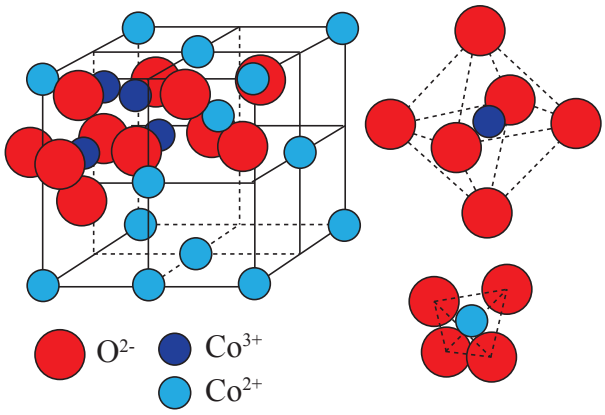

Figure 3.4: Spinel cobalt oxide unit cell

A 2" ceramic Co target of purity 99.95% is used and introduced to 5 mTorr of Ar/O_2 pressure. The charged plasma particles react with 10% O_2 partial pressure. Film stoichiometry to get the spinel ratio was achieved by adjusting the target temperature to 500°C and a working power of 200 W. Film thicknesses were varied based on deposition time with an average rate of 0.56 $\AA$/s. The sputtering system (AJA International, Inc., Scituate, MA) employed was at the Joint Center for Artificial Photosynthesis.

3.3.2 Characterization Techniques

3.3.2.1 Morphology

Co_3O_4 is a semiconductor with a normal spinel structure where Co^{2+} ions exist in tetrahedral interstices while Co^{3+} ions exist in octahedral interstices along the cubic close-packed lattice structure of O^{2-}. [64] The unit cell for Co_3O_4 is given in Fig. 3.4. The film thickness of the sputtered Co_3O_4 films was estimated with a Dektak IIA profilometer for 50 nm or thicker films. A 10 nm film was determined based on the estimated sputter rate and deposition time and in agreement with absorbance measurements using Beer's Law. The crystal structure was characterized using Bragg-Brentano focusing powderXRD with Cu Kα radiation from a Rigaku SmartLab X-ray diffractometer (Rigaku Americas, The Woodlands, TX). Scanning electron microscopy (SEM) measurements were conducted on an FEI Quanta FEG250 (FEI, Hillsboro, OR), operating at 10 or 20 kV and a working distance of 9.8 mm.

Both XRD patterns and SEM images were obtained in order to show the distinct differences in film quality dependent on substrate (Fig. 3.5). Polycrystalline Co_3O_4 was formed when sputtered on quartz or ITO, which gives multiple crystalline directions such as (111), (311), (222), and (511). When Co_3O_4 was sputtered on top of $MgAl_2O_4$ (110), an epitaxial film formed with only one crystalline face and oriented in the (220) and (440). This is due to the minimal mismatch between the lattice constants of the two materials. [65] The crystal directions (h k l) (blue lines) are referenced from the 2012 International Cen-

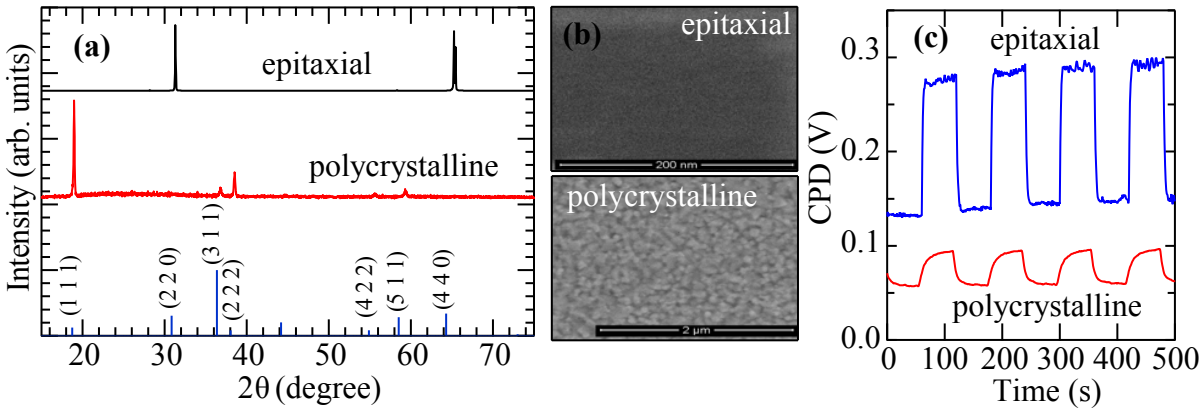

Figure 3.5: (a) XRD patterns, (b) SEM images and (c) SPV for epitaxial and polycrystalline Co_3O_4 thin films.

tre for Diffraction Data PDF Card 04-014-7784 for Co_3O_4. [66] The polycrystalline films yield a domain size (D_p) of roughly 20 nm based on the Scherrer equation. SEM images provide further evidence of the crystallinity differences. The polycrystalline film yields multiple grain boundaries while the epitaxial film has no noticeable features even at 200 nm resolution. Additionally, a comparison of the SPV, measured using CPD measurements, highlights the large difference in surface morphology between the epitaxial and polycrystalline films (Fig. 3.5c). Larger photovoltages are obtained for the epitaxial film suggesting better passivation of the surface while the polycrystalline films give more transient behavior suggesting carrier trapping processes. A solution of 250 μM 20 nm Co_3O_4 nanoparticles with an organic precursor were dropcast on a quartz substrate and used as received from the Heinz Frei group at Lawrence Berkeley National Laboratory for further morphological comparisons. The organic precursor was removed with high temperature (350°) calcination for 48 hours to give 20-50 nm film thicknesses.

3.3.2.2 Electrochemistry

(Photo-) and (spectro-)electrochemical measurements were performed in a Teflon electrochemical cell with CaF_2 optical windows at room temperature. The electrolyte is 0.1 M NaOH electrolyte solution and an area of ~0.50 cm^2 Co_3O_4 was exposed. A CV and Mott-Schottky plot are shown in Fig. 3.6 to identify some material properties of Co_3O_4. The CV was taken with a 20 mV/s scan rate at 0.001 V sample intervals. The principal anodic peak with an onset at about 0.60 V is associated with the oxygen evolution reaction. The CV curve is consistent with previous measurements on Co_3O_4. [63] The Mott-Schottky plots, scanned from -0.6 V to 0 V with 0.1 V amplitude signal at 100 Hz frequency, show a V_{FB} of -0.14 V vs Ag/AgCl based on the intercept of a best fit line. Additionally, the slope yields an intrinsic hole doping of 5×10^{21} cm^{-3}, leading to roughly 1% Co vacancies.

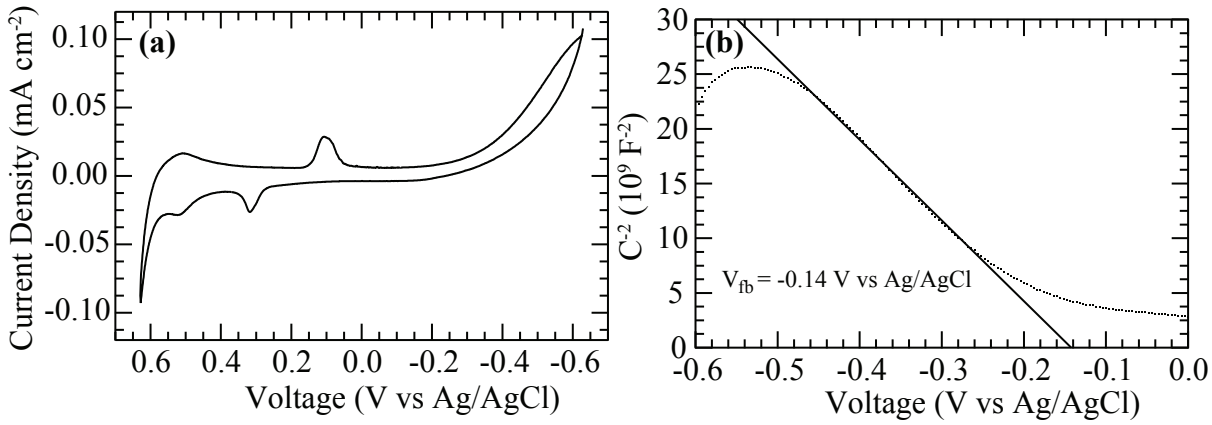

Figure 3.6: (a) CV curve and (b) Mott-Schottky plot of a $d \sim 10$ nm Co_3O_4/ITO.

3.3.2.3 Absorbance spectrum

The electronic, magnetic, and optical properties of Co_3O_4 have been extensively studied by several groups, but both theory and experiments have yet to agree on the correct energy band gap. [64, 67–70] The optical spectrum of Co_3O_4 was characterized using a Shimadzu UV-2600 spectrophotometer (Shimadzu Scientific Instruments, Columbia, MD). The infrared spectrum of Co_3O_4 was characterized by Fourier-transform infrared spectroscopy using a Bruker Vertex 70V (Bruker Optics Inc.; Billerica, MA). As shown in Fig. 3.7, and in good agreement with previous reports [67–69, 71], the static absorption spectrum of Co_3O_4 exhibits two strongly absorptive bands (2.84 eV, 1.66 eV) and two weaker absorptive bands (0.94 eV, 0.82 eV). Miedzinska *et al.*'s [71] semi-empirical molecular orbital treatment assigns the peaks to specific excitations. They attribute the 436 nm (2.84 eV) band to LMCT between O 2p $\rightarrow$ Co^{2+} d metal centers. The 745 nm (1.66 eV) band is identified as MMCT from Co^{3+} d $\rightarrow$ Co^{2+} d, creating an oxidized Co^{4+} and a reduced Co^{1+} in the excited state. The band at 1323 nm (0.94 eV) is associated with the reverse process (Co^{2+} d $\rightarrow$ Co^{3+} d) that flips the oxidation states such that, in the excited state, a Co^{3+} occupies a tetrahedral site and Co^{2+} occupies an octahedral site. Finally, the feature at 1505 nm (0.82 eV) is due to the ligand field transition in tetrahedral Co^{2+} (Co^{2+} d $\rightarrow$ Co^{2+} d). The two lower energy bands at 1323 nm (0.94 eV) and 1505 nm (0.82 eV) are described as localized *d-d* transitions. They are differentiated from the two higher energy CT bands by their weaker absorptivity and narrow spectral range. The intra-valent d-d transitions are normally forbidden due to dipole selection rules. However, a non-zero transition matrix element can occur between the initial and final states due to hybridization of the O $2p$ and Co $3d$ orbitals which will relax the parity selection rule and result in a non-zero transition probability. The result is a small matrix element leading to a small absorption intensity. The transient spectra and kinetics discussed below report on these selectively pumped transitions, as indicated by the arrows

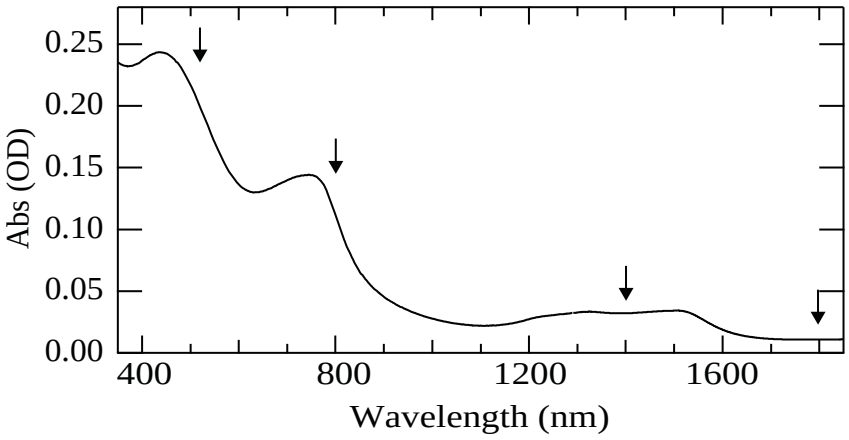

Figure 3.7: UV-vis-IR absorption spectrum of a 10 nm Co_3O_4 film. The arrows indicate the excitation wavelengths employed in the TA experiments.

Table 3.1: Co_3O_4 absorptions and corresponding transitions.

Wavelength (nm)	Energy (eV)	Transition	Type
436	2.84	O 2p $\rightarrow$ T_d Co^{2+} d	LMCT
745	1.66	O_h Co^{3+} d $\rightarrow$ T_d Co^{2+} d	MMCT
1323	0.94	T_d Co^{2+} d $\rightarrow$ O_h Co^{3+} d	MMCT
1505	0.82	T_d Co^{2+} d $\rightarrow$ T_d Co^{2+} d	Intravalence

in Fig. 3.7.

3.4 Results

3.4.1 Transient spectrum

While 520 nm produces electron-hole pairs across all major optical transitions, 800 nm light selectively excludes the LMCT transition and 1400 nm selectively excites carriers across only the two weaker *d-d* transitions. 1800 nm excites below all the transitions. Despite exciting selective transitions with drastically varying absorbance intensities, these four pump wavelengths produce transient spectra of similar shape at a 3 ps delay time as shown in Fig. 3.8 (a). This unique response is discussed in terms of an intrinsic, low-lying energetic manifold of *d* states. Although excitation below this density of states produces the same spectrum, two-photon absorption can explain the response at 1800 nm and will be discussed further below. Additionally, the transient spectrum maintains the same shape through the nanosecond time scale (Fig. 3.8(b)). The spikes at $\sim$520 nm are due to leakage of the pump

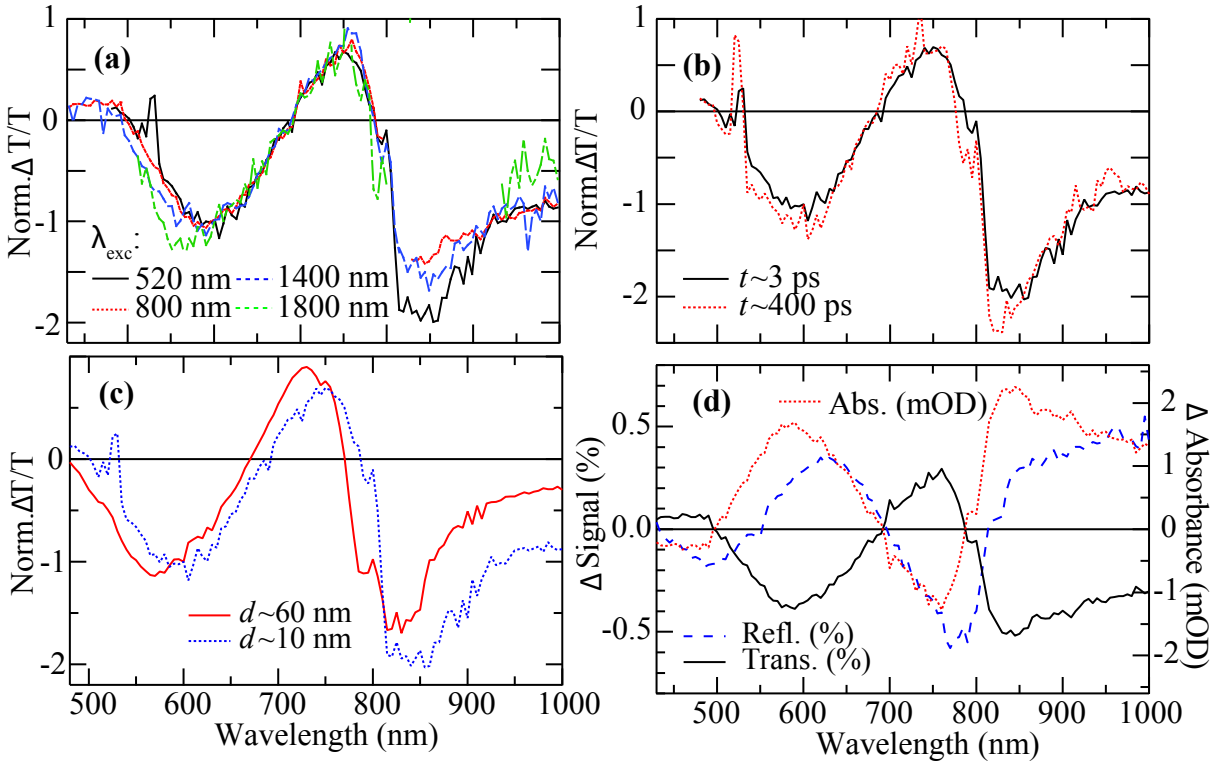

Figure 3.8: Transient transmittance spectra of Co_3O_4 (a) excited at different wavelengths at $t \sim 3$ ps, (b) excited at 520 nm at two different pump-probe delay times t and (c) excited at 520 nm, $t \sim 3$ ps at two different thicknesses d. (d) Comparison of transient transmittance, reflectance, and absorbance spectra at $t \sim 3$ ps of a $d \sim 10$ nm Co_3O_4/quartz. $\lambda_{exc} = 800$ nm.

into the detector. Most data, unless otherwise noted, were collected for either ∼10 nm film or ∼60 nm film of Co_3O_4 on a ∼1 mm quartz substrate in air. While both films exhibit a similar transient spectrum in the UV-vis region (Fig. 3.8c), only in the thicker ∼60 nm film can the transient response be detected in the NIR region. Although the spectral shape is thickness independent, there is a small blue shift with increased thickness. A blue shift is generally associated with a Burstein-Moss shift where occupation of electrons in the conduction band causes the band gap energy to "appear" higher in energy. [72] However, this is not believed to be the case and the reason for the shift is explained based on the spectro-electrochemistry data below. Fig. 3.8(d) highlights the relationship between the reflectance, transmittance, and absorbance transient spectra. For our ∼10 nm films, the transient reflected spectral response is nearly a mirror image of the transmitted response. Therefore, the transient response is described as a change in the absorptive property of the film, through the application of Beer's law. Since both the ∼10 nm and ∼60 nm films exhibit the same transmitted spectrum in the UV-vis region, the transmitted response of the thicker

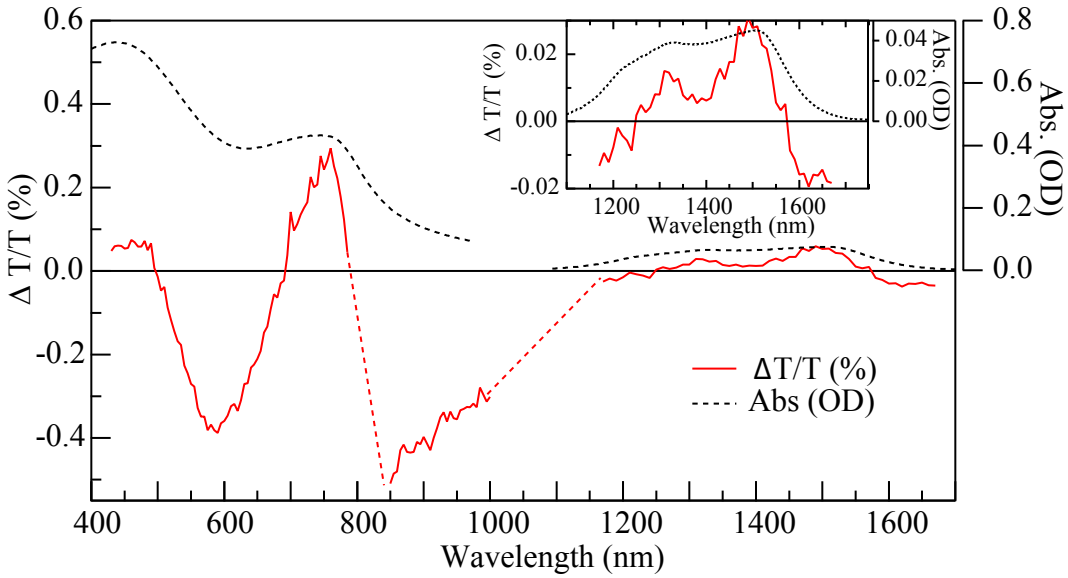

Figure 3.9: Comparison of the transient transmittance (λ_{exc} = 800 nm) with the static absorbance spectrum. For clarity, the inset shows the same data in the region. The red dotted lines were introduced to guide the eye.

films is interpreted in the same manner.

In order to investigate the role of the *d*-*d* transitions, the probe wavelength was extended to the NIR region. As shown in Fig. 3.9, when electrons are excited above the first CT transition (λ_{exc} = 800 nm), the *d*-*d* transitions in the 1300-1500 nm region exhibit a positive change in transmittance, *i.e.* a bleach. Excitation at longer wavelengths is more difficult due to lower signal levels from the lower absorption coefficient. This is in contrast to a large extent of the visible region where excitation results in a negative transmittance change, or new absorptions. Further, the bleach shape mirrors the characteristic double peaks of the *d*-*d* transitions when the long tail due to the lower charge transfer transition is subtracted from the static optical spectrum to emphasize the *d*-*d* transitions (Fig. 3.9 inset). Due to the weak extinction coefficient of the *d*-*d* transitions, the transient spectra were taken with an ∼60 nm film rather than the ∼10 nm film used in the spectral region of the CT transitions. In Fig. 3.9 the responses of the ∼10 nm and ∼60 nm film were scaled to the same absorbed excitation fluence such that the magnitudes in the two spectral regions can be directly compared.

3.4.2 Spectro-electrochemistry

Spectro-electrochemical measurements fill unoccupied and occupied states with electrons and holes, respectively, by applying a voltage on a film in an electrochemical cell while a static UV-vis spectrum is recorded. Static spectra were taken ∼1 minute after potential

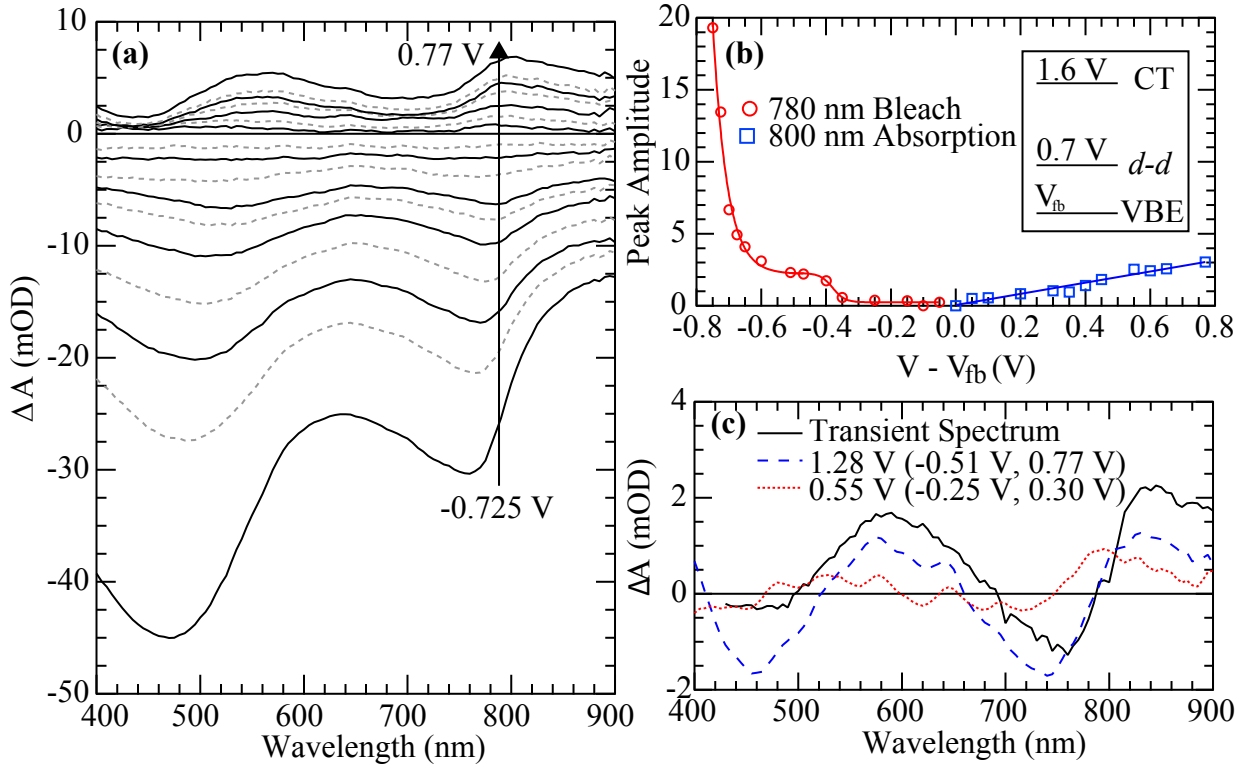

Figure 3.10: (a) Differential spectrum for applied potentials with respect to V_{fb}. (b) Peak amplitudes of ∼800 nm absorption and ∼780 nm bleach peaks as a function of V - V_{fb}. Solid lines were introduced for clarity. Inset: Band diagram of Co_3O_4 where V_{fb} is taken as 0 V. VBE is the valence band edge. (c) Comparison of the sum of the spectro-electrochemically obtained hole and electron spectra with the transient optical spectrum.

was applied to allow for equilibration. Given the weak nature of *d-d* transitions, spectro-electrochemistry [72–74] utilizes the spectral regions with stronger absorptivity in order to follow the occupation of the weaker *d-d* transitions by providing a well-defined potential that assesses those infrared electronic states. Such measurements can help interpret the transient spectrum of TMOs, as has been previously shown for Fe_2O_3. [51, 75]. The differential spectra, obtained by subtracting the spectrum at the flatband potential (*i.e.* V_{FB}) from the spectrum at a different applied bias ranging from 0.77 V to -0.725 V are shown in Fig. 3.10 (a) across the spectral region of the CT transitions. According to the Mott-Schottky plots and in agreement with previous studies, V_{FB} is -0.15 V vs Ag/AgCl. [63] Hole injection at positive potentials gives rise to new transitions, leading to pronounced absorbance peaks at 800 nm and 560 nm. On the other hand, the spectra for electron injection at negative voltages are characterized by bleaches at 780 nm and 500 nm. Direct spectro-electrochemical experiments probing the *d-d* transition was not possible due to absorptions by the electrolyte. However, using a monochromatized Xenon lamp output with lock-in detection, two points at 1300 nm

were acquired for hole and electron injection. At comparable voltages, a new absorption and a bleach were observed, consistent with the trend in the spectral region of the CT transitions. In addition to the increasing intensity of absorbance and bleach peaks, there is a notable blue shift in the max bleach peak with increasing negative potential. This is in contrast to the minimal change in the wavelength of the max absorption peak observed. As mentioned earlier, blue shifts are generally associated with Burstein-Moss shifts. However, because Co_3O_4 is a p-type semiconductor with an assumed 1.6 eV band gap and a flatband potential taken as the valence band edge (VBE), the applied biases should not be enough to reach the conduction band. Therefore, the onset of the blue-shift observed at ∼-0.7 V is consistent with assignment to occupation of *d* states. This can also explain the blue shift observed in the transient spectrum of the thicker film in which more electrons are occupying the *d* states than in the thin film.

The relationship between the applied voltage and the electronic states in Co_3O_4 is based on the location of V_{FB} and shown schematically in the inset of Fig. 3.10(b). Since Co_3O_4 is highly *p*-type, the V_{FB} corresponds to the VBE. At applied biases negative of V_{FB} (*i.e.* electron injection), previously unoccupied states within the band gap are filled with electrons, which results in a bleach. Here, the band gap is defined as the 1.6 eV transition. For voltages positive of V_{FB} (*i.e.* hole injection), holes fill previously occupied states below V_{FB} causing new absorptions. Fig. 3.10(b) plots the amplitude of the 800 nm absorption peak and the 750 nm bleach peak as a function of V-V_{FB}. While hole injection leads to linearly increasing absorption peaks with applied voltage, electron injection grows nonlinearly. A minimum voltage is required before the bleach increases significantly in magnitude. The onset voltage for electron injection is necessary in order to reach the unoccupied states within the band gap, whereas hole injection can occur for any voltage positive of V_{FB}. Following the 780 nm bleach peak with applied potential, the major onset for electron injection occurs at ∼-0.7 V from V_{FB}, close to where the intraband *d* states are expected optically. A minor onset also appears at ∼-0.4 V, which may be associated with the tail edge of these *d* states or surface specific *d*-*d* transitions. [76, 77]

As shown in Fig. 3.10(c), the sum of the hole and the electron spectra obtained through spectro-electrochemistry agrees with the overall shape of the transient optical spectrum. The two distinct absorptions in the transient optical spectrum are assigned, then, to hole-induced absorptions, while the bleach at 750 nm is assigned to an electron-induced bleach. At sufficiently negative potentials, there is a large density of intraband states that become occupied. These states are most likely the Co *d* states that lie ∼-0.7 V above the flatband potential. Further, the electron and hole injection voltages required to make a reasonable agreement with experimental transient optical spectrum are at -0.51 V and 0.77 V, respectively, or an energy difference of 1.28 eV. Higher energy differences also reproduce the transient spectrum, but voltage differences lower than the energies of the *d*-*d* transitions (*e.g.*, 0.55 eV) do not.

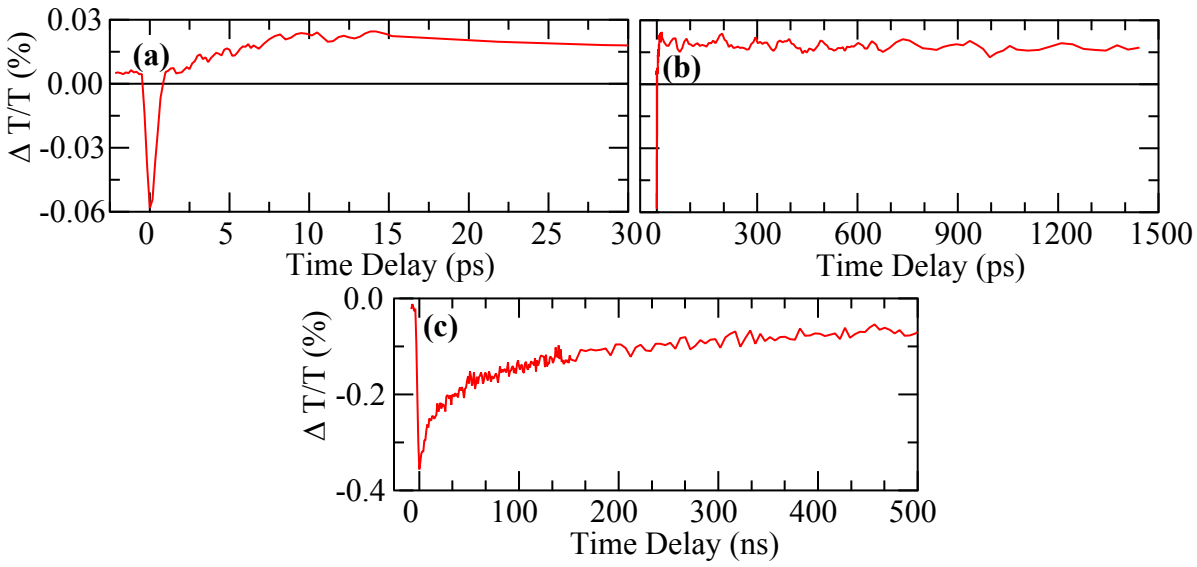

Figure 3.11: Transient decays of the signal at 1320 nm for a ∼60 nm film at (a) early and (b) later delay times (λ_{exc} = 800 nm). (c) Decay of the signal probed at 830 nm on a nanosecond time scale (λ_{exc} = 520 nm).

3.4.3 Transient decays

The transient decay of photoexcited carriers for an ∼60 nm thick film is illustrated in Fig. 3.11. The kinetics exhibit three components when probed at 1320 nm: an initial, fast 1-2 ps absorption (Fig. 3.11(a)), followed by an ∼5 ps rise of a bleach (Fig. 3.11 (a)), and a subsequent decay of a bleach on the nanosecond time scale (Fig. 3.11(b)). While the bleach corresponds to the one in the transient spectrum shown in Fig. 3.9, the fast (<2 ps) component has a distinctly different spectrum. This fast phase is always absorptive with a more pronounced absorption at longer probe wavelengths all the way through the *d-d* transitions (Fig. 3.12). Time zero was arbitrarily defined as the time just before the signal rise. The full decay of the slower time scale is shown in Fig. 3.11(c) and extends for nanoseconds. A fit by a stretched exponential yields a time constant of τ = 67 ns with α = 0.46. Probing this longer decay required using a diode laser as a probe in order to control the delay electronically. As a result, a probe wavelength of 830 nm was used instead of 1320 nm. Although this wavelength does not directly probe the *d-d* region, the decay time scale is insensitive to an extensive probe wavelength range, as shown in Fig. 3.13a. In addition to probe wavelength, the transient decays are also insensitive to pump wavelength, pump fluence and morphology according to Fig. 3.13b, c, and d, respectively. Interestingly, the decay kinetics are independent to the defects and impurities of the material as shown in the comparison of epitaxial, polycrystalline and nanoparticle Co_3O_4.

The calculation for the fraction of carriers excited for the *d-d* transitions is determined next based on pump probe experiments on the 100 nm Co_3O_4 films excited at 800 nm.

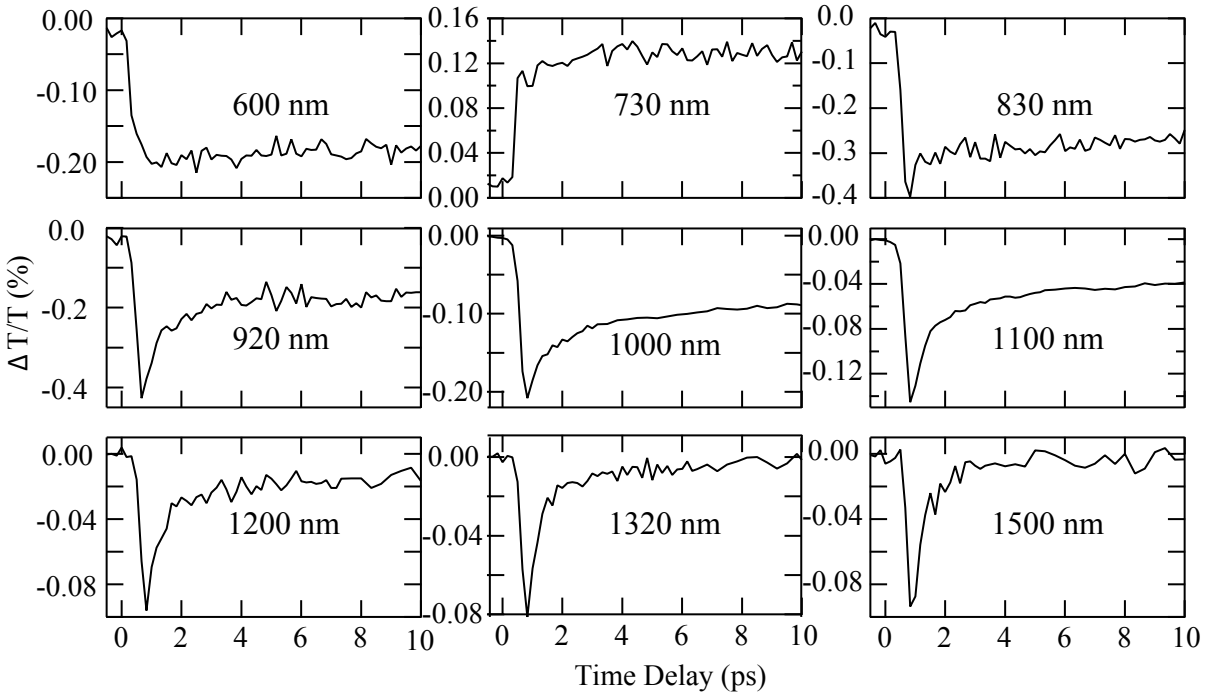

Figure 3.12: Probe wavelength dependence of transient transmittance signal at early times for a ∼10 nm Co_3O_4/quartz. $\lambda_{exc} = 800$ nm.

First, the experimental percentage change is determined first. Probing at 1310 nm, the Δtransmittance signal is 1.67% which is ΔOD = -log(1+0.0167) = -0.0072. Since the optical density (OD) at 1310 nm is 0.389 according to UV-vis measurements, the fraction excited is calculated to be $\frac{\Delta OD}{OD} = 1.85\%$. Based on the maximum absorbed fluence ($F_{abs} \sim 7$ mJ cm^{-2}), a carrier density of $\sim 2.75 \times 10^{21}$ cm^{-3} is expected. The percentage of carriers excited per valence electron density is ∼0.35%. Therefore, the change in OD is much larger than what is estimated from the number of created carriers. The reason for the higher OD may be a result of smaller valence electron density than theoretically calculated due to surface defects and impurities. Using the experimental percentage, it is calculated that there are ∼19% fewer valence electrons.

Looking at the dependence of the ΔT/T signal with carrier density yields interesting behavior (Fig. 3.14). At excitation wavelengths of 520, 800, and 1500 nm, the signal is linear. At excitation wavelengths longer than the *d-d* transitions, *i.e.* 1700, 1800, and 2000 nm, where the signal is expected to disappear or change significantly, a quadratic dependence is observed. The larger than expected increase in signal with fluence is possibly due to two-photon absorption. Based on a two-photon absorption of 2000 nm light, this equates to a 1.24 eV transition which is consistent with the 1.28 eV energy difference determined with spectro-electrochemical measurements. As 1700 nm also shows quadratic behavior, a band

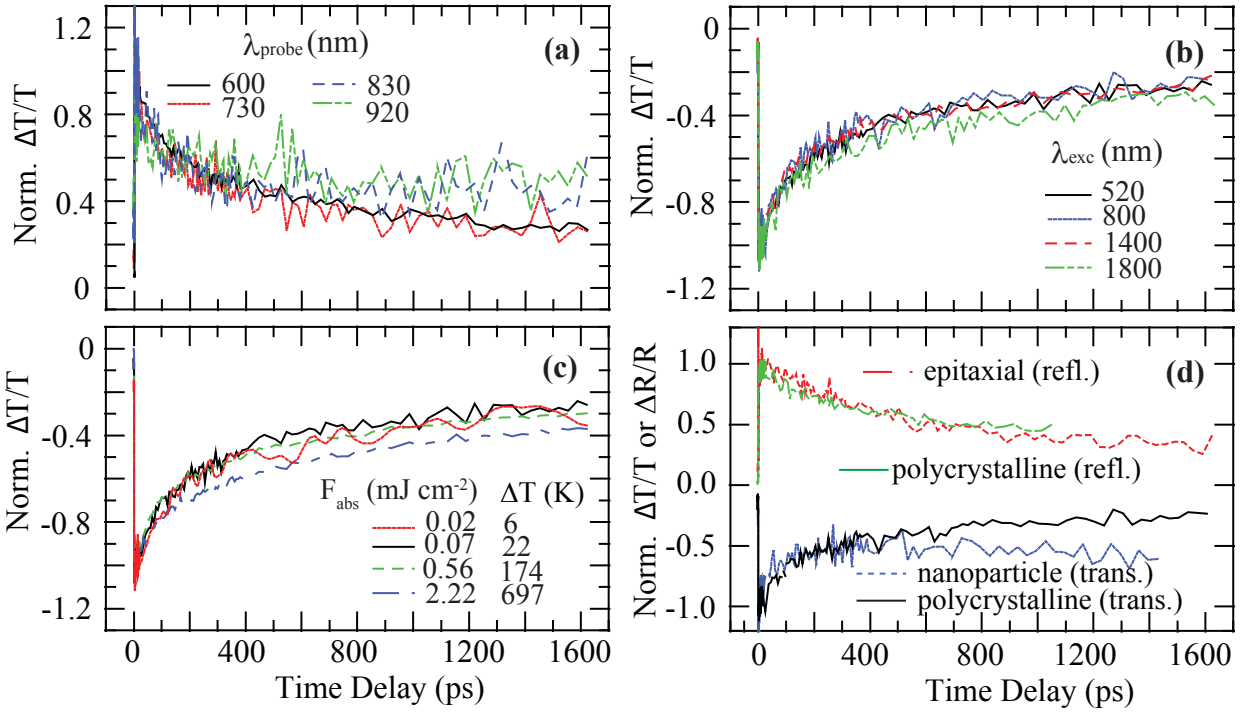

Figure 3.13: Transient transmittance decays (a) probed at different wavelengths, (b) excited at different pump wavelengths and (c) excited at different absorbed pump fluences. λ_{exc} = 520 nm and λ_{probed} = 600 nm unless otherwise mentioned. (d) Transient reflectance changes for an ∼60 nm epitaxial film of $Co_3O_4/MgAl_2O_4$ and a polycrystalline film on glass of similar thickness and transient transmittance changes for an ∼20 nm drop-casted nanoparticle film of Co_3O_4 on quartz and an ∼10 nm polycrystalline film. λ_{exc}=800 nm.

of states approximately 0.22 eV in width exists.

Another interesting property is observed when varying the film thickness. A comparison of the kinetics between a 10 nm and a 200 nm Co_3O_4 film suggests bulk versus surface sensitivity between transmittance and reflectance, respectively. As expected, for the 10 nm film, the transmitted and reflected kinetics are the same. However, for the 200 nm film, the transmitted signal decays on a longer time scale than that observed in the 10 nm films and additionally there is a significant difference with the reflected signal. This behavior is attributed to the sensitivity of the detection mode to either bulk or surface properties, to be discussed below.

3.5 Discussion

Taken together, the results demonstrate that *d-d* transitions in the spinel compound Co_3O_4 serve as a special type of recombination center intrinsic to the electronic structure.

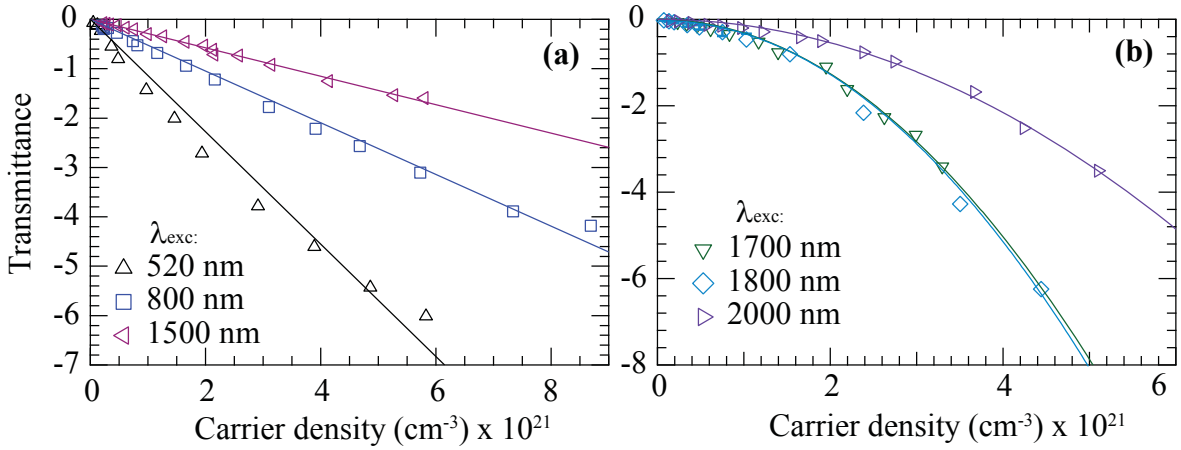

Figure 3.14: Transient transmittance taken at 600 nm and 5 ps time delay with respect to carrier density (cm^{-3}) at excitation wavelengths of a) 520, 800, 1500 nm showing linear dependence and b) 1700, 1800, and 2000 nm showing quadratic dependence.

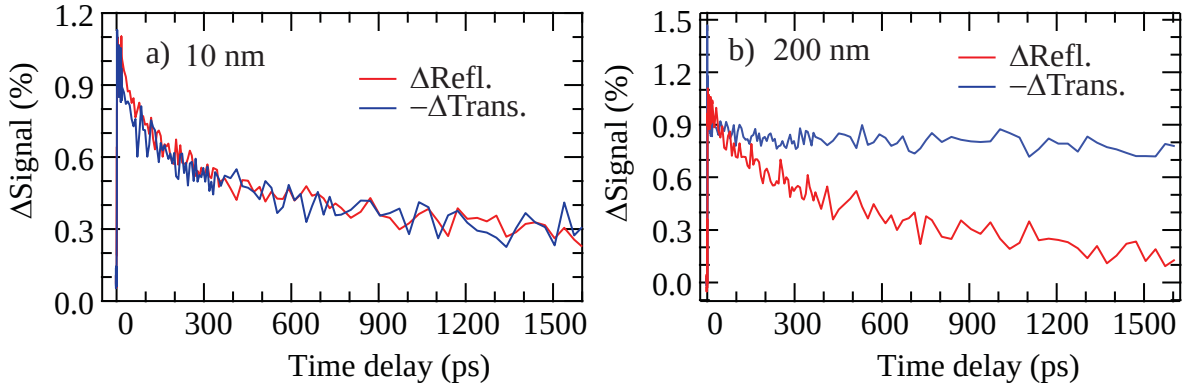

Figure 3.15: Transient transmittance and reflectance comparison taken at $\lambda_{exc} = 580$ nm and probed at $\lambda = 620$ nm for a) 10 nm and b) 200 nm film.

This recombination centre traps photoexcited electron-hole pairs within ∼3 ps. The trapped carriers finally recombine on the nanosecond time scale. Given this interpretation of the photoexcited carrier dynamics, the transient decays are assigned to specific processes. The fast, ∼2 ps component is ascribed to hot carrier cooling or intraband thermalization within the higher lying CT transitions. The absorptive trend observed with longer probe wavelengths is characteristic of Drude-like behavior. The following ∼5 ps rise of the bleach corresponds to the capture of photoexcited carriers to the unoccupied d states. Lastly, the slower, nanosecond component is assigned to recombination from the excited d states to the ground state. A schematic of this interpretation is provided in Fig. 3.16. The slower, probe wavelength independent decay is consistent with carrier recombination from a manifold of trap states, as observed in nanoparticle ZnO films [50], α-Fe_2O_3 epitaxial thin films [51, 78, 79] and colloidal nanoparticles [46, 51] and nanocrystalline TiO_2 films [80] and powders [58].

3.5.1 Long-lived Localized d-d Excitation

As mentioned previously, in ferromagnetic manganite a long-lived decay was observed for the dipole and spin forbidden d-d transition between spin split e_g levels and attributed to the coupling of excited d carriers to low energy spin waves. [55] Finding a long-lived d-d transition in Co_3O_4 suggests the extended lifetime may be more general, appearing in materials without specific magnetic excitations. As opposed to CT transitions, localized d-d transitions modulate the charge distribution in the lattice weakly, and therefore are expected to couple weakly to modes of the extended lattice, be they phonons or magnetic excitations. These findings are also consistent with previous suggestions that the long-lived excitations in Fe_2O_3 may result from intrinsic "mid-gap" states. [46, 49, 51, 75]. Two additional pieces of evidence for the assignment to localized d-d excitations are the direct measurement of the ground state bleach of the d-d transitions in the transient absorption spectrum and the ability to mimic the transient spectrum in the CT region with voltages that selectively fill these d states electrochemically.

The agreement between the transient absorption spectrum and the difference spectrum obtained electrochemically is surprisingly good. However, it is important to note that the bleaches in the spectral range of the CT region are not explainable in a purely state-filling picture that would ascribe them directly to Pauli blocking of those CT states. Rather, it is state filling of the lower energy d-d transitions that leads to the bleaches, which can be interpreted in terms of a polaronic effect in conjunction with state-filling. Localization of photoexcited carriers within the d states creates a polaron. The polaron induces changes in the local electric field by carrier-lattice interactions that modulate the hybridization of the d orbitals with O $2p$ orbitals. This modulation can affect all electronic transitions in the spectrum and lead to the observed bleaches in the CT region.

One qualification for the localized d manifold interpretation relates to the presence of a dominant defect, Co-vacancies, among all the different morphologies of thin film Co_3O_4 tested. Transition metal ion vacancies in thin film oxides are thought to be responsible for their substantial p-doping. Since our Co_3O_4 films are highly p-doped, there exists a dense

population of states near the VBE occupied by electrons at room temperature. [81, 82] Therefore, these Co-vacancies most likely trap holes from the VBE, contributing to the hole component of the transient spectrum and leading to hole hopping prior to recombination with electrons sitting at the *d-d* states. While this does not directly interfere with the consistency of the interpretation presented, single crystal studies of similar $3d$ transition metal oxides could clarify the effect of metal vacancies on the kinetics to discriminate between CT and *d-d* transitions.

As the rate constant is independent of pump fluence, it excludes the most common recombination mechanisms, *e.g.* bimolecular and Auger recombination. These mechanisms should show a nonlinear dependence on carrier density, rather than a linear dependence as shown in Fig. 3.14a. Secondly, traditional absorption theories for semiconductors suggest a strong dependence should occur based on which region of the Brillouin zone is being pumped. Since this is also not the case, a thermal response might be considered. Fast trapping by deep traps can be facilitated by multi-phonon emission and under certain conditions lead to an independence from carrier density. [83] Energy transfer to the lattice can cause band gap renormalization that could cause a change in the transient spectrum as previously reported for GaAs and Si. [84] However, the temperature change associated with the absorbed excitation fluence is minimal based on the following calculations using

$$\frac{F}{d} = \frac{Q}{V} \quad (\frac{mJ}{cm^3}) \tag{3.4}$$

where F and d are the absorbed fluence and film thickness, respectively and $\frac{Q}{V} = \Delta T \cdot C_p$ where C_p is the heat capacity ($J\ K^{-1}\ cm^{-3}$). Since C_p is 123.2 $J\ K^{-1}\ mol^{-1}$ for Co_3O_4 at room temperature and there are 0.0259 mol Co_3O_4 cm^{-3}, the molar heat capacity is 3.19 $J\ K^{-1}\ cm^{-3}$. [85] For a typical absorbed pump fluence of 0.1 mJ cm^{-2} and d = 10 nm, the upper limit for ΔT is 31 K, assuming that the total absorbed energy is instantaneously released into the lattice. At the lowest 520 nm pump fluence of 0.019 mJ cm^{-2}, ΔT is only 6 K. As no change is observed within this fluence range, despite the large temperature differential, a thermally induced transient change is ruled out.

3.5.2 Surface vs Bulk Effects

The spectroscopic results also suggest a certain level of surface sensitivity for the 10 nm films in both transmittance and reflectance mode where the charge dynamics originate from surface *d-d* transitions rather than bulk effects. In contrast to the transmittance, a reflectance signal arises primarily from the surface. The surface reflected wave has to interfere constructively with the waves penetrating from inside the film. The effective probe depth in reflectance usually goes as $\alpha = \frac{\lambda}{4\pi n}$ where n is the real part of the refractive index. This is approximately 20 nm at a 620 nm probe wavelength. As this probe depth is greater than the sample thickness, the transmitted and reflected kinetics are the same in the 10 nm films. However, this surface sensitivity explains the differences in timescales observed between reflectance and transmission modes for the thicker Co_3O_4 films (Fig. 3.15). For the 200 nm

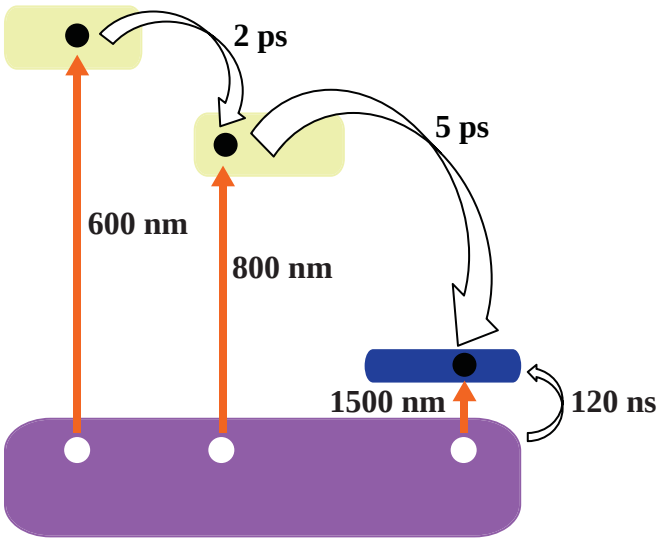

Figure 3.16: Schematic of Co_3O_4 proposed relaxation dynamics.

film, the reflected signal decays on a relatively fast time scale similar to the 10 nm films while the transmitted intensity decays on a much longer time scale. The kinetics do not depend on surface preparation as discussed previously in the comparison of the different film morphologies nor is it affected by the electrolyte in contact with the surface. As a result, the faster dynamics can not be attributed to extrinsic factors, such as charge transfer to different surface adsorbates. Rather, the sensitivity to structural differences originating from intrinsic surface d states are enhanced with reflectivity and thinner films in Co_3O_4. The faster decay kinetics are attributed to surface recombination at these localized trap states while the longer time scale reflects bulk properties of the film that could arise due to bulk recombination, carrier diffusion or a combination of both. Additionally, the shoulder observed at ∼-0.4 V in Fig. 3.10b suggests the presence of a mid-gap density of surface states while the ∼-0.7 V may be the direct fundamental band gap of Co_3O_4 as previously suggested by both theory and experiments. [86, 87]

3.6 Conclusion

In conclusion, the photoexcited carrier dynamics of Co_3O_4 show a unique insensitivity to a number of tuning parameters. The transient optical spectrum and transient kinetics are insensitive to excitation wavelength, pump-induced carrier density and probe wavelength across all the major optical transition types, indicating that electron-hole pairs must thermalize to a manifold of states at an energy lower than the CT transitions within ∼3 ps. This manifold of states is intrinsic to Co_3O_4 and attributed to d states with an energetic location

of approximately 0.7 eV above the VBE. Acting as efficient hole traps that can oxidize the Co atom, these *d* states further suggest that the proposed Co(IV)=O species is a likely intermediate in the water oxidation reaction. The long lifetime of the photoexcited *d* states in Co_3O_4 suggests *d*-*d* transitions, which are universal to many TMOs, could more generally be utilized for NIR absorption in photovoltaic and photocatalytic devices. These *d*-*d* transitions are optically accessible in the NIR with an absorption coefficient of $\sim 10^3$ cm^{-1}, on par with above band gap absorption in silicon, the lowest transition of semiconductor quantum dots, and semiconductor plasmons. [88–90] As these results are the first to characterize the carrier dynamics of Co_3O_4, this study complements future studies that employ Co_3O_4 anode composites for water oxidation catalysis. Additionally, with the goal of manipulating the kinetics of Co_3O_4, a proposed heterojunction can be engineered with Co_3O_4 in order to isolate the hole dynamics from the recombination kinetics by utilizing a built-in electric field. This is briefly addressed in Appendix A using a Co_3O_4/ZnO heterojunction.

Chapter 4

Probing Electronic Structure with L-edge X-ray Absorption Spectroscopy

Portions of the content and figures of this chapter are reprinted or adapted with permission from A.M. Hibberd, H.Q. Doan, E.N. Glass, F.M.F. de Groot, C.L. Hill, and T. Cuk, J. Phys. Chem. C 119, 4173 (2015).

4.1 Introduction

A general strategy often employed in the performance optimization of oxygen evolving catalytic systems is tuning the electronic properties through doping, alloys, heterojunctions and structural modifications. [30, 91–95] For example, $LiCoO_2$ and $LiCoPO_4$ are tunable via delithiation. [96–98] There are also a variety of other cobalt (Co)-containing materials that have emerged as some of the more promising systems for solar fuel devices. They range from heterogeneous electrodeposited Co-phosphate [99] and Co_3O_4 nanoparticles [20, 45] to homogeneous CoPOMs. [100, 101] Although the active catalytic center is the Co ion, identifying the exact active structure responsible for the catalytic activity is still largely debated as is the mechanism by which these centers are able to catalyze the water oxidation reaction. To that end, a fundamental compare and contrast study of the ground state atomic and electronic structure among the broad range of Co-based WOCs serves as a good starting point for settling the debate and directing rational engineering. In particular, investigation of the $3d$ states, which generally make up the valence band maximum and serves as the driving force behind the oxygen evolution reaction, can help elucidate the structure-activity relation of the Co-based WOCs.

This next chapter reviews the XAS technique, which serves as a powerful, element specific tool for electronic structure characterization of the $3d$ states. A link to theory is made with simulated spectra from ligand field multiplet (LFM) calculations. The systems studied are a

Co_3O_4 thin film and a set of five closely-related POMs that vary according to the number and position of Co sites, the Co valence state, and the coordination geometry of oxygen ligands surrounding the Co center(s) and heteroatom identity. These Co-based systems exhibit drastically different photocatalytic activities for water oxidation. Their detailed electronic structure are revealed with Co L-edge XAS spectra and discussed in the context of the atomic and ligand field parameters of the local Co environment. Further these parameters are extracted from the well-defined homogeneous POMs to simulate the more structurally ambiguous heterogenous Co_3O_4 thin film. Finally, the summary of results highlights the necessity for X-ray techniques even more sensitive to the $3d$ electronic structure in order to make a definitive statement about the structure-activity relationship.

4.2 X-ray Absorption Spectroscopy

The absorption of X-ray radiation by core electrons probes the unoccupied density of d states as shown schematically in Fig. 4.1. When an X-ray penetrates down to the core levels, a core electron can absorb the X-ray photon if the energy gain is equal to or higher than the energy difference between the initial and final state. The transition probability W_{fi} for this absorption process is described by Fermi's Golden Rule,

$$W_{fi} = \frac{2\pi}{\hbar}|\langle\phi_f|T|\phi_i\rangle|^2\delta_{E_f-E_i-\hbar\omega} \tag{4.1}$$

where ϕ_i and ϕ_f are the initial and final states, respectively. The conservation of energy is included by the delta function δ with E_f, E_i and $\hbar\omega$ as the final, initial, and incident

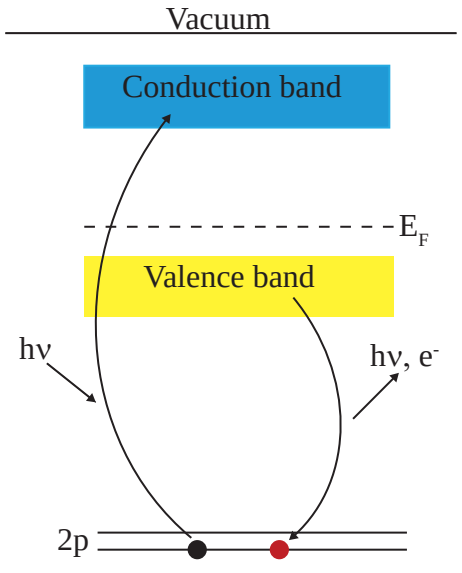

Figure 4.1: Schematic for XAS process.

energies, respectively. The transition operator T is related to the interaction Hamiltonian and contains the term e^{ikr} with k as the X-ray wave vector. As the wavelength of an X-ray photon is much larger than the typical size of an atom, the factor kr is $\ll 1$. Consequently, the transition operator turns into the dipole operator r using the Taylor expansion and based on the dipole approximation. Fermi's Golden Rule simplifies to

$$W_{fi} \propto |\langle \phi_f | r | \phi_i \rangle|^2 \delta_{E_f - E_i - \hbar\omega} \tag{4.2}$$

If the absorption process is allowed, *i.e.* $\hbar\omega$ is equal to the binding energy of a specific core state, a core electron is then excited to an empty state below the ionization threshold.The process of tuning the energy of the X-ray while measuring the product after the relaxation is XAS. Excitation results in an unstable state due to the presence of the core hole. That core hole is quickly filled by one of two decay processes that can be measured. Either a released photon or electron can be detected based on fluorescence or Auger decay, respectively. The limited femtosecond lifetime of the core hole broadens the peaks in the absorption spectrum according to the Heisenberg uncertainty relation.

K-edge XAS, which excites an electron from the 1s orbital to the delocalized, sp unoccupied continuum, has previously been employed to characterize the approximate oxidation state and local coordination environment of the Co-phosphate catalyst prior to and during catalytic water oxidation [102] and assess the stability of the homogeneous, soluble Co-based POMs [103, 104]. While these studies are informative of the local Co environment, K-edge XAS is unable to directly probe the $3d$ electrons integral to catalysis. The pre-edge peak of K-edge XAS does contain information about electron excitation from the 1s to the 3d Co orbital but this transition is dipole forbidden and results in a broad, weak and difficult to interpret peak. [102–104]

On the other hand, XAS at the 2s and 2p core levels, *i.e.* L-edge, excites $2p^6 3d^n \rightarrow 2p^5 3d^{n+1}$ transitions (where n is the number of d-electrons in the ground state), thereby directly probing the unoccupied density of d states. Two peaks arise in the L-edge XAS spectrum due to separation of the 2p states to $2p_{3/2}$ and $2p_{1/2}$ as described by the total angular momentum quantum number(J) and caused by core spin-orbit coupling (ξ_{2p}). These two J states are referred to as L_3 and L_2 and observed as the lower and higher energy peaks, respectively. There is significant overlap between the 2p core states and $3d$ valence states. Therefore, their interaction is strong and multiplet effects that form fine structure arise within the peaks of the XAS spectra. These multiplet effects are a signature of the spin and orbital momentum coupling of different $3d$ valence holes and from the coupled states formed between the $3d$ valence holes and the 2p core holes. This electronic fingerprint of the L-edge XAS contains a wealth of information about the ground state electronic structure. More specifically, the Co oxidation state, crystal field strength, electron-electron interactions and structural distortions can be extracted. For this study, only the fine structure of the L_3 is examined as it is more sensitive to multiplet effects than the L_2 peak. A more intensive theory of XAS is provided in [105].

Experimentally, the CoPOM crystals were spread directly onto conductive copper or carbon-based adhesive tape or pressed onto indium foil and affixed to a specially designed

beamline sample holder for X-ray analysis. The Co_3O_4 thin film on SiO_2 was also attached to the beamline sample holder with adhesive tape. A drop of conductive silver paste at the sample edge and holder supported conductivity across assembly. A cobalt foil reference was used for energy calibration. [106] The XAS experiments were performed at beamlines 7.0.1 and 8.0.1 at the Advanced Light Source at Lawrence Berkeley National Laboratory. The X-ray absorption process was measured using total electron yield (TEY) and total fluorescence yield (TFY) detection modes. The TEY signal originates from the cascade of secondary electrons created upon relaxation of the excited core-level electron, while TFY arises from the emission of a fluorescent X-ray photon upon relaxation. TEY was collected by measuring the sample drain current, and the TFY signal was acquired using a channeltron detector equipped with a negatively-biased grid to repel electrons ejected from the sample. The inelastic mean free path of electrons and photons determines the experimental probing depth, rendering TEY more surface sensitive, typically 4 nm, and TFY more bulk sensitive. [107] Therefore, TEY spectra are primarily reported, and only TFY is used when bulk sensitivity is required. The sample was positioned at $\sim$45° to the incident X-ray beam with an $\sim$30° angle between X-ray beam and channeltron detector. The analysis chamber was kept lower than 2.0×10^{-8} Torr during data acquisition. All spectra were normalized by I_0, the incident X-ray beam current as detected by gold foil upstream from the sample analysis chamber. Data were collected using beamline specific software and processed using custom panels in the Wavemetrics, Inc. Igor Pro 6.22A software.

4.2.1 Ligand Field Multiplet Theory

The LFM model approximates the transition metal ion as an isolated atom surrounded by a distribution of charges that are representative of the environment around the transition metal ion by applying a group theory treatment to the symmetry operations. [105, 108] With the aid of LFM calculations, one can analyze the electronic structure fingerprint that XAS spectra provide through the simulation of spectra consistent with observations in order to define the local properties of the active catalytic metal centers. [109–113] The Co 2p XAS process corresponds to $2p^63d^7 \rightarrow 2p^53d^8$ and $2p^63d^6 \rightarrow 2p^53d^7$ transitions for Co^{2+} and Co^{3+}, respectively. Spectra were calculated with the aid of CTM4XAS and CTM4RIXS [114], a freeware interface version of the Cowan-Butler-Thole code as developed by Thole et al. [115–117] LFM calculations are more representative of TEY detected spectra, since saturation effects can complicate TFY spectra, as suggested previously, so the XAS spectra were calculated to reproduce the experimental TEY spectra. [118, 119] For the experimental TFY spectra, reproduction was performed using a linear combination of 25% XAS and 75% resonant inelastic X-ray scattering (RIXS) spectra. Simulated XAS spectra take into account atomic multiplet effects, which determine how the molecular nature of the compound affects the atomic structure. Atomic multiplet effects are included by a reduction of the Slater integrals from their atomic values, introducing a ligand field, and adding charge transfer processes as needed. The Slater integrals represent the radial Coulomb repulsion between the core and 3d electrons $\langle 2p3d|\frac{1}{r_{12}}|2p3d\rangle$ (F_{pd}), the Coulomb repulsion of the 3d electrons

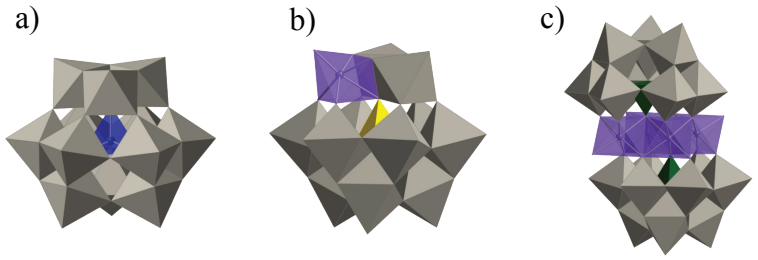

Figure 4.2: Polyhedral representations of POM analogues showing location and number of Co tetrahedra (blue), Co octahedra (purple), and tungstate octahedra (gray). Analogues studied include (a) T_d Co in a 2^+ or 3^+ oxidation state (b) O_h Co^{2+} with a neighboring Si heteroatom (yellow), and (c) four O_h Co^{2+} centers in the POM core with neighboring P or V heteroatoms (green).

$\langle 3d3d|\frac{1}{r_{12}}|3d3d\rangle$ (F_{dd}) and the exchange $\langle 2p3d|\frac{1}{r_{12}}|3d2p\rangle$ (G_{pd}) integrals in the presence of a core hole. Atomic values were used for ξ_{2p}, but were reduced from atomic values for the valence spin-orbit coupling (ξ_{3d}) depending on the spin interaction of the valence electrons. The ligand field, which accounts for solid state effects, is parameterized by crystal field splitting energy (10Dq), crystal field symmetry and axial distortion, Ds. To reproduce experimental spectra, it was unnecessary to explicitly include charge transfer states. Rather, such effects were implicitly accounted for by reduction of the Slater integrals. As the calculations do not result in an absolute energy value, simulated spectra are shifted to align with experimental spectra. Calculations are done at 300 K, and the resulting spectra are broadened to account for core-hole lifetimes and experimental resolutions, represented by Lorentzian, Γ, and Gaussian, G, functions, respectively. For this, we use half-width half-maximum values of $\Gamma(L_3)$=0.2 eV, $\Gamma(L_2)$=0.4 eV, and G=0.15 eV.

4.3 Properties of Cobalt Polyoxometalates and Co_3O_4

$K_5H[Co^{II}W_{12}O_{40}]\cdot 15H_2O$, $K_5[Co^{III}W_{12}O_{40}]\cdot 20H_2O$, $K_6[SiCo^{II}(H_2O)W_{11}O_{39}]\cdot 10H_2O$ and $Na_{10}[Co_4(H_2O)_2(RW_9O_{34})_2]\cdot nH_2O$ (where R represents phosphorus (P) or vanadium (V)) were synthesized based on published procedures in ambient amospheric conditions. [100, 101, 120, 121] All the reagents were purchased as analytical or reagent grade and used as received. Synthesis of the POMs was performed within Craig Hill's group at Emory University. Using coordination geometries, number of Co ions, valence states, and heteroatoms as identifiers, the POMs are labeled as T_d Co^{2+}, T_d Co^{3+}, O_h Co^{2+}, O_h $Co_4{}^{2+}P_2$ and O_h $Co_4{}^{2+}V_2$ where T_d denotes a tetrahedral geometry and O_h denotes an octahedral geometry. Representations of these POMs are shown in Fig. 4.2.

Each analogue was purified by recrystallization prior to use. Tetrahedral analogues were further purified using Dowex 50WX8 ion-exchange resin conditioned in the K^+ cycle prior

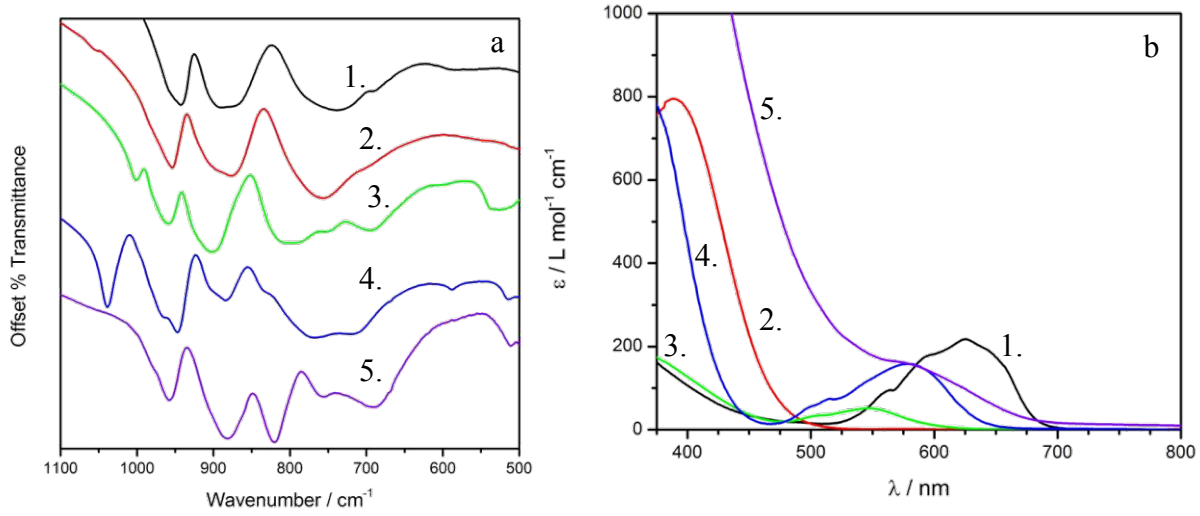

Figure 4.3: (a) IR and (b) UV-vis electronic absorption spectra of 1. T_d Co^{2+} (black) 2. T_d Co^{3+} (red) 3. O_h Co^{2+} (green) 4. O_h $Co_4{}^{2+}P_2$ (blue) 5. O_h $Co_4{}^{2+}V_2$ (violet)

to recrystallation. [122] The identities and purities of each compound were confirmed with UV-vis and infrared spectroscopy (Fig. 4.3). Infrared spectra (2% by weight in KBr) and the electronic absorption spectra were acquired using a FT-IR spectrometer (Nicolet 6700, Thermo Scientific, Waltham, MA) and spectrophotometer equipped with a diode-array detector (Agilent 8453, Agilent, Santa Clara, CA) and cell temperature controller unit (Agilent 89090A, Agilent, Santa Clara, CA), respectively.

Only the POMs with multiple Co sites within a single molecular structure are highly active WOCs. Yin *et al.* reports a turnover frequency of ≥ 5 s^{-1} for $Na_{10}[Co_4(H_2O)_2(\alpha\text{-}PW_9O_{34})_2]\cdot nH_2O$ while for $Na_{10}[Co_4(H_2O)_2(VW_9O_{34})_2]\cdot 35H_2O$, a turnover frequency of $>$ 1000 s^{-1} was found by Lv *et al.* under conditions noted within references. [100, 101] The other three POMs do not exhibit any catalytic activity and are used as references. Co_3O_4 films were deposited on SiO_2 substrates by DC reactive magnetron sputtering (AJA International) from a 2" Co target with 99.95% purity at a working power of 40 W. A total pressure of 5 mTorr was used with a ratio of 20:2 sccm Ar:O_2 at a growth temperature of 600°C. Film thickness of ∼200 nm was obtained based on a deposition rate of 0.342 $\AA$ s^{-1} calculated from a quartz crystal monitor. After deposition, the Co_3O_4 film was post-annealed for 6 hours at 700°C in 1 atm O_2. Structural analysis was determined using XRD from a Siemens D500 Diffractometer with Cu Kα radiation and Raman spectroscopy. The Raman spectrum measured between 350 and 750 cm^{-1} was obtained from a Macro-Raman system with a 488 nm Ar ion laser and triple spectrometer using a 0.6 m dispersion stage with a resolution of ∼4 cm^{-1}. XRD patterns and Raman spectrum (Fig. 4.4) confirm polycrystalline Co_3O_4 thin films. The position and relative intensity of the three Raman active modes, peak centered at 692, 520, and 483 cm^{-1}, and the diffraction peaks at 36°, 42°, and 62° are

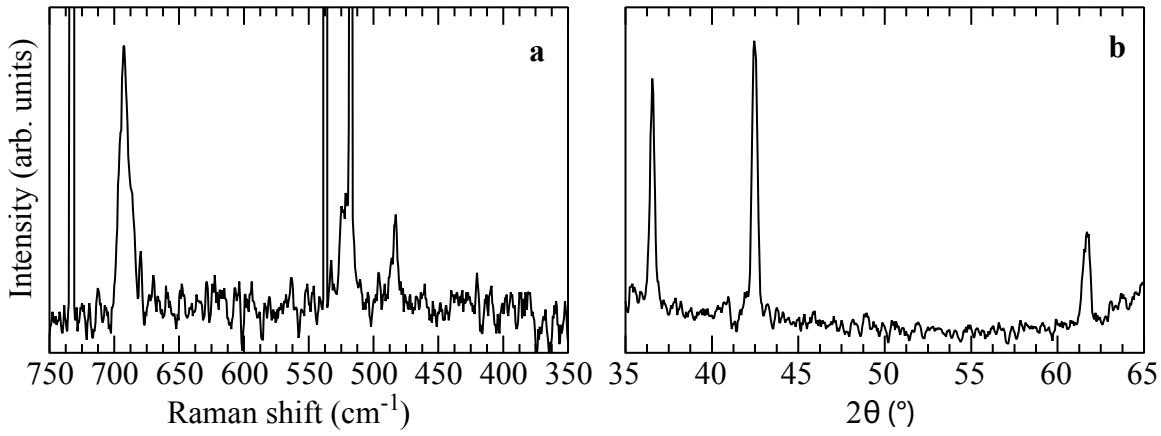

Figure 4.4: (a) Raman spectrum (b) XRD patterns of Co_3O_4 thin films.

typically associated with spinel Co_3O_4. [63, 123]

4.4 Results

4.4.1 Experimental Co L-edge XAS

Experimental Co L-edge XAS spectra for 5 POM analogues (representations in Fig. 4.2) are shown in Fig. 4.5. The analogues vary according to the number and position of Co sites within the POM structure (1 or 4 cobalt(s)), the Co valence state (2+ or 3+), coordinating geometry (O_h or T_d), and the identity of the heteroatom (silicon (Si), phosphorus (P), or vanadium (V)).

All spectra are based on TEY detection except for T_d Co^{3+} which is from TFY detection. Due to the highly oxidizing T_d Co^{3+} POM oxidizing the surface, TEY was not representative of the bulk structure and necessitated collection via TFY. Comparison of the TEY and TFY spectra for the T_d Co^{3+} POM are provided in Fig. 4.6a. The structure and peak position in the TEY suggest reduction of the surface Co centers to Co^{2+} .

The L_3 multiplet structure depends distinctly on the coordination of the Co center. For example, the TEY spectrum of O_h Co^{2+} has a low energy shoulder at 776.4 eV not present in the T_d Co^{2+} case. However, from the similarity of the L_3 structures observed for O_h Co^{2+}, O_h $Co_4^{2+}P_2$ and O_h $Co_4^{2+}V_2$, L-edge XAS does not appear to be sensitive enough to detect notable differences in the electronic structure resulting from the heteroatom (P or V) or to the number of Co sites (1 or 4) within the POM structure. It is these parameters that differentiate the water oxidation activity and therefore no direct correlation can be made within the context of the structure-activity relationship. Rather, the Co valence state and coordination geometry define the fine structure.

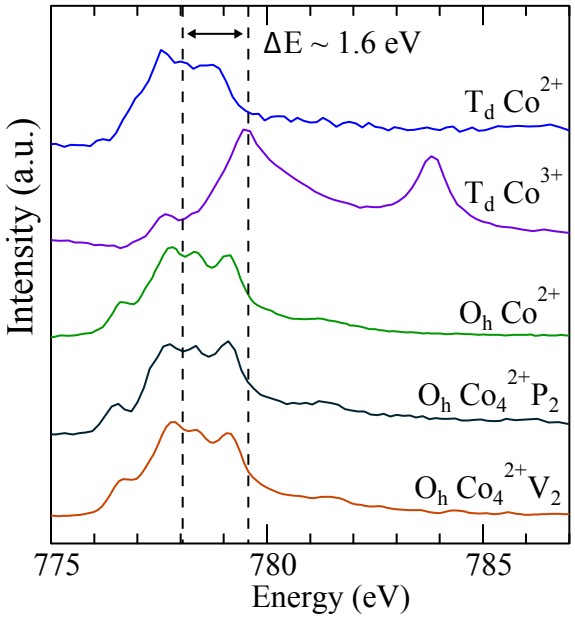

Figure 4.5: Experimental Co $2p_{3/2}$ XAS spectra of POM analogues for T_d Co^{2+}, T_d Co^{3+}, O_h Co^{2+}, O_h $Co_4{}^{2+}P_2$ and O_h $Co_4{}^{2+}V_2$.

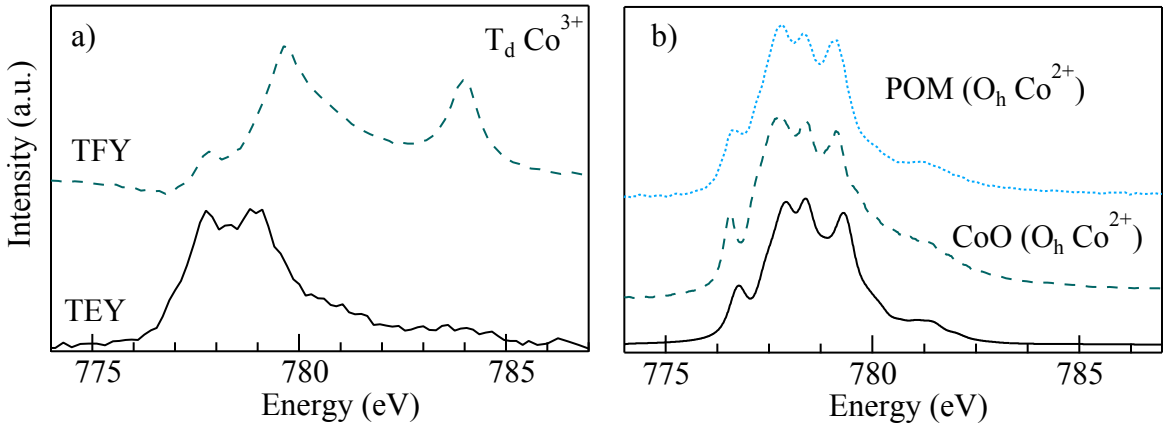

Figure 4.6: Cobalt $2p_{3/2}$ XAS spectra of a) Td Co^{3+} in TFY (dotted line) and TEY (solid line) detection method and b) O_h Co^{2+} POM (dotted line), reference CoO compound (dashed line) and LFM calculated spectrum (solid line).

The peak located at ∼784 eV in T_d Co^{3+} case consistently appears in the TFY spectra of all the systems but not in the TEY. Others have also observed this fluorescent peak at both the ALS and European Synchrotron Radiation Facility and previously assigned it as originating from charge transfer satellites or cobalt-acetate residues. [111, 124] However, the exact assignment is still unknown with some suggesting it is from barium contamination within the substrates used. The Ba $M_{4,5}$ edge is at the same energies as these observed "satellite" peaks. [125] Our recent experiments show this peak also appears prominently in systems with no cobalt, ruling out a cobalt-related assignment.

Additionally, the Co $2p_{3/2}$ XAS spectrum of a more commonly used reference compound, bulk CoO, is included in Fig. 4.6b. It is compared directly with the experimental and simulated Co $2p_{3/2}$ XAS spectrum of the O_h Co^{2+} POM to confirm the structural representations of the CoPOMs as well as the experimental and theoretical techniques applied are correct. The CoO spectrum was obtained from the ADRESS beamline at Swiss Light Source. Further details can be found at van Schooneveld *et. al.*. [110] The spectrum was simulated using the following electronic structure parameters: final state 10Dq = 0.8 eV (Ds = 0.04 eV); SIR (F_{dd}, F_{pd}, G_{pd}) = 0.9%; valence spin orbit coupling reduction (VSOCR) = 0.7%.

4.4.2 Comparison with Simulated Co L-edge XAS

Fig. 4.7 shows LFM simulated spectra of Co^{2+} and Co^{3+} in both O_h and T_d environments compared with experimental L_3 XAS spectra of a Co_3O_4 thin film (a), O_h Co^{2+} POM (b), T_d Co^{2+} POM (c), and T_d Co^{3+} POM (d). The parameters varied, namely the crystal field parameters, 10Dq and Ds, the SIR, and the VSOCR are summarized in Table 4.1.

While the O_h Co^{2+} POM and the T_d Co^{2+} POM agree well with their simulated spectrum, visible deviations exist in the T_d Co^{3+} POM and thin film Co_3O_4. In particular, for the T_d Co^{3+} POM the shoulder at 778 eV is more pronounced in the experiment. Potentially, this can be attributed to the reduction of surface Co atoms that dominate the TEY spectrum, and it appears in the bulk TFY spectrum. The shoulder is at the same energy as the sharp peak in the multiplet structure of the reduced TEY spectrum shown in Fig. 4.6a. While the TEY spectra are clearly indicative of a reduced Co center, they are not equivalent to the T_d Co^{2+} POM. Therefore, a simulated addition of two Co T_d centers with different oxidation states cannot be used to provide a better agreement and thereby quantify the extent of Co metal center reduction.

The simulated spectrum for the Co_3O_4 is created by a stoichiometric (1:2) or nonstoichiometric (1:0.8) combination of high-spin (10Dq = 0.75 eV) T_d Co^{2+} and low-spin (10Dq =1.8 eV) O_h Co^{3+} spectra, assuming the radial matrix elements are equivalent and normalizing to the integrated intensity of allowed transitions related to the number of 3d holes in each system based on sum rules. [105] The possible origins of the deviation of the thin film from simulation are discussed in the next section.

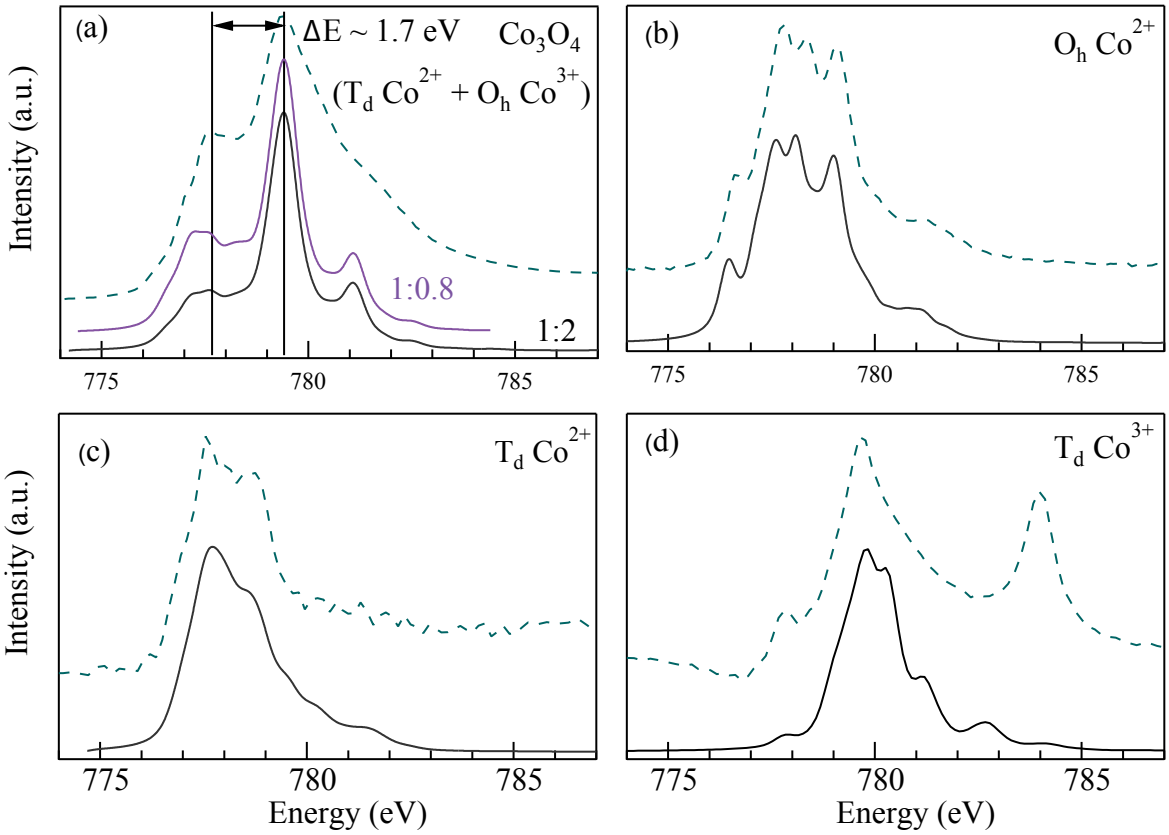

Figure 4.7: Experimental (dashed line) and LFM calculated (solid line) Co $2p_{3/2}$ XAS spectra of (a) Co_3O_4 thin film with LFM calculations based on a stoichiometric (1:2) and a nonstoichiometric (1:0.8) ratio of Co^{2+} and Co^{3+} (b) O_h Co^{2+} POM (c) T_d Co^{2+} POM and (d) T_d Co^{3+} POM.

Absorber	Final State 10Dq (eV)	SIR[a] (%) (F_{dd}, F_{pd}, G_{pd})	VSOCR[b] (%)
T_d Co^{2+} (POM)	-0.7 ± 0.1	0.9 ± 0.05	1.0
T_d Co^{3+} (POM)	-0.8	0.8	0.0
O_h Co^{2+} (POM)	0.8 ± 0.1 (4Ds = 0.16)	0.9 ± 0.05	0.7
T_d Co^{2+} (Co_3O_4)	-0.75	0.9	1.0
O_h Co^{3+} (Co_3O_4)	1.8	0.7	1.0

Table 4.1: Electronic structure parameters used for fitting L-edge absorption spectra for select absorbers

[a]Slater integral reduction [b]Valence spin-orbit coupling reduction

4.5 Discussion

4.5.1 Homogeneity vs Heterogenity

Prior XAS studies of Co-based systems have been limited by the heterogeneous sample environment of the Co centers. That is, in a heterogeneous environment, the crystalline lattice contains various types of imperfections. For example, in heterogenous Co-based systems, a mix of substitutional and interstitial sites originating from oxygen and metal vacancies exists and sometimes the Co phase separates to form metallic Co clusters as a result of structural defects. [109, 126, 127] Often times, metal oxide thin films are intentionally doped and structurally modified in order to optimize catalytic activity. These modifications deform the lattice and contribute to the important catalytic properties of the material, possibly through reduction of the band gap or by shifting the valence band edge, but also make it difficult to define the electronic structure. [30, 128, 129] In contrast, homogenous systems like the CoPOMs have easily tunable and well-defined electronic structures. Therefore, the well-defined electronic structures of the CoPOMs are linked to a representative heterogeneous sample, a sputtered Co_3O_4 thin film which typically has structural defects due to $\sim$1% Co vacancies and an unintentional p-doping of 10^{20} cm^{-3}. This link sets the stage for investigating the more interesting heterogeneous catalytic systems with L-edge XAS.

The experimental and simulated Co L-edge XAS of a Co_3O_4 thin film, displayed in Fig. 4.7a, show a relatively good agreement but deviations are still present. The contribution of T_d Co^{2+} to the simulation, when included with a stoichiometric ratio of Co^{2+} to Co^{3+}, is smaller than suggested by experiment. Deviations in the Co_3O_4 thin film likely involve site-mixing due to the Co vacancies, since Co_3O_4 is strongly p-type. These defects introduce structural distortions, where O_h Co^{2+} and T_d Co^{3+} states also exist. [130, 131]. The greater contribution to the low energy peak at 777.7 eV could be due to mixing of O_h/T_d Co contributions for both the 2+ and 3+ valence states, since according to the XAS spectra for the homogeneous POMs, these two coordination geometries are centered at approximately the same energy for a given valence state (Fig. 4.7(b,c)). A simulation considering this mixing is given by the 1:0.8 ratio calculated spectrum in Fig. 4.7a but Co vacancies alone wouldn't account for this drastic shift in stoichiometry, suggesting that other effects should be included to describe the heterogeneity of the thin film such as the additional presence of CoO from the auto-reduction of Co_3O_4 or surface-related structural distortions as discussed in Chapter 3.

4.5.2 Valence State

The effect of the valence state on the absorption energy cannot be determined precisely using ligand field models because screening effects are difficult to include correctly. However, the valence state is determined experimentally and used as an input into the LFM calculations. As the spectral shape of L_3 is a complex multi-peaked structure, the center of gravity of the complete peak is used to study the valence state rather than the edge position. As

shown in Fig. 4.5, T_d Co^{3+} occurs ∼1.6 eV higher in energy than T_d Co^{2+}. When there are fewer d e^- (*i.e.* greater oxidation state), the effective nuclear charge Z_{eff} is greater because there is less screening by the d shell and the electrons "feel" a greater amount of positive charge. [132] This is consistent with previous reports on energy shift per valence state change found for 3d transition metal oxides with one study reporting a linear slope of 1.5 eV/valency. [133–135] This energy shift arises from the greater degree of effective nuclear charge Z_{eff} acting on the core electron when there are fewer valence electrons to screen the positive charge. To provide another example, the experimental Co 2p XAS of a Co_3O_4 thin film is shown in Fig. 4.7(a). As mentioned previously, Co_3O_4 has a spinel structure consisting of Co^{2+} and Co^{3+} in T_d and O_h sites, respectively. The pronounced L_3 doublet peak structure is assigned to these oxidation states with Co^{2+} at 777.7 eV and Co^{3+} at 779.4 eV to give a 1.7 eV energy shift with valence state.

4.5.3 Ligand Field and Structural Distortions

The values of the crystal field applied to the LFM spectra in Fig. 4.7 are listed in Table 4.1. A negative 10Dq value for the T_d structures indicates a d-orbital splitting with a lower energy e and higher energy t_2 set, that is reversed from the O_h case (where t_{2g} is lower and e_g is higher). The value of 10Dq increases for O_h structures relative to T_d due to the larger number of ligand atoms (6 versus 4), though the increase is mitigated by the longer metal-oxygen distances in an O_h geometry that also reduces the 10Dq. An increase in metal oxidation state also indicates a stronger bond with the oxygen ligands, and therefore increases 10Dq as reflected in the larger value of 10Dq = 1.8 eV for O_h Co^{3+} in Co_3O_4 vs 10Dq = 0.8 eV O_h Co^{2+} POM. These markedly different ligand field splitting energies result in a low spin

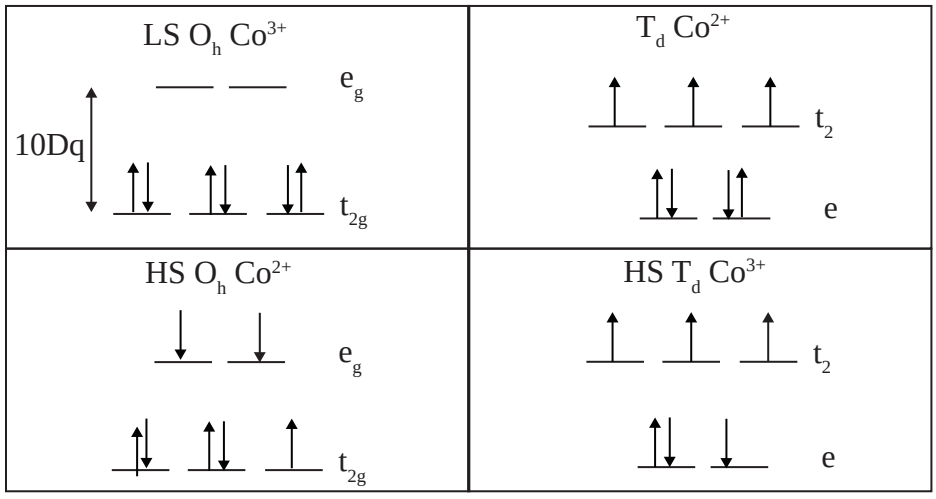

Figure 4.8: Crystal field diagrams for T_d and O_h Co(II) and Co(III). HS and LS refer to high spin and low spin, respectively.

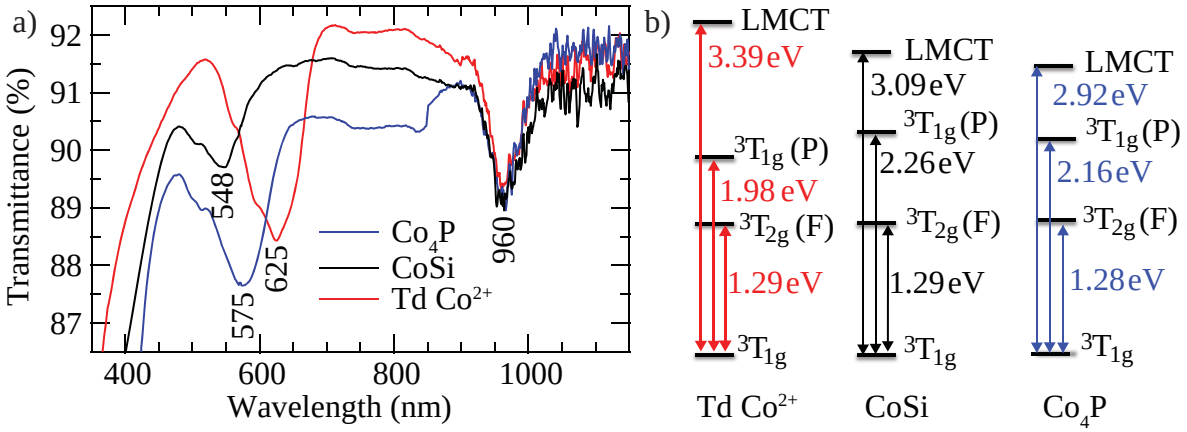

Figure 4.9: UV-vis-NIR electronic absorption spectra of T_d Co^{2+} (red dotted), O_h $Co_4{}^{2+}P_2$ (blue dashed) and O_h $Co^{2+}Si$ (black solid)

electron configuration for Co^{3+} in Co_3O_4 and a high-spin configuration for the O_h Co^{2+} POM. The electron filling configurations are shown in Fig. 4.8 for the various geometries, valence states and 10Dq values.

In XAS experiments, it is the final state 10Dq value that dictates spectral shape. The magnitude of the X-ray 10Dq is routinely found to be less than the UV-vis 10Dq, which measures the ground state 10Dq. [133] The difference is the presence of a core hole in the final state for the X-ray absorption process, which is understood to increase localization of metal d orbitals and thus decrease the magnitude of the energy splitting. For example, in the O_h Co^{2+} case, the optical 10Dq value is 1.4 eV while the X-ray 10Dq was determined to be 0.8 eV. Optical 10Dq values were calculated using the Tanabe-Sugano diagram [136] According to the experimental UV-vis-NIR spectra for three select POM analogues shown in the Fig. 4.9a, the possible transitions and their corresponding energies are listed in Fig. 4.9b. For d^7 case, the ground state term is $^3T_{1g}$. The first spin allowed transition is to the $^3T_{2g}$ (F) and another spin allowed transition is $^3T_{1g}$ (P). Utilizing a Tanabe-Sugano diagram specifically for d^7 O_h, a series of spin allowed and some forbidden transitions are given in Fig. 4.10 with E/B vs Δ/B energies. The vertical line at Δ/B = 22 indicates the transition from high spin to low spin. To determine the optical 10Dq energy from the UV-vis-NIR spectra, the procedure is to first determine the lowest transition energy (*i.e.* 960 nm) and the ratio of the energies between the second versus the first transitions. Second, locate where that ratio matches the values on the Tanabe-Sugano diagram (indicated by the arrows in Fig. 4.10) to get the predicted values of E/B from the y-intercept and Δ/B from the x-intercept. Using the predicted values, calculate B and, then, calculate Δ from that B. Δ is the optical 10Dq. For the tetrahedral case, d^3 Tanabe-Sugano diagram is used based on the d^{10-n} rule and $10Dq = \Delta \times \frac{4}{9}$. [137] This method gives an optical 10Dq of 0.56, 1.42, and 1.40 eV for Co^{2+} T_d, CoSi, and Co_4P, respectively. The X-ray 10Dq for Co^{2+} T_d of -0.7 eV is

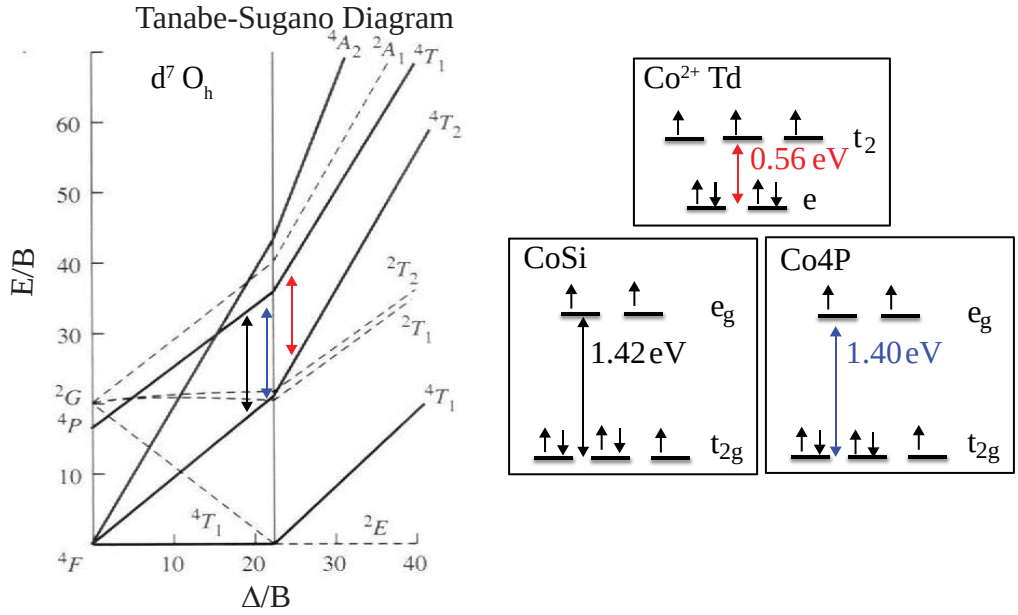

Figure 4.10: d^7 O_h Tanabe-Sugano Diagram and calculated optical 10Dq values for three POMs.

not less than the optical 10Dq value as predicted. However, several assumptions were made for determining the optical 10Dq for the tetrahedral structure which may be inaccurate.

The inclusion of a small axial distortion, Ds = 0.04 eV, was necessary to reproduce the shoulder (781.3 eV) on the high energy side of L_3 for the O_h Co^{2+} ion. This distortion reduces the symmetry from O_h to D_{4h} and is consistent with X-ray crystallography studies of POM structure. [138, 139] The Ds parameter corresponds to an elongation of the z-axis, yielding an energy difference between the d_{z^2} and $d_{x^2-y^2}$ orbital of 4Ds, or 0.16 eV. In agreement with previous X-ray structural studies, it was not necessary to introduce a distortion for the T_d Co^{2+} POM. [140, 141]

Ligand field 10Dq values are further justified by showing changes in calculated spectra as a function of this parameter (Fig. 4.11(a), (b)) and compared with experimental spectra for O_h Co^{2+} POM and T_d Co^{2+} POM. 10Dq is varied from 0.5 - 1.4 eV in 0.3 eV steps while the remaining parameter values are kept constant. In the O_h Co^{2+} case, large changes in peak shape arise due to the transition from the high spin to low spin configuration. From Fig. 4.11(a), one can see that a 10Dq value around 0.8 eV is consistent with the experimental spectrum of O_h Co^{2+}. Small step sizes of 0.1 eV around this value produce appreciable changes in the spectrum (Fig. 4.11(c)), such that 10Dq = 0.8 eV to within ±0.1 eV can be reported. Similarly, 10Dq = -0.7 eV to within ±0.1 eV agrees with the experimental T_d Co^{2+} (Fig. 4.11(d)).

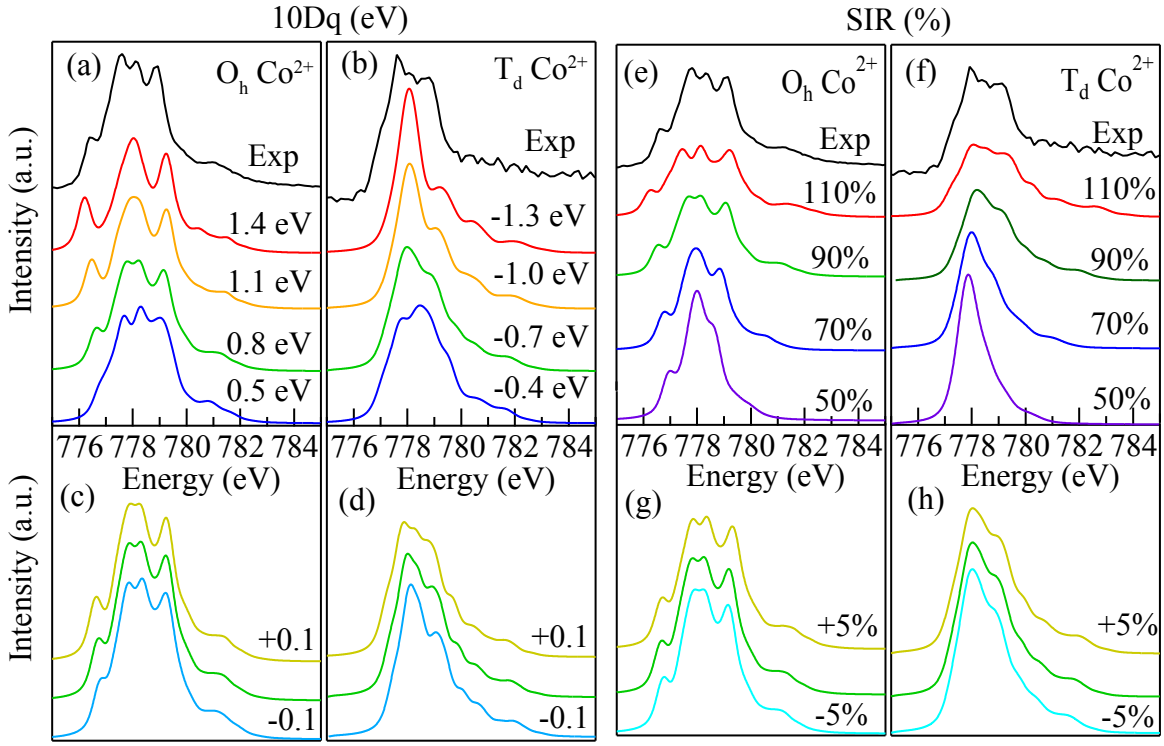

Figure 4.11: (a) O_h and (b) T_d Co^{2+} spectra calculated at a series of crystal field splitting parameters (10Dq). (c) and (d) show spectra for small step sizes with 10Dq values ±0.1 eV from 0.8 and -0.7 eV, respectively. (e) O_h and (f) T_d Co^{2+} spectra calculated at a series of SIR. (g) and (h) show specta for small step sizes with SIR values ±5% from 90%. All other electronic structure parameters are held constant.

4.5.4 Electron-Electron Interactions: Slater Integral and Valence Spin-Orbit Reduction

As shown in Table 4.1, for all the compounds studied a reduction of the Slater integrals is required, with 90% of the atomic value for Co^{2+} absorbers and 70-80% for Co^{3+} absorbers. Reducing the Slater parameters can be understood as simulating an increased d-electron delocalization, or covalency, that occurs in going from a free ion to a complex. This is commonly described as the nephelauxetic effect in transition metal complexes. [142, 143] The degree of covalency, and thus SIR, becomes more significant as the oxidation state of the metal center increases. As above with 10Dq, further justification for SIR values is provided by varying them from 50% - 110% in 20% steps (Fig. 4.11) for the O_h Co^{2+} and T_d Co^{2+} cases. In general, as the reduction increases and the separation between atomic multiplet states becomes smaller, the L_3 peak splitting decreases and the edge becomes centered around a single distinct peak. Judging by the spectra in Fig. 4.11(e, f), in both

cases a SIR value of around 90% is a reasonable choice for the 2+ valence state. Slater integrals reduced by ±5% around 90% provide an error bar for visual inspection (Fig. 4.11 (g,h)).

The last parameter to be discussed is the VSOCR. Reduction of the 3d spin-orbit coupling from its atomic value is due primarily to ligand field effects that change the d-orbital occupation, but can also come from delocalization effects. In cases such as T_d Co^{2+} and low-spin O_h Co^{3+}, where the ground state electronic configuration ($e^4t_2^3$ and t_{2g}^6, respectively) has A symmetry, there is no difference in the spin-orbit coupling from the atomic state and this parameter can be left the same. However, the high-spin O_h Co^{2+} case (Fig. 4.7(b)) requires a reduction to 70% of the atomic value, due to a half-filled t_{2g} orbital that does change the d-orbital occupation. This is consistent with previous values used to calculate spectra for CoO nanocrystals. [110] In contrast, a full quenching (0%) of the atomic value is necessary for T_d Co^{3+} due to a change in the orbital occupation of the e orbitals. [137, 144]

4.6 Conclusion

The electronic structures of Co centers in a set of nanoscale CoPOMs and a Co_3O_4 thin film using L-edge XAS were characterized. Spectra were analyzed by LFM theory to obtain the valence state, the strength of the ligand field through 10Dq, the effect of structural distortions through Ds, and the degree of covalency through reduction of the Slater integrals. The valence state and SIR were determined to a high degree of accuracy, within ±0.1 eV or ±5%. Together, these parameters depict the electronic structure of the unoccupied *d*-electron states of Co^{2+} and Co^{3+} in O_h and T_d environments within well defined model systems. The work demonstrates the straightforward use of LFM theory and provides a benchmark for the many Co containing photo-catalysts currently being investigated. While *ab initio* calculations of the L-edge would be a more precise determination of the electron structure, they are currently beyond the scope of current computational power. However, the multiplet structure of the L_3 edge provides a fingerprint that is enough to differentiate key parameters of the ground state electronic structure of Co-based catalysts. The results suggest that L-edge XAS is not sensitive enough to detect differences in electronic structure due to multiple Co atoms in similar local environments, or to heteroatoms in the Co atom's vicinity. It is these properties that, qualitatively looking, has the largest impact on catalytic activity. Therefore, the work also shows that even more sensitive X-ray techniques, such as resonant inelastic x-ray scattering (RIXS), along with additional probes of the oxygen atom, should be employed to investigate notable differences in the ground state electronic structure affecting reactivity. To support this statement, the oxygen K-edge RIXS spectra for two POM structures are noted in Appendix B showing that differences in the valence band can be observed.

Chapter 5

Surface Hole Mobilities and Dynamics Determined with Transient Grating Spectroscopy

Portions of the content and figures of this chapter are reprinted or adapted with permission from H.Q. Doan, K.L. Pollock, and T. Cuk, Chem. Phys. Lett. 649, 1-7 (2016).

5.1 Introduction

In a full PEC cell, the photogenerated area is often spatially separated from the actual water splitting reaction. [7, 8] Therefore, in addition to surface reactivity, charge transport is equally important when studying STH efficiency. [36, 145, 146] Previously, the focus was on the water oxidation catalysis and characterizing the transient and steady-state electronic structure differences affecting reactivity. Now the attention shifts to the transport properties of the charges within a photoanode, specifically using GaN as a model system. Upon illumination with above band gap energy, the upward band bending at the photoanode surface propels photogenerated electrons away from and holes towards the catalytic surface. In the case for n-GaN, when the photoholes reach the interface, they can participate in the following activities:

1. oxidation of reductants in solution (*e.g.* water oxidation)
2. photo-corrosion of GaN
3. surface recombination
4. bulk carrier recombination

Only the first process is desirable but the extent each process occurs is affected by the surface structure and is closely linked to the charge transport properties of the semiconductor.

How fast the charges reach and laterally move across the interface is characterized by the material's mobility. The mobility of a material describes the drift velocity of a carrier experiencing the influence of an electric field. The main contributions that decrease mobility are:

- lattice scattering (*ie.* phonon-assisted)
- impurity or defect scattering
- carrier-carrier scattering events.

At room temperature, in pure or low carrier concentration materials, lattice scattering dominates. For highly doped materials, the mobility is mainly reduced by carrier-carrier scattering or defect scattering. At the surface, where the termination of the periodicity of the crystal lattice forms dangling bonds, defects and impurities are prominent. Any defects or impurities within or at the surface of the semiconductor promote recombination. Surface passivation techniques, either through a protective overlayer or chemical treatment, ties up dangling bonds, reducing the number of defects and, thereby, increasing mobility by limiting scattering events. This description is true at the solid state/air interface. However, at the solid state/electrolyte interface a different picture guides interfacial carrier mobility. When in contact with an electrolyte solution, a substantial density of localized mid-gap surface states can form at the semiconductor surface either through adsorption of water molecules or via dark charge transfer during equilibration of the electrochemical and redox potential. These surface states serve as potential catalytic sites to mediate catalysis. Mediation can increase catalytic activity through the new reaction intermediates and provide an alternative reaction pathway for hole transfer or directly affect the semiconductor because those new surface states increase carrier mobility along the surface. With increased mobility, the probability of the photohole interacting with a reactant molecule increases. This lateral diffusion of carriers at an aqueous interface has yet to be quantified and connected experimentally with surface reactivity. [147–156]

Based on the results of this work, it is proposed that for n-GaN mediation by surface states directly influences the material properties. A look at the carrier diffusivity variations at different interfaces are discussed next. The first section discusses the transient grating technique used to characterize the transport of carriers. The second section gives the unique and interesting properties of GaN and why it was chosen as the system to study. Lastly the results and conclusion of the experimental work on GaN are provided. Both steady-state photoelectrochemical and transient spectroscopic measurements were performed in order to show quantitative evidence for the first time for the interdependence of interfacial hole mobility and charge reactivity. Additionally, a comparison of transient absorption (TA) and transient grating (TG) kinetics is made to show the photo-excited carriers do not simply decay within 200 ps but survive in "invisible" trapped states, exhibiting dispersive rather than absorptive behavior, for up to a nanosecond. Further, voltage-dependent studies of the TG kinetics highlight a unique dependence that could not be observed in traditional

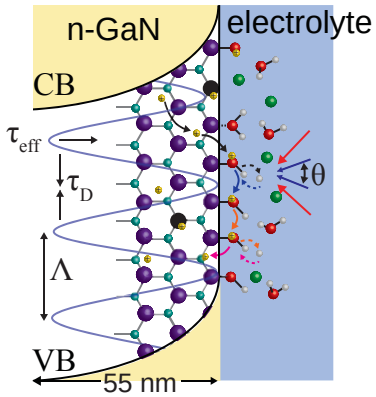

Figure 5.1: Cartoon depicting observation of hole transport using transient grating technique at GaN/electrolyte interface.

TA measurements that reinforces the dispersive diffusion picture from hole hopping between different localized states as depicted in Fig. 5.1.

5.2 Transient Grating Spectroscopy

The transport of photogenerated minority charge carriers is a key material property defining the efficiency for photovoltaic power conversion devices. The easiest and most common technique to measure mobility is via the Hall effect but this method has its limitations. As an electrical measurement, good contact is necessary which is often difficult to obtain unless a highly doped sample is used. With highly doped samples, the majority charge carriers dominate the measurements making the Hall effect method impractical. In this experiment, it was necessary to examine the transport of the minority carriers, *i.e.* holes, in both an undoped and n-doped GaN sample in order to compare surface reactivity with mobility. TGS serves as a direct method for probing the diffusivity of minority charge carriers in both these samples. TGS is a non-linear optical, four-wave mixing technique that uses short light pulses to control the photo-excitation process in time and space. TGS is a powerful tool that has been used to study a wide range of phenomena, from charge transport [149, 157] to phase transitions [158, 159] to molecular rotational dynamics. [160, 161] This section lays the mathematical and experimental ground work for studying interfacial charge transport using the TGS method. A more detailed description of TGS can be found in Ref. [162, 163].

TGS consists of two distinct processes. The initial step in TGS is creation of a dynamic optical grating through the spatial superposition of two mutally coherent waves. Excitation from wave vectors, k_1 and k_2, creates an interference pattern within the sample with grating vector

$$q = \pm(k_1 + k2) \tag{5.1}$$

The period of the induced grating is defined by

$$\Lambda = \frac{\lambda_{pump}}{2sin(\theta)} = \frac{2\pi}{q} \tag{5.2}$$

where λ is the wavelength of excitation and θ is the angle between the two interfering excitation beams k_1 and k_2. By tuning θ, the grating spacing (Λ) is changed.

If absorption of a photon with frequency ω is in resonance with a transition in the material, *e.g.* bandgap transition, a grating of coherent excited states forms. The response by the material is a periodic spatial modulation of the optical properties of the material, *e.g.* the refractive index (n) or absorption coefficient (k) or both, which can generally be expressed as the complex dielectric constant ϵ_R.

$$\epsilon_R = \tilde{n}^2 \text{ where } \tilde{n} = n + ik \tag{5.3}$$

Therefore, the detected diffracted intensity η associated with TGS is

$$\eta \cong \Delta\epsilon_R \cong \tilde{n}^2 \cong \alpha(\Delta n)^2 + \beta(\Delta k)^2 \tag{5.4}$$

If the probe frequency is near a transition frequency, the change in the complex dielectric constant $\Delta\epsilon_R$ occurs mainly to the absorptive or imaginary part of the ϵ_R and it is referred to as an amplitude grating. On the other hand it is termed a phase grating if the modulation is mostly in n or the real part of ϵ_R. This dominates when the probe frequency is far from a transition frequency as is the case for the TGS experiments performed on GaN discussed below.

The second step in TGS monitors the optical grating through diffraction, or forced light scattering, of a time-delay controlled third electric field. The dynamic optical grating created by the initial excitation process is modified by local relaxation processes as well as diffusion phenomena. The sinusoidal modulation, shown in Fig. 5.2a), can decay via two distinct mechanisms. One mechanism is recombination of charge carriers and relaxation back to the ground state, represented in Fig. 5.2b). This decreases the amplitude by shifting the excited region downward. The other mechanism is the spatial equilibration of $\Delta\epsilon_R$ through diffusion as represented in Fig. 5.2c). Diffusion does not change the average $\Delta\epsilon_R$ but, rather, decreases the intensity by smearing the spatial profile. Recombination is independent of Λ but diffusive transport has a decay time with a quadratic dependence on Λ. TG takes advantage of this difference to isolate the transport processes and deduce a diffusion coefficient D of a material.

5.2.1 Diffusivity and Surface Recombination Velocity Determination

Two limiting cases exist for the induced grating. If Λ is smaller than the optical length or sample thickness d ($d \gg \Lambda$), a thick grating forms. As light can interact multiple times with the scattering plane when passing through a thick grating, only specific probe angles

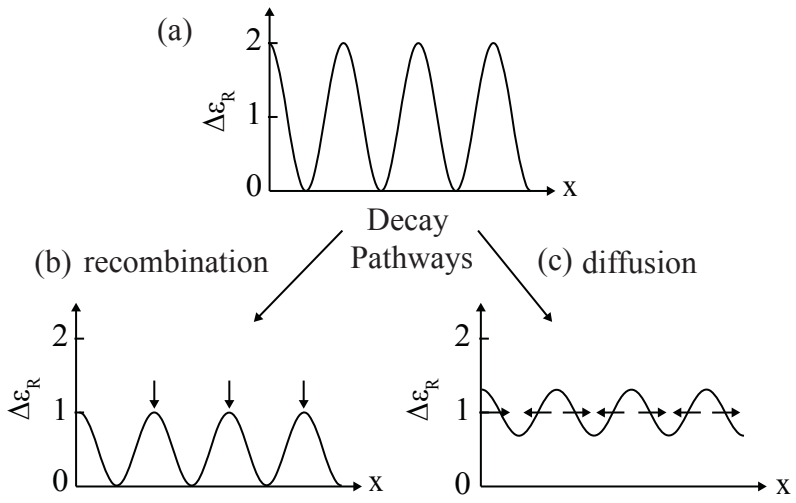

Figure 5.2: a) Cartoon of the sinusoidally varying pattern of intensity of the change of the complex dielectric constant $\Delta\epsilon_R$ after photo-excitation along the x plane. This plane is parallel with the sample surface. The two decay pathways for this excitation pattern is b) recombination and c) diffusion.

interfere constructively and yield intense diffracted beams. The derivation for the diffraction efficiency η for a thick grating is complicated and will not be discussed further. More relevant is the thin grating case. If $d \ll \Lambda$, the grating is characterized as thin and light interacts only once with the scattering plane. A sinusoidal transmission grating can be assumed and the diffraction efficiency η of that grating can be calculated by solving the second-order continuity equation for the relaxation of charge carriers, [151]

$$\frac{\partial N(x,z,t)}{\partial t} = \nabla[D(N)\nabla N(x,z,t)] - \frac{N(x,z,t)}{\tau_R(N)} \tag{5.5}$$

where $N(x,z,t)$ is the electron-hole density, $D(N)$ is the diffusion coefficient dependent on the electron-hole density, and $\tau_R(N)$ is the lifetime of the photogenerated carriers dependent on photogenerated carrier density. The biomolecular and Auger recombination terms can be relevant but are not taken into account in this case because care was taken to stay in the low excitation regime. To solve this equation, certain boundary conditions are needed. The boundary conditions are

$$\left.\frac{\partial N(x,z,t)}{\partial z}\right|_{z=0} = \frac{S}{D(N)} N(x,0,t) \tag{5.6}$$

and

$$N(x,\infty,t) = 0 \tag{5.7}$$

where is the surface recombination velocity, describing the recombination at a surface that is limited by the rate at which carriers arrive at that surface. The initial condition, given by

creating a thin grating of carriers, is

$$N(x,z,0) = g(x)l(z) = N_0[1 + cos(\frac{2\pi x}{\Lambda})]e^{-\alpha z} \tag{5.8}$$

where z is the direction normal to the grating and g(x)l(z) is the spatial generation function. N_0 is the initial excess carrier density at the surface, Λ is the grating period and α is the absorption coefficient of the excitation frequency.

Assuming D and τ_R are constant by suppressing the dependence on N, which experimentally is done by maintaining a lower carrier density, the solution to Eq. 5.5 is

$$N(x,z,t) = \left\{1 + \cos\left(\frac{2\pi x}{\Lambda}\right)\exp\left(-\frac{4\pi^2 D}{\Lambda^2}t\right)\right\}\Phi(z,t), \tag{5.9}$$

where $\Phi(z,t)$ is

$$\Phi(z,t) = \frac{N_0}{2}\exp\left(-\frac{t}{\tau_R}\right)\exp\left(-\frac{z^2}{4Dt}\right)\left\{W\left(\alpha(Dt)^{\frac{1}{2}} - \frac{z}{2(Dt)^{\frac{1}{2}}}\right) + W\left(\alpha(Dt)^{\frac{1}{2}} + \frac{z}{2(Dt)^{\frac{1}{2}}}\right) - \frac{2\frac{S}{D}}{\frac{S}{D}-\alpha}\left[W\left(\alpha(Dt)^{\frac{1}{2}} + \frac{z}{2(Dt)^{\frac{1}{2}}}\right) - W\left(\frac{S}{D}(Dt)^{\frac{1}{2}} + \frac{z}{2(Dt)^{\frac{1}{2}}}\right)\right]\right\} \tag{5.10}$$

with W(x) = $\exp(x^2)$erfc(x).

The first-order diffraction intensity $\eta(t) \propto \int \Delta\tilde{n}(t)^2$ and using $\Delta\tilde{n}(t) \sim$ N(x, z, t), the thin sinusoidal transmission grating is described by

$$\eta(t) = J_1^2\left\{\frac{\pi}{\lambda}\frac{e^2}{2nm^*_{eh}w^2\epsilon_0}\int_0^\infty\left[N(\Lambda,z,t) - N(\frac{\Lambda}{2},z,t)\right]dz\right\} \tag{5.11}$$

where J_1 is the first-order Bessel function. Using Eq. 5.9 to solve Eq. 5.11 gives the diffraction efficiency,

$$\eta(t) \propto \frac{\exp^{-\frac{4\pi^2 Dt}{\Lambda^2} - \frac{t}{\tau_R}}}{\alpha}\left[1 + \frac{1}{\frac{S}{D}-\alpha}\left(\frac{S}{D}\exp(\alpha^2 Dt)\text{erfc}(\alpha\sqrt{Dt}) - \frac{S}{D} - \alpha\,\exp((\frac{S}{D})^2 Dt)\text{erfc}(\frac{S}{D}\sqrt{Dt}) + \alpha\right)\right] \tag{5.12}$$

Using eq. 5.12, the TGS kinetics can be well-modeled. In addition to the carrier diffusivity, the TGS kinetics can also quantify S. The surface recombination rate and diffusion rate are intrinsically tied together because recombination is limited by the speed with which minority carriers can move towards the surface. In a well-passivated surface with no recombination, the movement of carriers towards the surface is zero, and hence S = 0. In a surface with infinitely fast recombination, the movement of carriers towards this surface is limited by the

maximum velocity they can attain. Therefore, S (cm/s) is an inherent measure of the defect density which affects the lifetime and efficiency of charge carriers.

In order to fit the TGS kinetics to eq. 5.12 which is described by three fitting parameters (S, τ_R and D), one must be solved for. D can be determined using a simpler model characterizing η(t) decay. As mentioned previously and derived in Eq. 5.9, the diffusive transport has a quadratic dependence on Λ and this unique property is utilized to isolate D from the other decay processes. The decay of the diffracted intensity is described simply as

$$\eta(t) \propto \exp^{-2t\tau^{-1}}. \tag{5.13}$$

A fit of the TG kinetics to this monoexponential decay yields τ^{-1} where τ^{-1} is

$$\tau^{-1} = \frac{1}{\tau_D} + \frac{1}{\tau_{eff}} = D\frac{4\pi^2}{\Lambda^2} + \frac{1}{\tau_{eff}} \tag{5.14}$$

When Λ is small, *i.e.* a narrow grating, diffusion is easier and faster. When Λ is large, *i.e.* a broad grating, recombination dominates. Therefore, by plotting τ^{-1} as a function of q^2 where $q = \frac{2\pi}{\Lambda}$, a linear dependence forms. Using a best-fit line, the slope and intercept are the diffusion coefficient D and inverse effective recombination time τ_{eff}^{-1}, respectively. The effective recombination time τ_{eff} accounts for all decay processes except for diffusion. This is different from the τ_R in Eq. 5.12, which only describes the linear recombination processes.

5.2.2 Experimental Setup and Analysis

Fig. 5.3 is an illustration of the TG setup employed. The setup before the diffractive optic (DO) mirrors the conventional two-pulse pump probe experiment described previously. A 266 nm pump and 800 nm probe beam are focused onto a customized DO element (Holoeye Corp., San Diego, CA) which splits the transmitted beam into multiple diffraction order beams. Only the ± 1 orders beams are of interest and all other orders are blocked (not shown). In contrast to a beamsplitter, the DO offers the advantage of passively phase-locking the pulse pairs, automatically aligning the wave vectors for Bragg angle phase matching, and preserving the spatial and temporal resolution of the beams. The DO element contains an array of customized permanent gratings that controls the angle of diffraction. Therefore, the angle θ between the ± 1 order pump beams and, hence, Λ is easily tuned. The DO was customized to give Λ = 2.3 μm, 2.9 μm, 3.7 μm, 4.6 μm, 5.6 μm, 7 μm, 9 μm, and 12 μm.

The two excitation pulses and two probe pulses pass through a 200 mm collimating and 200 mm focusing lens in a boxcar geometry to focus onto the sample. The two pump beams intersect at an angle θ on the sample, forming a dynamic grating pattern from which the probe diffracts in the same direction as the transmitted beam of opposite order called the reference or local oscillator (LO). A pair of variably tilted microscope coverslips, placed in the probe beam paths, provide fine control over the $t = 0$ position and relative phase between diffracted and LO pulses. One of the coverslips is placed on a motorized rotation platform (RP01, Thorlabs, Inc., Newton, N.J.) for automated rotation. The boxcar geometry ensures

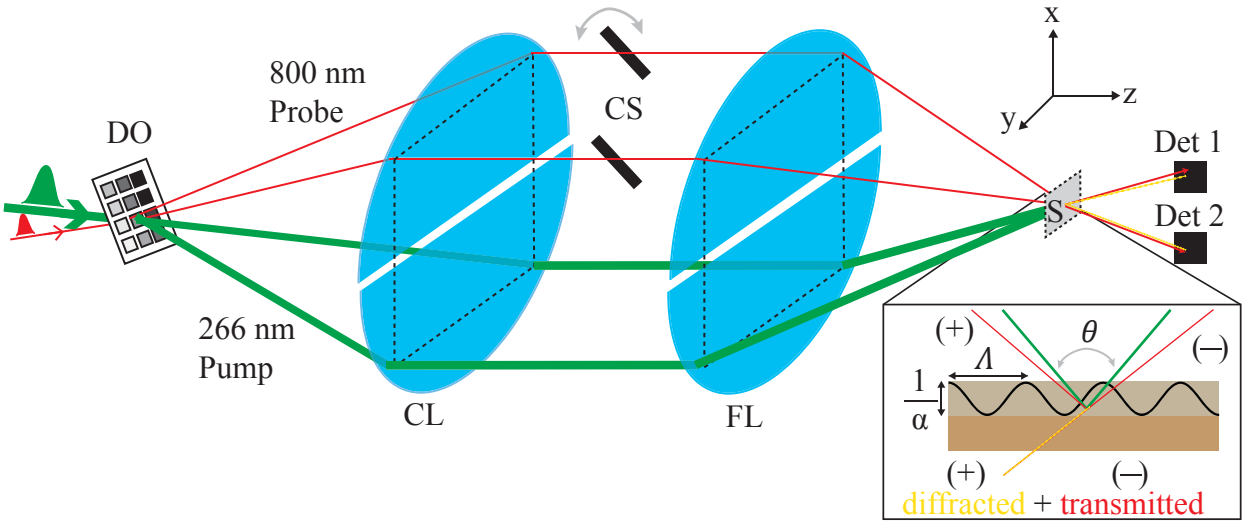

Figure 5.3: Heterodyne transient grating spectroscopy experimental set-up. DO is diffractive optic. CL and FL are collimating and focusing lens, respectively. CS is coverslip and S is sample.

proper phase matching for any combination of input frequencies as well as a collinear overlap between the diffracted and LO pulses on the detector. The detection of both transmitted and diffracted pulses is called heterodyne detection and is discussed further below.

The 200 mm collimating/focusing lens are cut in half in order to control independently the collimating/focusing properties of the probe and pump beams individually. Since large ultraviolet achromatic lenses were not available, it was necessary to cut the lenses in half to counteract both spherical and chromatic abberations that prevent spatial overlap of the focal point of the ultraviolet pump and infrared probe beams on the sample. Each of the four lens pieces are placed on mechanical stages to allow precise tuning of each lens positions and, hence, crossing position of pump and probe beams along the z axis. Two signals can be collected based on the boxcar geometry and were simultaneously collected by using two detectors connected to two lock-in amplifiers. Pumping at a unique Λ, a signal is recorded at multiple coverslip angles for each time delay point. Fig. 5.4 shows a representative plot of the signal (%) with respect to coverslip angle (radian) at a time delay point after time zero for the two detectors. A sinusoidal relationship is observed and can be fitted with

$$B + A \cdot \cos(k \cdot \text{Coverslip Angle} + \beta) \tag{5.15}$$

to obtain the amplitude (A), offset (B) and phase (β). The frequency (k) is held constant for all time delay points. The data extracted from the sinusoidal fit of both detectors at a

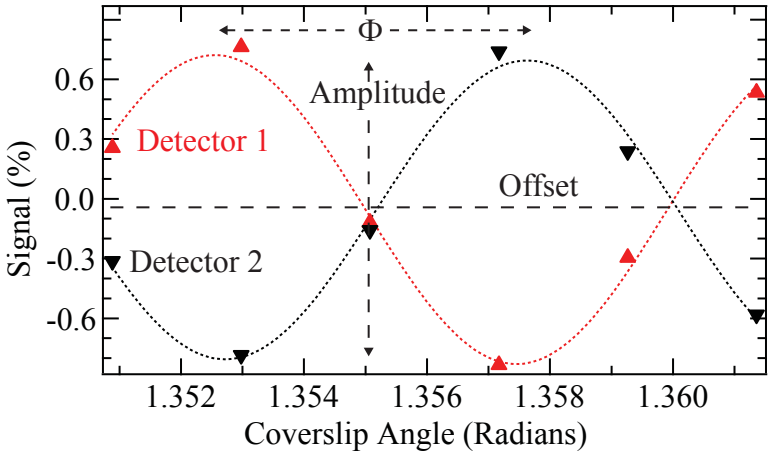

Figure 5.4: A representative plot of the data collected at one time delay position: Signal % at six coverslip angles (radians)

given time delay yield:

$$\begin{aligned} \frac{A_1 + A_2}{2} &= \frac{TG}{T}(\%) \\ \frac{B_1 + B_2}{2} &= \frac{\Delta T}{T}(\%) \\ \frac{\beta_2 - \beta_1}{2} &= \phi_{diff} \end{aligned} \tag{5.16}$$

The TG/T (%) decay kinetics can, then, be plotted after performing this analysis for each time delay point. Repeating this process at multiple grating spacings yields a series of TG/T (%) decay curves.

Finally, each TG/T (%) decay curve is fitted to a monoexponential fit based on eq. 5.13 to extract τ^{-1} the inverse decay rate at a given Λ. A τ^{-1} vs q^2 is plotted and a linear relationship observed. In addition to TG/T (%), two additional pieces of information are known from the data set. A ΔT/T (%) decay curve is obtained which is analogous to kinetics from a conventional two-pulse pump probe experiment. More unique to a heterodyne-detected TG experiment, the ϕ_{diff} is extracted. The significance of ϕ_{diff} is discussed further in the section below on optical heterodyne detection.

5.2.3 Optical Heterodyne Detection

As opposed to traditional two-pulse pump probe experiments, which are insensitive to changes in transmission or reflectivity out of phase with equilibrium, TGS has the ability to overcome this deficiency with heterodyne detection of the probe electric field. Although time intensive, optical heterodyne detection yields two benefits. First, there is a gain in detection,

i.e. the signal is amplified by 2×LO field. Secondly, the linearization of the signal to $\Delta\tilde{n}$ (rather than $\Delta\tilde{n}^2$ for homodyne detection) allows for separation of the real and imaginary components of the complex refractive index. In order to achieve heterodyne detection, a four-beam boxcar geometry is employed as shown in Fig. 5.3. Here, a fourth electric field is introduced as a LO which mixes on the detector with the weak diffracted signal field. The diffracted signal is related to the third order polarization $\mathbf{P}^{(3)}$(t) by

$$\begin{aligned} E_{diff}(t,\phi) &\propto i\mathbf{P}^{(3)}(t,\phi) \\ &\propto i\cdot\{Re[P^{(3)}(t)]cos(\phi_{diff}) + Im[P^{(3)}(t)]sin(\phi_{diff})\} \\ &\propto Re[P^{(3)}(t)]sin(\phi_{diff}) + Im[P^{(3)}(t)]cos(\phi_{diff}) \\ &\propto E_n(t)sin(\phi_{diff}) + E_k(t)cos(\phi_{diff}) \end{aligned} \tag{5.17}$$

The two components, the refractive part (E_n(t)) and absorptive part (E_k(t)), of the diffracted signal can be separated if the phase ϕ_{diff} is known.

The intensity on a square law detector in a heterodyne set-up is

$$\begin{aligned} I_{het} &= [E_{diff}(t,\phi_{diff}) + E_{LO}(t,\phi_{LO})]^2 \\ &= |E_{diff}|^2 + |E_{LO}|^2 + 2|E_{LO}(t)E_{diff}(t)|cos(\phi_{LO} - \phi_{diff}) \end{aligned} \tag{5.18}$$

where $|E_{LO}|^2$ is the constant background term which can be easily substracted with lock-in detection, $|E_{diff}(t)|^2$ is negligibly small in the limit of $|E_{LO}| \gg |E_{sig}(t)|$, and the final term is the interference (heterodyne) term. Heterodyne detection requires control of the relative phase difference between the LO and the signal $\Delta\Phi = \phi_{LO} - \phi_{diff}$ which is achieved using coverslips. [162, 164].

Phase calibration is necessary to determine ϕ_{diff} and is often performed by using a reference material with a well known photoresponse. For example, carbon disulfide (CS_2) is often used as a reference because it has a large refractive change but a minimal imaginary response when photo-excited. [162, 164] Another method, and the one employed here, determines the absolute signal phase based on the symmetry between the LO and probe beams that was first performed within the Orenstein group at University of California- Berkeley. [165] Due to the symmetry, the third and fourth electric fields are interchangeable and both behave as the LO and probe beam simultaneously. Therefore, two heterodyne signals can be detected that are identical in magnitude but the diffracted wave vectors are different by ± q. The two heterodyned signals are

$$\frac{\Delta I_1}{I_1} = \frac{\delta t}{t_0}\cos(\phi_{diff}) + \frac{TG}{T}\cos(k\theta - k\theta_0 - \phi_{diff}) \tag{5.19}$$

and

$$\frac{\Delta I_2}{I_2} = \frac{\delta t}{t_0}\cos(\phi_{diff}) + \frac{TG}{T}\cos(k\theta - k\theta_0 + \phi_{diff}) \tag{5.20}$$

The first term $\frac{\delta t}{t_0}\cos(\phi_{diff})$ is the pump probe-like signal termed here as $\frac{\Delta T}{T}$ when the average is calculated (second equation of Eq. 5.16). The tunable variable is θ, which is the

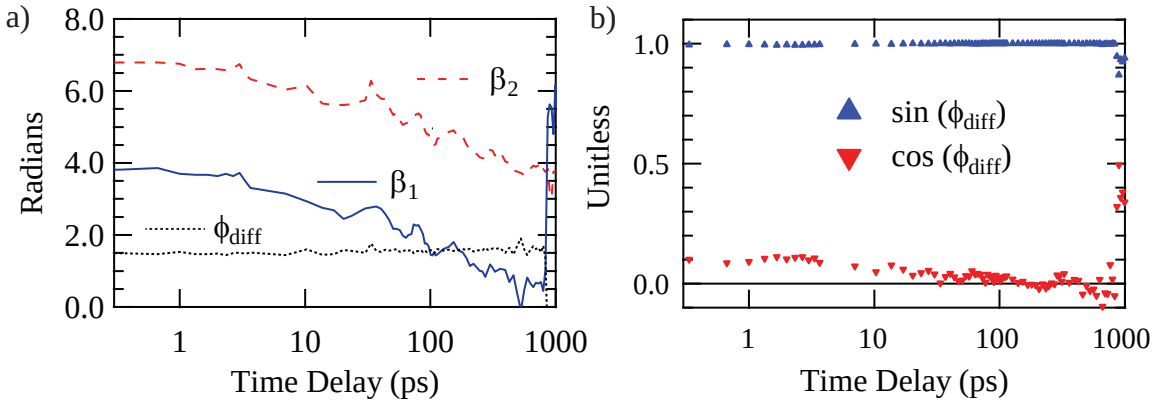

Figure 5.5: a) $\beta_{1,2}$ and ϕ_{diff} in radians as a function of time delay (ps). b) The corresponding sin and cos of ϕ_{diff}. Data is representative of TG data of n-GaN in air at 2.3 μm.

phase difference between the LO and probe beams, and is modulated through rotation of a coverslip. θ_0 is the relative phase of the two pump beams and is an unknown term. Using $\beta_{1,2} = -k\theta_0 \pm \phi_{diff}$, ϕ_{diff} can be determined based on the third equation in eq. 5.16. Fig. 5.5a shows $\beta_{1,2}$ and ϕ_{diff} obtained from this analysis. Fig. 5.5b shows the cos and sin of ϕ_{diff} which can be used to separate out the refractive and absorptive parts of the signal based on eq. 5.17.

β can vary randomly during data collection due to drift. There are multiple methods to control and stabilize ϕ. One method is actively locking $\Delta\phi$ by using an interferometer to output an error signal for a feedback loop that controls the position of one of the optics. [166] Expensive optical setups can ensure very good mechanical stability and minimal phase drift as well. [167] Although time intensive, the simplest method to counteract the drift of ϕ_{diff} is to acquire both signals simultaneously while collecting a full sinusoidal coverslip angle curve at each time delay point as performed here. As shown in Fig. 5.5a, the phase drifts by $\sim$ 3.4 radians after a scan that takes roughly two hours. This drift over the time delay can distort the information extracted if simply taking a time delay scan at one coverslip angle and referencing the kinetics to another time delay scan at another coverslip angle. However, utilizing the phase information of two detectors simultaneously, the calculated ϕ_{diff} is relatively constant throughout the scan despite the drift observed in the individual signal. Additionally, the $\frac{TG}{T}$ signal is independent of this drift because it is directly obtained from the amplitude of the full sinusoidal curve.

5.3 Properties of GaN

Recently, GaN is being explored as a promising photoanode for solar fuel cells. Although GaN has a wide bandgap as illustrated by the absorbance spectrum shown in Fig. 5.6 where

little absorbance occurs until 365 nm, or 3.4 eV, the band positions of both p- and n-type GaN are suitable for both water reduction and oxidation. [31, 168] Nanowires of GaN have exhibited self-driven water photoelectrolysis. [24, 25, 169–171]

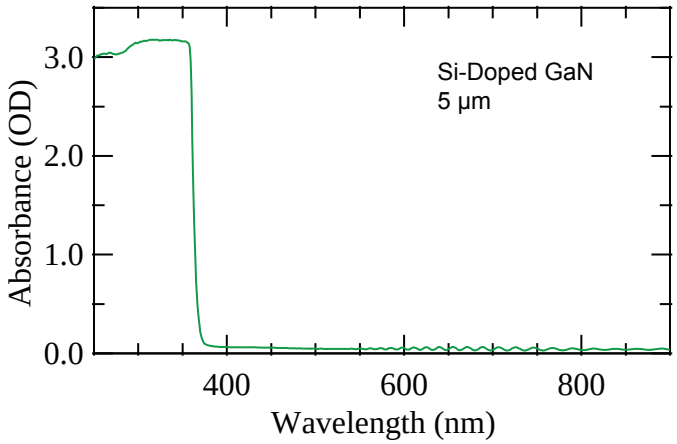

Figure 5.6: Absorbance spectrum for a 5 μm thick Si-doped GaN film

To counter the wide bandgap, alloys of indium and GaN with tunable bandgaps have been engineered that can harness a larger portion of the solar spectrum. [172–174] This alloy has been reported to yield a 1.5% STH under zero bias with simulated sunlight irradiation. [174] Addition of a NiO cocatalyst to the GaN surface shows improved catalytic efficiency and device stability. [175] A combination of GaN and ZnO particles in a solid solution has shown overall self-contained water splitting under visible light albeit with only a couple percent quantum efficiency. [29]

Unlike GaAs which has a small bandgap but deteriorates rapidly in aqueous electrolytes, nitrides like GaN have a strong chemical resistance. However, anodic photocorrosion is still a problem for n-doped GaN because of the upward band bending which pushes photogenerated holes to the surface where GaN is susceptible to oxidation based on the chemical reaction, [176–178]

$$2\mathrm{GaN}(s) + 6h^+ \rightarrow 2\mathrm{Ga}^{3+} + \mathrm{N}_2(g) \tag{5.21}$$

However, addition of a redox couple and maintaining a low photogenerated hole density can suppress photocorrosion. [176, 179, 180] For example, using HBr as the aqueous electrolyte, the photogenerated holes react with Br^- to form Br_3^- instead of reacting with the GaN surface. Both the use of HBr as a hole scavenger and a low pump fluence ensured limited photocorrosion to the GaN surface as shown in the comparison of SEM images before and after measurements in Fig. 5.7.

The undoped and Si-doped GaN (0001) films on C-plane sapphire grown via hydride vapour phase epitaxy (HVPE)-based method used for the experiments were purchased from MTI Corporation (Richmond, CA) as 2" wafers. Films are nominally 5 μm thick. The

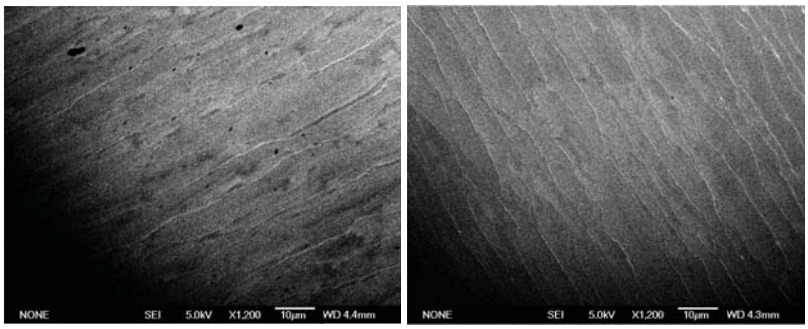

Figure 5.7: SEM images of n-GaN films left: before illumination in air and right: after illumination in 0.1 M HBr.

dopant concentration is $\sim 5 \times 10^{18}$ cm^{-3} as determined by Mott-Schottky experiments. Although zinc-blende GaN exists, it is more commonly found as a wurtzite structure. This wurtzite structure consists of hexagonal unit cells as shown for GaN in Fig. 5.8. Due to the electronegativity difference between Ga and N, a polarity exists. Therefore, a (0001) c-plane surface can be Ga-terminated i.e. Ga-polar or N-terminated (N-polar). The samples purchased from MTI Corporation are Ga-terminated at the (0001) surface.

Samples of ∼1 cm × 1 cm GaN pieces are cleaved from the wafer. Ohmic contact is made between a Cu wire and n-GaN using InGa eutectic and silver paste. Microstop insulating lacquer covers the contact to expose ~ 0.01 cm^2 of n-GaN. The electrolyte solution was 0.1 M HBr unless otherwise mentioned and constantly stirred during measurement.

GaN is widely studied both experimentally and theoretically as a model for applications in catalysis because of its interesting surface chemistry. At the GaN/electrolyte interface,

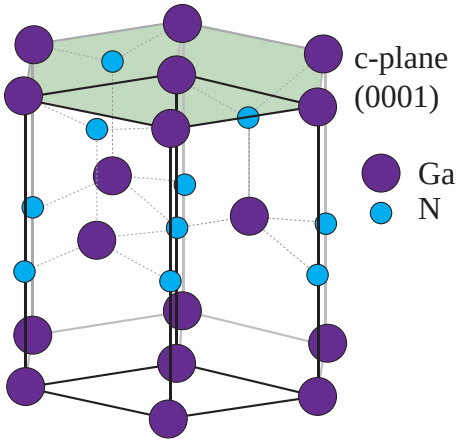

Figure 5.8: Wurtzite GaN Hexagonal Unit Cell: Shaded area indicates the (0001) c-plane representative of the surface.

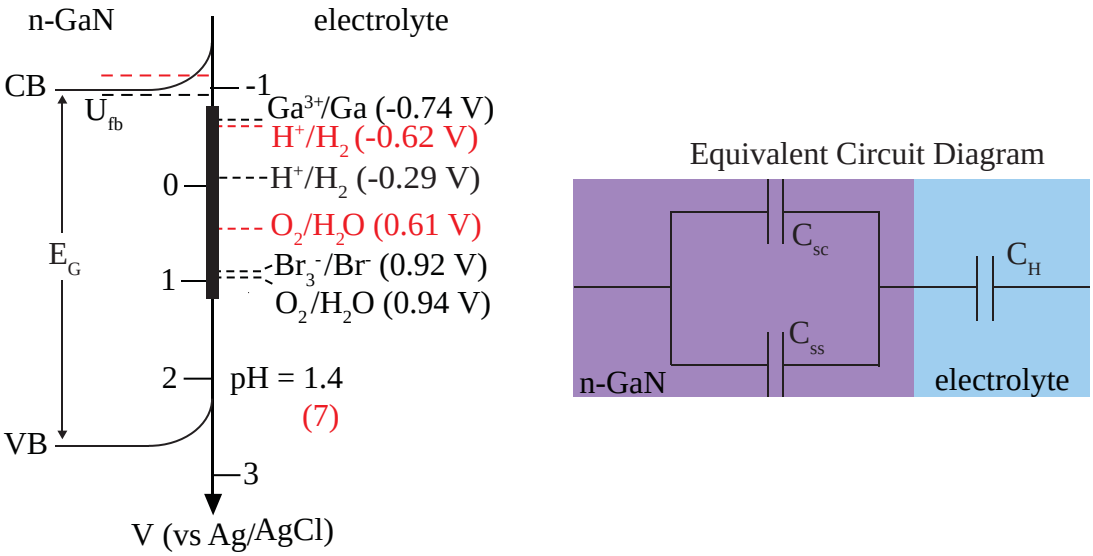

Figure 5.9: Right: Band diagram for n-GaN with the reduction potentials of H^+/H_2, O_2/H_2O, Ga^{3+}/Ga and Br_3^-/Br^- in solution at pH = 1.4 (7). The black band indicates the interfacial mid-gap states formed upon equilibration. Left: An equivalent circuit diagram for the n-GaN/electrolyte system with surface states.

equilibration with the aqueous environment forms interfacial mid-gap states. These mid-gap states have been reported to mediate catalysis by pinning the Fermi level. [181, 182] The band diagram with corresponding redox potentials and an equivalent circuit diagram shown in Fig. 5.9 describes the n-GaN/electrolyte system. Since the mid-gap states form upon dark equilibration rather than upon illumination as sometimes observed [183], the open circuit conditions for the TGS experiments should still probe a relevant catalytic-like surface. This catalytic-like surface consists of possible reaction intermediates for the water oxidation reaction that are formed by the trapped surface charge.

5.4 Results

5.4.1 Steady-State Photoelectrochemistry

Steady-state photo-electrochemical experiments, *e.g.* CV, open circuit potential (OCP) and EIS, on GaN are important characterization methods to understand the material properties of the semiconductor. For n-GaN, it also establishes the extent to which reactions at the n-GaN/aqueous interface are mediated by interfacial mid-gap states.

CV characterizes the absorbed photon-to-current efficiency (APCE) which is a measure

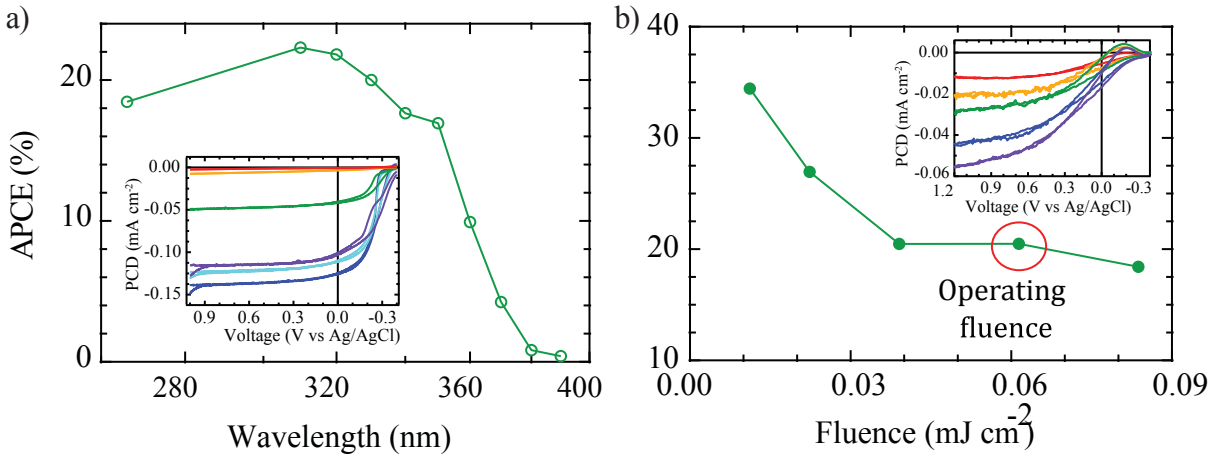

Figure 5.10: n-GaN photo-electrochemistry: a) APCE (%) vs wavelength Inset: Photocurrent density (PCD) (mA cm^{-2}) vs voltage (V vs Ag/AgCl). Illumination performed with Xe arc lamp b) APCE (%) vs fluence (mJ cm^{-2}) Inset: PCD (mA cm^{-2}) vs voltage (V vs Ag/AgCl). Illumination performed with ultrafast pulsed laser.

of the photo-catalytic activity of a material, calculated by

$$APCE = \frac{j_{photo} \cdot N_a \cdot h \cdot c}{\lambda \cdot AP \cdot F} \tag{5.22}$$

where j_{photo} is photocurrent, N_a is Avogadro's constant, h is Planck's constant, c is the speed of light, λ is the excitation wavelength, AP is the absorbed power, and F is Faraday constant. First, the APCE (%) is measured with respect to the wavelength of illumination, shown in Fig. 5.10a, which follows the absorption spectrum shown earlier (Fig. 5.6). The illumination is a continuous light source from a Xe arc lamp. The inset shows the photodiode-like appearance of the CV curves used to determined the photocurrent. Alternatively, the dependence of APCE (%) on fluence is measured (Fig. 5.10b) using illumination from an ultrafast pulsed laser source. The inset shows a similar photodiode-like appearance in the CV. As fluence increases, the APCE (%) decreases due to increased recombination from the higher carrier density. The APCE (%) is unaffected by whether the light source is continuous or pulsed as $\sim$ 20% APCE occurs in both cases. This suggests the dynamics observed in TGS which requires ultrafast pulsed light may also be applicable when irradiated with simulated solar radiation.

Comparison of the effects of illumination on the capacitance were tested with both continuous light from a Xe arc lamp (Fig. 5.11) and short-pulsed light from a Ti:sapphire laser (Fig. 5.12). In addition, two active areas are compared, either the exposed sample area is larger or comparable to the illuminated area. Fig. 5.11 shows Mott-Schottky plots that allow determination of the flatband potential (U_{fb})and dopant concentration (n_0) from the

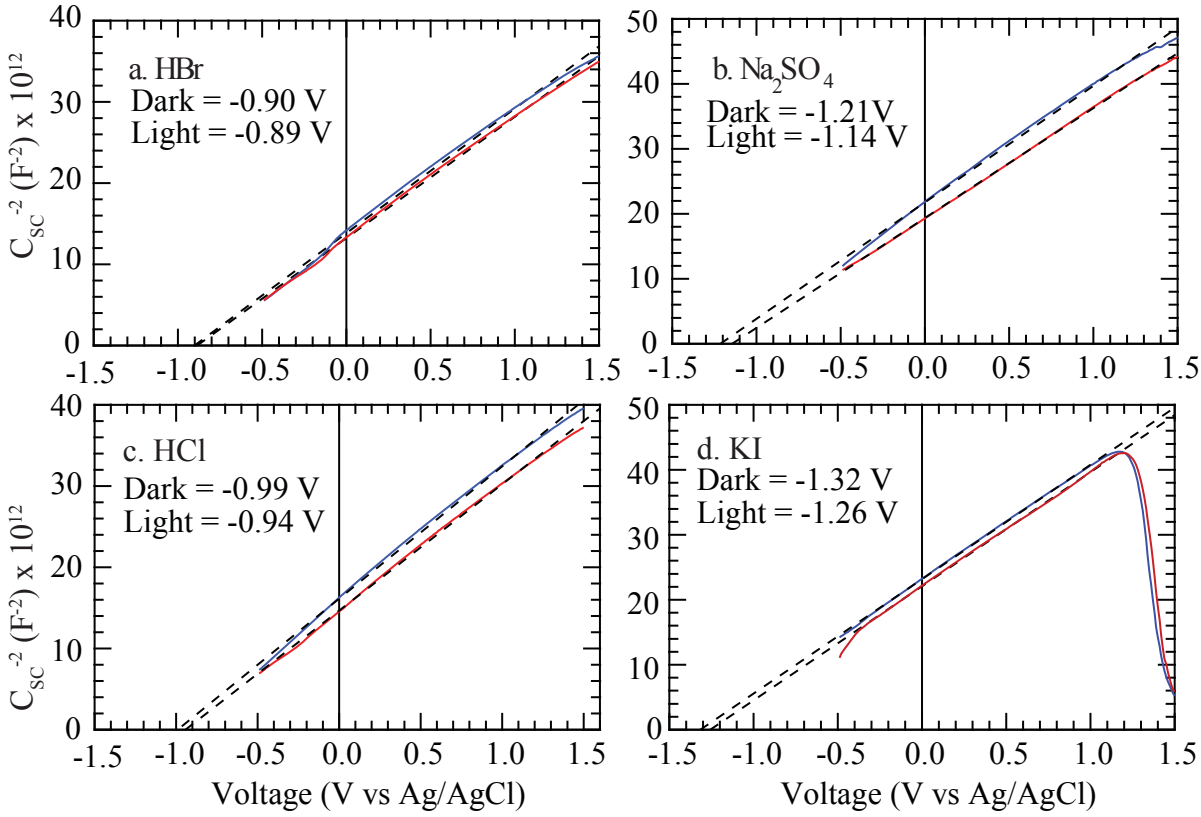

Figure 5.11: Mott-Schottky plots with C^{-2} vs voltage. A.C. voltammetry measurements were performed at a frequency of 100 Hz on n-GaN in multiple aqueous electrolytes in the dark (blue) and illuminated (red) at 266 nm from a Xe arc lamp. Here the exposed area ($\sim$ 0.1 cm^2) $>$ illuminated area

intercept and slope, respectively, of a best-fit line according to the Mott-Schottky equation,

$$\frac{1}{C^2} = \frac{1}{C_{\mathrm{H}}^2}\left\{1 + \frac{2C_{\mathrm{H}}^2}{e_0 \epsilon \epsilon_0 N_{\mathrm{d}}}\left(U - U_{\mathrm{fb}} - \frac{kT}{e_0}\right)\right\} \tag{5.23}$$

The flatband potentials are given for each electrolyte in the dark and under illumination. The capacitance measurements also reveal no significant differences in the voltage dependence between dark and laser illuminated conditions (Fig. 5.12). Further evidence that the TGS probes the mid-gap states formed upon dark equilibration and no new surface states form upon illumination.

OCP measurements over time (Fig. 5.13a) describes the equilibrium potential with periodic light off and light on conditions. The linear dependence of the photovoltage (V_{ph}) on the redox potential (V_{redox}) of the solution, highlighted in Fig. 5.13b, exhibits a slope

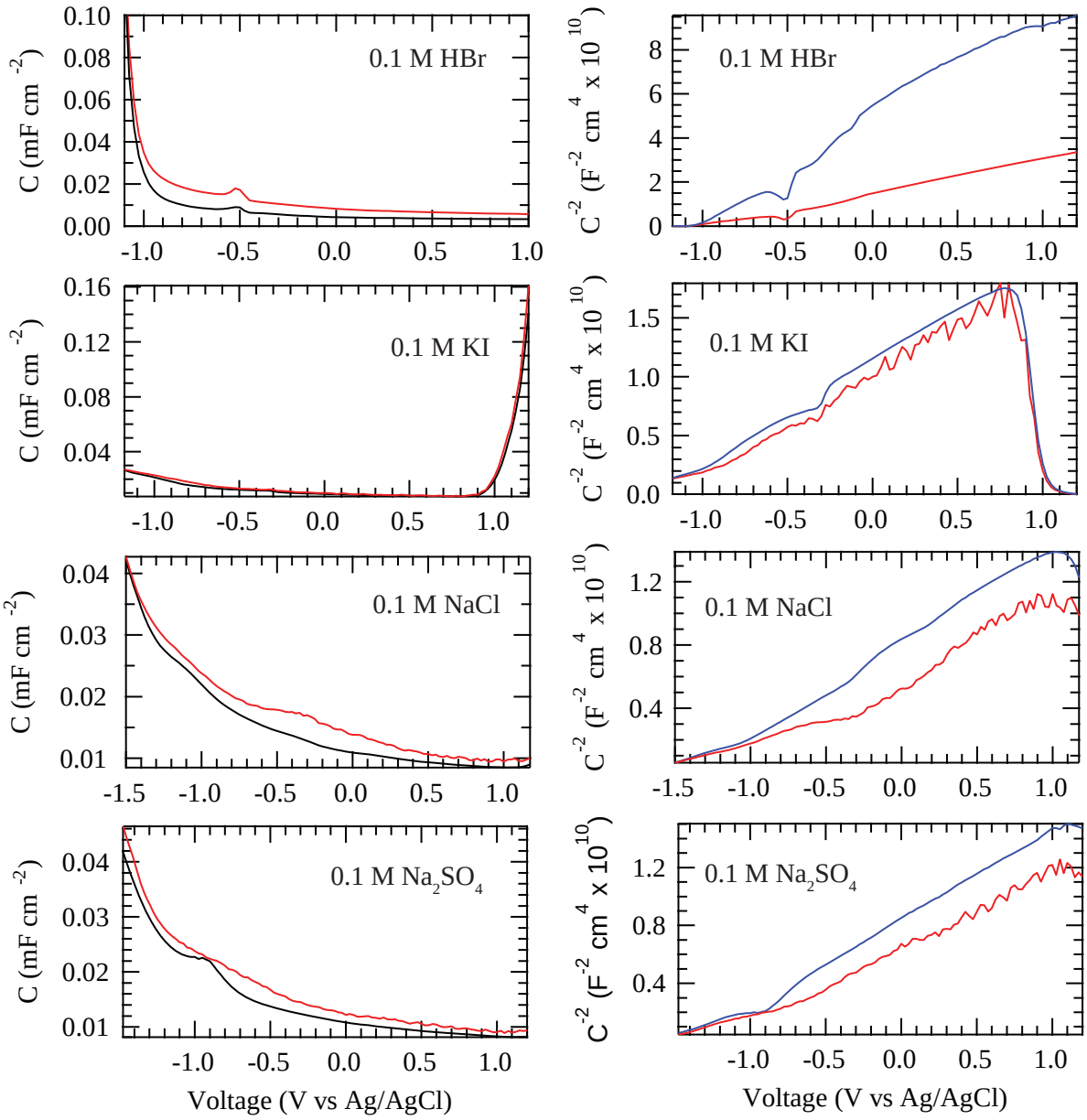

Figure 5.12: A.C. voltammetry measurements yields capacitance with respect to applied potential (left graphs) using a frequency of 1 kHz on n-GaN in multiple aqueous electrolytes in the dark (black or blue) and illuminated (red) at 266 nm pulsed light. Mott Schottky plots are C^{-2} vs voltage (right graphs). Here the exposed area (~ 0.01 cm^2) $\sim$ illuminated area.

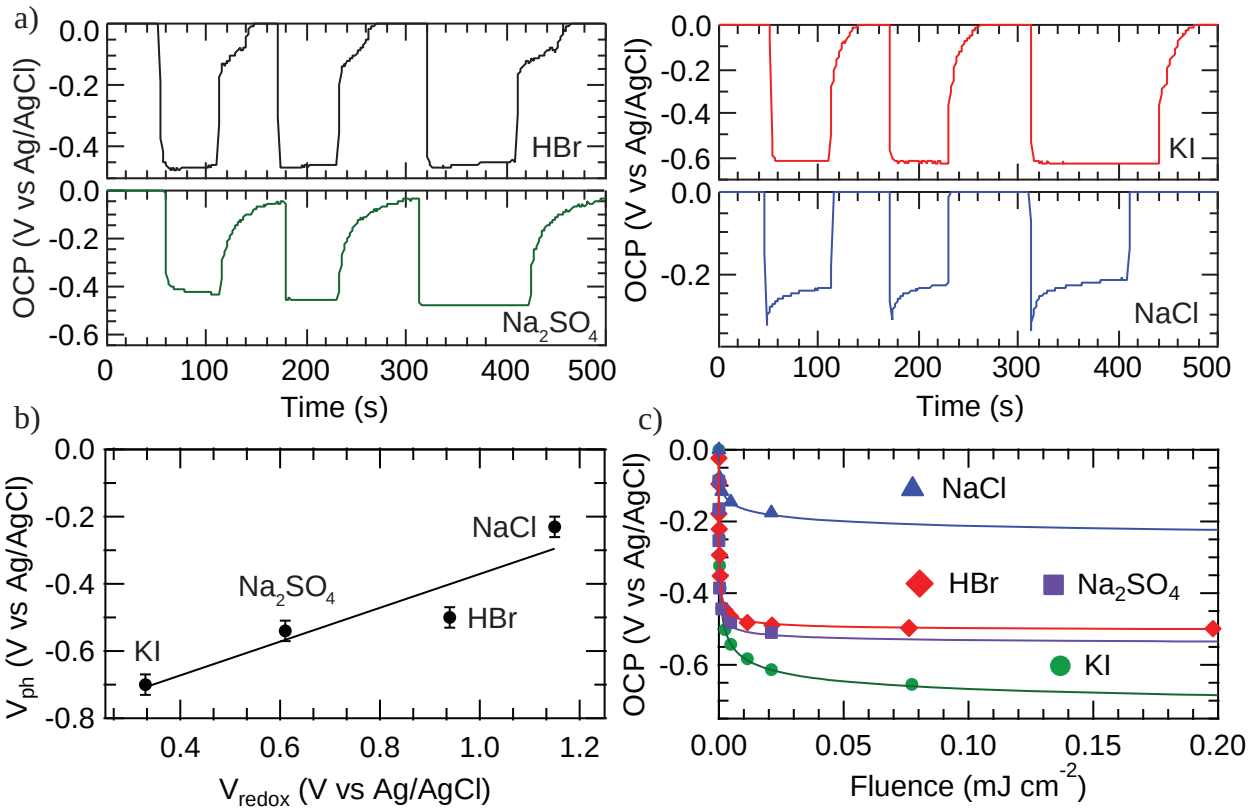

Figure 5.13: a) over time for 0.1 M HBr, Na_2SO_4, KI, and NaCl at light off and light on conditions. b) V_{ph}, photovoltage, with respect to the Nernstian redox potential of various electrolytes. Solid line is linear fit with $dV_{ph}/dV_{redox} \sim 0.6$ c) OCP with respect to fluence (mJ cm^{-2}) for the various electrolytes. Illuminated measurements were performed with 267 nm, 150 fs, 1 kHz pulsed light and only the illuminated area was exposed to the electrolyte.

of ∼0.6. A slope of 1 implies no Fermi-level pinning. [41] V_{ph} is the difference in potential between light off and light on conditions. Fig. 5.13c shows the saturation of the OCP with fluence (mJ cm^{-2}). The experimental fluence applied for the TGS measurements are at the appropriate fluence to flatten the bands. This saturation value is a direct measure of the band bending inside the semiconductor (U_{sc}).

To describe the dark equilibrated surface, the surface charge and potential distribution at the interface are quantified using the steady-state photo-electrochemical experiments mentioned above. [37, 184] First looking at the semiconductor, the charge stored in the depletion layer (q_{sc} (cm^{-2})) is defined by the Schottky approximation as:

$$q_{\mathrm{sc}} = \sqrt{2\epsilon\epsilon_0|e_0|N_{\mathrm{d}}\left(U_{\mathrm{sc}} - \frac{k_{\mathrm{B}}T}{|e_0|}\right)} \tag{5.24}$$

Table 5.1: Surface Charge and Potential Distribution

Interface	U_{redox} (V)	U_{fb} (V)	U_{sc} (V)	U_H (V)	q_{ss} (charge cm^{-2})	$\frac{U_H}{U_{fb}}$(%)
GaN/HBr	0.94	-1.22	0.47	1.7	5.3×10^{14}	78
GaN/Na_2SO_4	0.61	-1.28	0.48	1.41	4.4×10^{14}	74

where ϵ, ϵ_0, e_0, and N_d are the permittivity, vacuum permittivity, electric charge, and doping density respectively. According to the equivalent circuit diagram in Fig. 5.9, q_{sc} (cm^{-2}) and the surface charge at the interface q_{ss} (cm^{-2}) determines the potential drop across the Helmholtz layer according to:

$$U_\mathrm{H} = \frac{q_\mathrm{sc} + q_\mathrm{ss}}{C_\mathrm{H}} \tag{5.25}$$

For a highly doped semiconductor, the measured capacitance depends on both the depletion layer and Helmholtz capacitances, i.e. $\frac{1}{C} = \frac{1}{C_\mathrm{sc}} + \frac{1}{C_\mathrm{H}}$.

$$U_{C^{-2}=0} = U_\mathrm{fb} + 0.059 \times (PZC - pH) + \frac{kT}{e_0} - \frac{e_0\epsilon\epsilon_0 N_\mathrm{d}}{2C_\mathrm{H}^2} \tag{5.26}$$

In the above, the flatband potential is corrected for the small dipole induced by a pH away from the point of zero charge (PZC), approximately pH= 6 in GaN. At open circuit, there is additionally

$$U_\mathrm{redox} - U_\mathrm{fb} = U_\mathrm{H} + U_\mathrm{sc} \tag{5.27}$$

since the only voltage drop across the semiconductor/electrolyte junction is $|U_\mathrm{redox} - U_\mathrm{fb}|$.

Inserting equations 5.25 and 5.26 into equation 5.27 and setting $C_\mathrm{H} = 20\ \mu\mathrm{F/cm}^2$, we determine U_H and q_ss for the different interfaces. Experimental inputs are the intercept of the Mott-Schottky plots in the dark ($U_{C^{-2}=0}$) and the photovoltage (U_sc) for each electrolyte. The surface charge (q_ss) along with the voltage drop across the full junction, U_fb, the depletion width of the semiconductor, U_sc, and the Helmholtz layer, U_H are in shown in the following table for the 0.1 M HBr and Na_2SO_4 electrolytes.

5.4.2 Transient Diffraction Kinetics

Optical excitation generates equal densities of electrons and holes. As a result, the fast moving electrons and slower moving holes are tied together in a coupled diffusive motion due to the internal electric field generated by their spatial separation, commonly referred to as ambipolar diffusivity. The extent to which the TGS provides the ambipolar diffusion coefficient, D_a or is a direct measurement of the hole diffusion coefficient, D_h is given by [185]

$$D = \frac{(n_0 + \Delta N_e + \Delta N_h) D_e D_h}{[(n_0 + \Delta N_e) D_e + (\Delta N_h) D_h]} \tag{5.28}$$

where ΔN_e and ΔN_h are the injected electron and hole carrier concentrations, respectively, D_e and D_h are the individual electron and hole diffusion coefficient, respectively, and n_0 is

the doping density. According to Scajev *et. al.*, two regimes exist for eq. 5.28 as noted by a steep sigmoidal relationship between D and injected carrier density for undoped GaN. [147] The steep sigmoidal relationship implies that, within an order of magnitude of tuning either ΔN or n_0, one of two regime is accessed. For a moderate/high injection regime where $\Delta N_e = \Delta N_h \gg n_0$, the carrier diffusivity behaves as ambipolar $D_a \approx \frac{2D_hD_e}{D_h+D_e}$. On the other hand when $\Delta N_e = \Delta N_h \ll n_0$, the low injection regime is reached and the carrier diffusivity D behaves as D_h.

For undoped GaN, where $n_0 \sim 1 \times 10^{16}$ cm^{-3}, the high injection regime exists for the experimental excitation fluence used during TGS ($\Delta N_e = \Delta N_h \approx 1 \times 10^{19}$ cm^{-3}). Therefore, the kinetics are a reflection of D_a. Since $D_h \ll D_e$ for GaN, TGS measures $D_a \approx 2D_h$. [186]. On the other hand, n-GaN has a $n_0 \sim 5 \times 10^{18}$ cm^{-3} which is comparable $\Delta N_{e/h}$. Although n_0 is comparable to the initial photo-excited carrier density in n-GaN, three factors suggest the TGS for n-GaN is within the low injection regime. First, the carrier density profile, using eq. 5.12, suggests that at the timescale where diffusion starts to dominate (200-400 ps) the effective carrier density has reduced by a factor of approximately 8 (Fig. 5.14a). Secondly, the fluence dependence (Fig. 5.14b) shows no change in the diffusion coefficient even when the initial ΔN is an order of magnitude below n_0. If the TGS kinetics were near the transition from low injection to the high injection regime, the slope obtained from τ^{-1} vs q^2 is expected to shift from D_h to $2D_h$ with ΔN. However, this is not the case even when changing the carrier density by an order of magnitude. Third, the experimentally obtained diffusion constant is that expected for D_h, consistent with half of D_a determine for undoped GaN. Therefore, the TGS kinetics for n-GaN is a direct probe of hole mobility.

When undoped GaN is introduced to an electrolyte environment, *i.e.* 0.1 M HBr, no

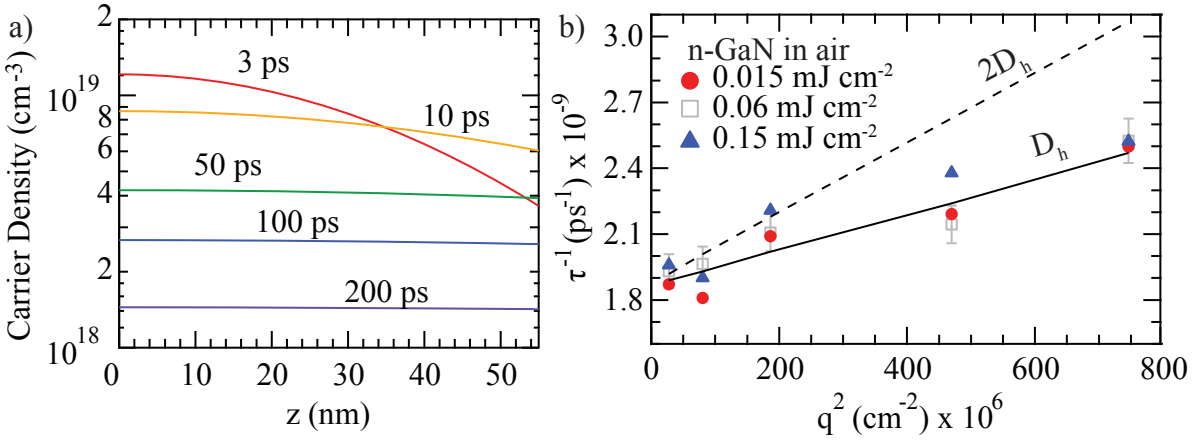

Figure 5.14: a) Photoexcited carrier density profile over a distance of z = $\frac{1}{\alpha}$ = 55 nm at several decay times (3, 50, 100, 500, and 1000 ps) b) τ^{-1} for n-GaN in air vs grating spacing at three fluences: 0.015, 0.06, and 0.15 mJ cm^{-2}. Solid line is slope for D_h while dotted line is sloped expected for $2D_h$.

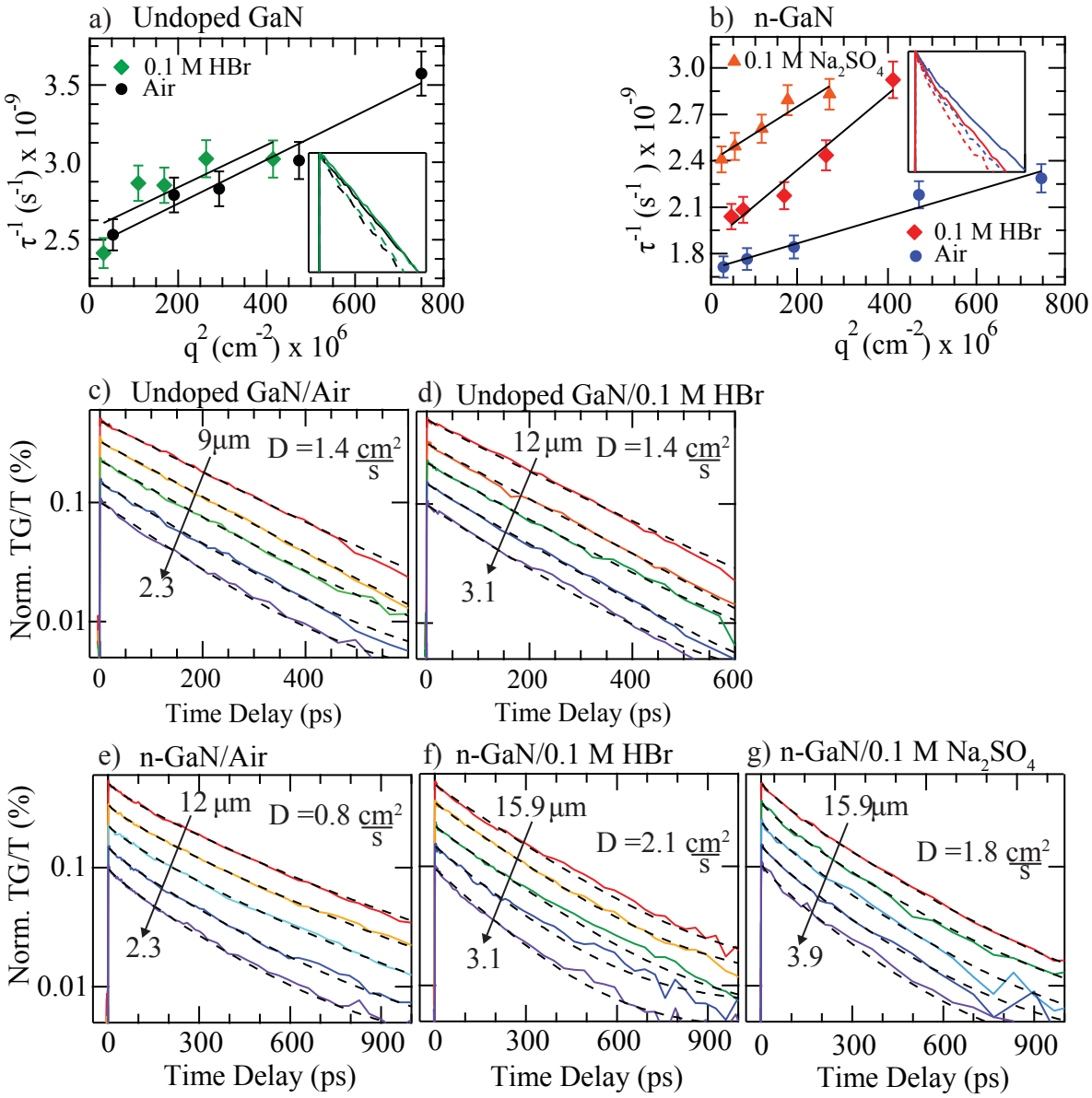

Figure 5.15: Decay rates (τ^{-1}) as a function of q^2 for a) undoped GaN and b) n-GaN in air (circles), 0.1 M HBr (diamonds), 0.1 M Na_2SO_4 (triangles). Slope and intercept obtained from linear fit gives D = 1.4 ± 0.1 cm^2 s^{-1} and 407 ± 10 ps in air and D = 1.4 ± 0.6 cm^2 s^{-1} and 389 ± 19 ps in 0.1 M HBr, respectively, for undoped GaN. D = 0.8 ± 0.1 cm^2 s^{-1} and 585 ± 12 ps in air; D = 2.1 ± 0.3 cm^2 s^{-1} and 505 ± 16 ps in 0.1 M HBr and D = 1.8 ± 0.3 cm^2 s^{-1} and 415 ± 8 ps in 0.1 M Na_2SO_4, respectively, for n-GaN. Error bars represent standard error of fit. Insets: Comparison of normalized TG/T (%) kinetics for largest (solid) and smallest (dashed) grating spacing in air and 0.1 M HBr. Normalized TG/T (%) kinetics (solid) for each grating spacings with TGS differential equation model fits (dashed) for c) undoped GaN in air, d) undoped GaN in 0.1 M HBr, e) n-GaN in air, f) n-GaN in 0.1 M HBr and g) n-GaN in 0.1 M Na_2SO_4. Offsets are added for clarity.

Table 5.2: Variables obtained from fits using diffraction efficiency model

Sample	S ($\frac{cm}{s}$)	D_h ($\frac{cm^2}{s}$)	τ_R (ps)	L_p (nm)
GaN	4.0×10^3	0.7	407	169
GaN (HBr)	7.0×10^3	0.7	389	165
n-GaN	1.6×10^4	0.8	1000	283
n-GaN (HBr)	5.0×10^3	2.1	505	326
n-GaN (Na_2SO_4)	2.5×10^4	1.8	703	356

significant change in diffusivity was observed. As shown in Fig 5.15a, D_h remains 0.7 $\pm$ 0.3 cm^2 s^{-1}. The inset shows the kinetics do not change between air and 0.1 M HBr for both the largest and smallest Λ. Importantly, the data exhibit no substantial difference in kinetics for the range of grating spacings measured. For n-GaN, the diffusivity behaves differently from undoped GaN when in solution. Here, D_h is 0.8 $\pm$ 0.1 cm^2 s^{-1} in air consistent with undoped GaN in air. However, a significant increase in D_h to 2.1 $\pm$ 0.3 cm^2 s^{-1} is observed at the n-GaN/0.1 M HBr electrolyte interface (Fig. 5.15d). The change in kinetics between air and 0.1 M HBr environments is highlighted at the smallest and largest grating spacing in the inset of the Fig. 5.15d. The data over a range of grating spacings show significantly faster kinetics in electrolyte (Fig. 5.15f) compared to air (Fig. 5.15e). The data and analysis show that D_h increases at the 0.1 M HBr interface by a factor of 2.6 from the air interface. The increased hole diffusivity at the n-GaN/aqueous interface is not unique to an HBr electrolyte at pH = 1.4, but also occurs with an Na_2SO_4 electrolyte at pH = 7, as shown in Fig. 5.15b. For 0.1 M Na_2SO_4, D_h is 1.8 $\pm$ 0.3 cm^2 s^{-1}, a factor of 2.25 increase from air. The lack of a pronounced difference between the two electrolytes is reflected in the similar behavior of the photovoltages (Fig. 5.13a) for HBr and Na_2SO_4 and that both interfaces lead to $q_{ss} \sim 10^{14}$ cm^{-2}. Taken together, equilibration to the H_2O/O_2 redox potential is assumed to control the unique n-GaN/aqueous electrolyte interface, which changes the lateral diffusivity.

While the surface is a mixture of surface-adsorbed water species regardless of electrolyte composition, the electrolytes could affect the defect densities. As mentioned previously, this defect density is quantified by the S reported in Table 5.2 and obtained using eq. 5.12 based on fits to the TG kinetics. Fig. 5.16 shows how the fits change when S is changed while D and τ are kept constant, giving us a confidence interval for the extracted value. A 20% error is observed with $\pm 0.8 \times 10^4$ cm/s change in S.

For undoped GaN, S = 4×10^3 $cm\ s^{-1}$ which agrees with previous experiments. [187] No change is observed when an aqueous electrolyte environment is introduced. For n-GaN/HBr, the aqueous electrolyte environment does significantly affect the surface passivation, leading to almost an order of magnitude decrease in S from $\sim 10^4$ $cm\ s^{-1}$ in air to $\sim 10^3$ $cm\ s^{-1}$. On the other hand, for the n-GaN/Na_2SO_4 aqueous interface, the S remains similarly high as at the air interface. This suggests that, while the defect density and surface recombination velocity are sensitive to the specific counter ions and pH of the aqueous electrolyte, the interfacial hole diffusivity is not. The substantially lower S for HBr is likely related to the

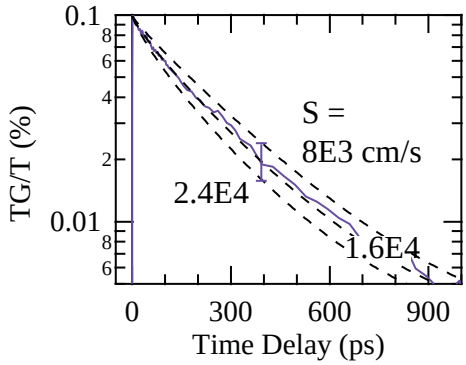

Figure 5.16: Theoretical η kinetic dependence (dotted line) on S using parameters obtained from the experimental n-GaN/air TGS kinetics (solid line) at $\Lambda = 2.3$ μm. A representative 20% error bar is shown.

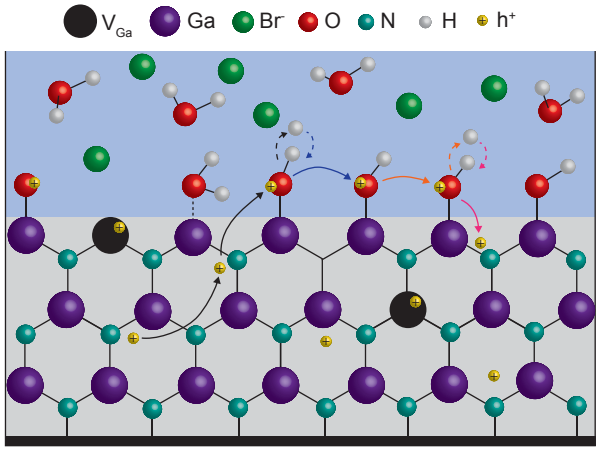

Figure 5.17: GaN(0001) surface with Ga sites terminated by H_2O, OH, and O^* after equilibration with an aqueous 0.1 M HBr electrolyte. Holes from the nitrogen valence band hop on the surface (solid arrows), accompanied by proton release and capture (dotted arrows), before returning to the bulk.

lower photocorrosion, as compared to Na_2SO_4. The lower S suggests HBr mediates reactions that avoid trapping holes in defect sites of GaN, thought to create Ga^{+3}. [176–178]

The increase in the lateral hole diffusivity occurs uniquely at the n-GaN/aqueous electrolyte interface. When the n-GaN/aqueous electrolyte interface equilibrates with the H_2O/O_2 redox potential, a surface charge develops simultaneously with the depletion layer in the semiconductor and Helmholtz screening layer at the interface. This surface charge modifies the surface adsorbed water composition. On the other hand, at the n-GaN/air interface and undoped GaN/electrolyte interface, the depletion layer and Helmholtz screening layer

develops separately. No substantial surface charge develops and hole diffusivity remains ∼ 0.7-0.8 cm^2 s^{-1}. The n-GaN polar surface in solution is composed of a distribution of water adsorbates, possibly intact water molecules, O adatoms, H adatoms, and hydroxyl groups, based on DFT calculations. [188–190] During equilibration, a significant population of Ga-OH and Ga-O^* forms, as suggested by ambient pressure photoemission of the n-GaN (0001) surface exposed to water [191, 192] and by calculation of time scale evolutions of excited holes at different GaN surfaces. [193] At 300 K, phonon-assisted charge carrier hopping accompanied by proton-coupled electron transfer is expected between sites. [194]. Therefore, the equilibrated surface, consisting of localized charge (*e.g.* Ga-O^*) and neighboring sites to which the charge can easily hop (*e.g.* Ga-OH) should increase surface hopping mobility as depicted in Fig. 5.17. In the energy band description of this interface, equilibration increases the density of surface states and broadens the mid-gap band [195] of the n-GaN/aqueous interface with respect to the undoped GaN/air, undoped GaN/aqueous, and n-GaN/air interfaces. Surface hopping could affect carrier mobility for many lattice lengths into the bulk for two reasons: (1) The surface states form a narrow, mid-gap band such that energy shifts in the photoluminescence reflect their filling with pH, as observed on GaN [181] and (2) Diffusion lengths are ∼200 nm in GaN (Tab. 5.2).

The increased interfacial carrier mobility can be considered one step in the catalytic process that creates a current pathway at the solid-liquid interface. One way to quantify the opening of this current pathway is through the mean square displacement of the charge carrier profile from the average position of the initial profile, $< x^2 >$ (t), along the air vs. electrolyte interface. The mean square displacement, according to $< x^2 > \sim Dt$, increases by the same factor as the diffusivity, or by 2.6 at the n-GaN/HBr interface. The standard deviation ($\sqrt{< x^2 >}$) of the carrier profile is 60% higher and hence, a 60% larger interfacial distance is traversed at the electrolyte interface. Another way to quantify the opening of the current pathway, especially important for photo-catalysis, is the hole diffusion length (L_p) = $\sqrt{D_h \tau_R}$. [196] The L_ps for the different interfaces are shown in Table 5.2. For undoped GaN in air and in aqueous electrolyte, L_p is $\sim 200\ nm$ in agreement with previous experiments. [197] L_p increases by $\sim 100\ nm$ for n-GaN, but mostly due to the increased recombination time τ_R. On the other hand, an additional $\sim 50\ nm$ is observed when an aqueous electrolyte is introduced to the n-GaN surface and is due to the increased diffusivity, since τ_R lowers. This demonstrates that at the n-GaN/electrolyte interface, photo-holes will diffuse longer distances before recombining as a direct result of the increased diffusivity.

5.4.3 Comparison of Transient Absorption vs Transient Grating

Kinetics obtained from conventional pump probe measurements differ significantly from the TG dynamics (Fig. 5.18). Conventional pump probe elucidates changes from the absorptive component of the material or the imaginary third order susceptibility. However, TGS adds to that by also probing the dispersive component or real part of the third order susceptibility. Dispersion is an important and often overlooked characteristic in charge transfer dynamics.

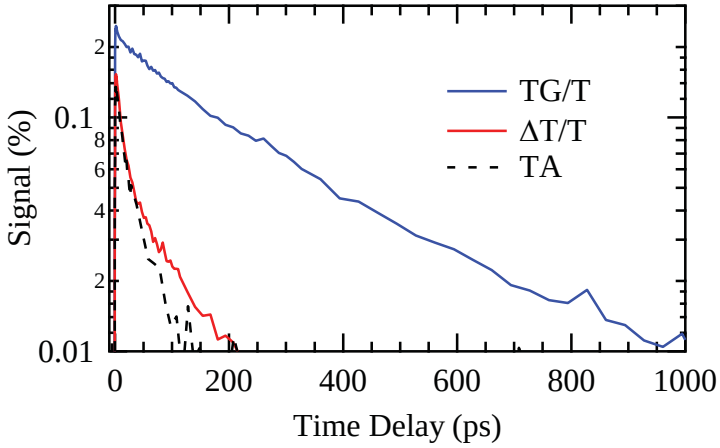

Figure 5.18: Comparison of TGS ($\frac{TG}{T}$ and $\frac{\Delta T}{T}$) and TA kinetics. TG data represents a n-GaN in air sample at $\Lambda = 2.3$ μm pumped with $\sim$0.05 mJ cm^{-2}. TA data represents n-GaN in air excited with $\sim$0.025 mJ cm^{-2}.

Although the transient absorption (TA) and $\frac{\Delta T}{T}$, which is analogous to a pump-probe signal, shows all the photo-excited carrier concentrations have decayed within $\sim$200 ps, TGS provides an alternative picture (Fig. 5.18). Therefore, the longer lived signal (up to 1000 ps) in the TG kinetics must originate from the real component of the heterodyne transient-grating signal. According to the ϕ_{diff} of the n-GaN diffracted signal (in ambient conditions) determined from heterodyne detection, the TG kinetics are solely from a phase grating. Shown in Fig. 5.5 b), $\cos(\phi_{diff})$ is 0 and $\sin(\phi_{diff}) = 1$. Therefore, from eq. 5.17, $\cos(\phi_{diff})\mathrm{ImP}^3 = 0$ and $\sin(\phi_{diff})\mathrm{ReP}^3 \neq 0$.

From the TG kinetics, the photo-excited carrier concentration has not all recombined within the fast timescale but, rather, the carriers may have gone into an "invisible" trapped state. One that does not change the absorptive properties of the material but does have a large effect on the dispersive properties. This lends further evidence to the schematic depicted in Fig. 5.17 where hole transport is assisted by mid-gap surface states. The mechanism of hole hopping occurs through localization of the charge carrier from a discrete set of trapping sites. Therefore, a greater concentration of these trap transport sites leads to larger diffusion due to the dispersive nature of hole transport. This type of dispersive transport has been used previously to describe the anomalous transport observed in amorphous semiconductors where large amounts of disorder leads to greater amounts of diffusion and dispersive spread than in an ordered semiconductor. [198, 199]

5.4.4 Voltage-Dependent Kinetics

The TG kinetics also show dramatic differences from the TA kinetics with applied potential (Fig. 5.19). Since the decay of the ΔT/T (%) signal is independent of applied potential

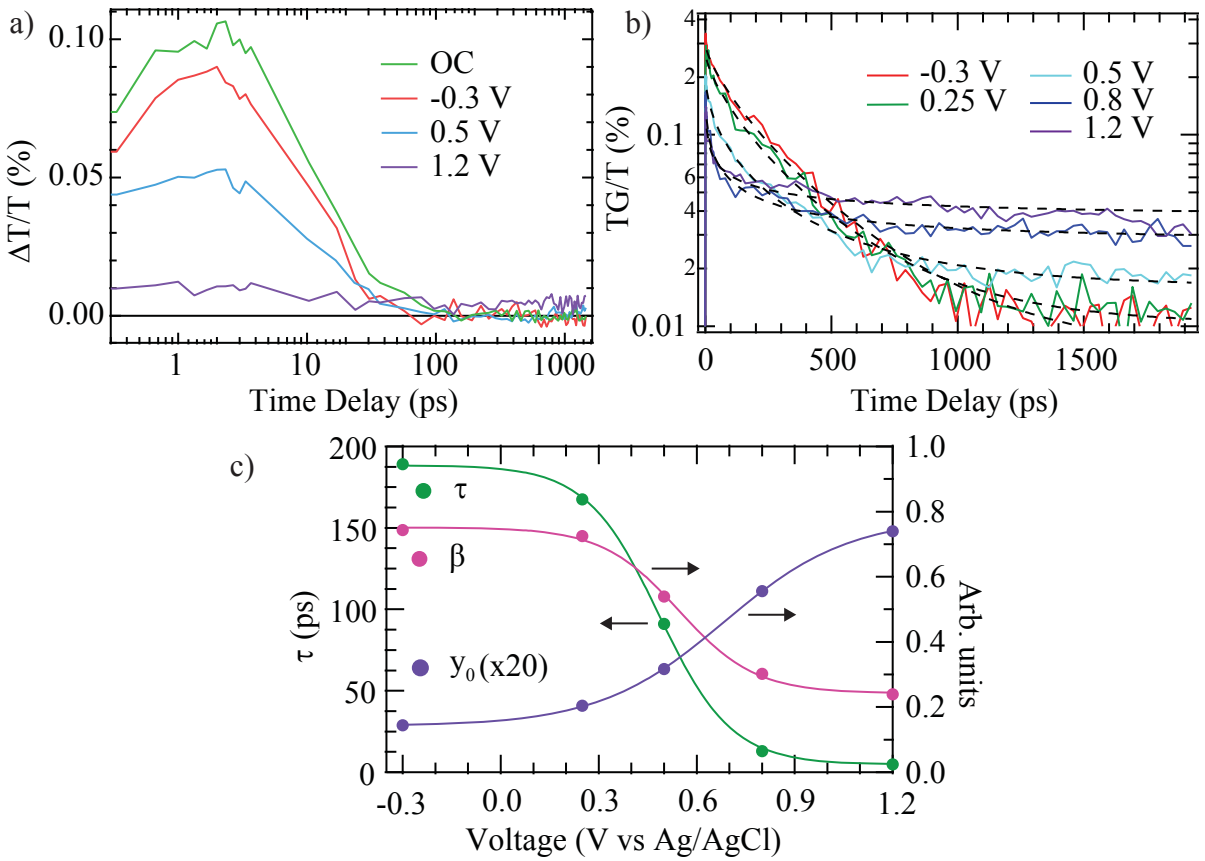

Figure 5.19: a) ΔT/T (%) from pump probe experiments and b) TGS kinetics (%) (Λ = 5.6 μm) at multiple applied potentials (-0.3, 0.25, 0.5, 0.8 and 1.2 V) for n-GaN (solid lines) and corresponding stretched-exponential fits (dashed lines). c) τ, y_0, and β from stretched exponential fits with respect to applied potential. Solid lines are guides for the eyes.

but the amplitude of the signal decreases dramatically at large positive potentials, it is proposed that the photo-excited holes have gone into an alternative pathway, promoted by the large positive potentials. Therefore, instead of the free carriers simply recombining within 15 ps, as suggested by TA, these free carriers enter into a trapped state. One that the TG method is able to probe as evidenced by the notable changes in the kinetics with applied potential. Previous time-resolved infrared absorption spectroscopy (TR-IR) was able to observe potential-dependent kinetics on n- and p-type GaN which suggested greater efficiency of carrier separation from bigger band bending at larger applied potentials and, thus, decreased recombination rates and longer electron lifetimes are responsible for the potential-dependent activities of the water splitting reactions. [200] However, due to the insensitivity of TR-IR to holes, it could not directly link the kinetics to the water oxidation reaction in n-GaN. For TGS, as mentioned previously, the kinetics are sensitive to hole dynamics and

direct observation of the relationship between the behavior of charge carriers under bias and enhanced STH efficiency can be made, allowing for elucidation of the mechanism during catalytic conditions.

Shown previously, the anodic photocurrent density from the oxidation of water starts to flow above -0.3 V as shown in Fig. 5.10b and the amplitude of the current increases with increasing positive potential. This current behavior is consistent with previous studies on n-GaN. [168, 170, 200] Referencing this steady state measurement, TGS kinetics were performed at multiple potentials corresponding to different photocurrent activities. First, a -0.3 V bias was applied which is consistent with open circuit conditions as very little current flows at this potential. Incrementally stepping up the potential from -0.3 V to 0.5 V corresponds to the biggest change in photocurrent. Between 0.5 V and 1.2 V, the photocurrent density stays relatively constant at the operating fluence.

Keeping the reaction efficiencies in mind, the TGS kinetics at different applied potentials are shown in Fig. 5.19b) for $\Lambda = 5.6$ μm. Although quantitative measurement of the lateral diffusivity could not be performed reliably under applied potential conditions due to changing surface conditions and non-mononexponential decay kinetics, notable voltage-dependent kinetics are observed in the charge dynamics. A stretched exponential, $y = y_0 + A \cdot exp(-(\frac{t}{\tau})^{\beta})$, best fits the kinetics in this case and the results of the fits are plotted with respect to applied potential in Fig. 5.19c. With increasing positive potentials, the signal decays faster at early times, from a lifetime (τ) of $\sim$ 200 ps to $\sim$ 5 ps, while a large offset (y_0) signal grows in at later times. The sigmoidal-like shape of τ and y_0 are indicative of a transition in charge dynamics occurring around 0.5 V. This voltage corresponds to the rise in the photocurrent density (Fig. 5.10) and the photovoltage amount required to flatten the bands (Fig. 5.13) which is also consistent with previous studies which found a band bending of 0.4 eV for n-GaN. [201] Therefore, the initial decay of signal observed at high potentials is believed to occur from a hole-consuming water oxidation reaction occurring at the n-GaN surface. This is proposed to be the first hole transfer accompanying the first step in the oxidation of water. Following this hole transfer, a longer lived intermediate forms and the next hole transfer process must occur at a slower, 10s of ns or greater, timescale. Evidence of direct observation of surface trapped states comes from the absence of signal when the surface is not refreshed, *i.e.* the electrolyte solution is not stirred. Furthermore, the detection of the reaction intermediate shows a saturation in the signal suggesting a saturation in the number of holes captured at available active surface sites.

The relaxation of many disordered systems have been found to follow this stretched-exponential law relationship which is believed to originate from the dispersive diffusion of photoexcited carriers due to hopping between different localized states. [202–204] The stretching parameter β ($0 \leq \beta < 1$) is considered the dispersion factor and measures the density of localized states. When β is near unity, the behavior is close to a simple exponential decay and dispersion is negligible. Therefore, when β decreases from $\sim$ 0.7 to 0.2 with increasing positive potentials, there is an increase in dispersion. This suggests that during catalysis surface disorder increases and is accompanied by an increase in the density of localized states which could lead to larger diffusivities.

5.5 Conclusion

Transient grating spectroscopy reveals interesting behavior in carrier diffusivity and voltage-dependence that could not have been observed with traditional transient absorption spectroscopy. Quantitative determination of the carrier diffusivity suggests a significant increase in the mobility of interfacial charge carriers when the surface is able to equilibrate with a redox couple, as in the n-GaN/electrolyte system. Based on ϕ_{diff} determined via heterodyne detection, the TG signal detects the dispersive properties of the material which are voltage dependent. These voltage-dependent kinetics describe a hole undergoing a fast initial charge transfer followed by a long ns lifetime where the intermediate formed is awaiting the next charge transfer step.

It is proposed that the local environment of water adsorbates (-OH, -H, and -O adatoms) leads to mobile hole hopping. Since oxidative catalysis proceeds from these starting reactants, the work suggests that surface reactivity and interfacial mobility are profoundly interdependent. The dark composition of water adsorbates creates surface intermediates that can transfer charge to reactant molecules and increase the speed with which charges reach the surface sites. Although quantitative determination of the carrier diffusivity could not be determined reliably when a steady catalytic current occurs, the TGS kinetic changes observed with applied potential suggests direct observation of hole dynamics. The voltage-dependent kinetics are indicative of a fast 5 ps hole transfer followed by a much longer lived intermediate surface state. This state gets saturated at large positive potentials. This work lays a nice foundation for using the TGS method to explore hole dynamics, particularly at surface sites which may be "invisible" to traditional transient absorption methods. Additionally, it shows that reducing recombination rates is not the only factor to improve device efficiencies but, rather, manipulating the surface active sites to accommodate better hole capture. It would be interesting to explore how surface modifications (e.g. co-catalysts) affects hole diffusivity and decay kinetics in the future using this method.

Appendix A

Co_3O_4/ZnO Heterojunction

It was established in Chapter 3 that the charge dynamics of Co_3O_4 was invariant to a number of external tuning parameters due to the recombination from an efficient intrinsic mid-gap trap state. Additionally, the insensitivity was also addressed to the extent the observed transients are dependent upon the chemical milieu at the surface. A dependence of the kinetics on surface chemical species is expected if surface-related traps play a prominent role in the carrier dynamics [205] either because interfacial electric fields gives rise to charge carrier separation [52, 58] and/or from competition between interfacial carrier transfer and carrier capture. [52] To that end, the transient decay kinetics as a function of an aqueous electrolyte with varying pH were measured, as shown in Fig. A.1. In line with previous experiments on Co_3O_4, the decay kinetics are invariant with respect to the surface adsorbates and surface electric field created by these different electrolytes. These *in situ* experiments provide further support that the nature of the efficient traps are intrinsic mid-gap states (*e.g.* the *d* states and/or the Co vacancies) rather than surface-related defect states.

The insensitivity to external controls, then, makes it tricky to isolate the hole dynamics

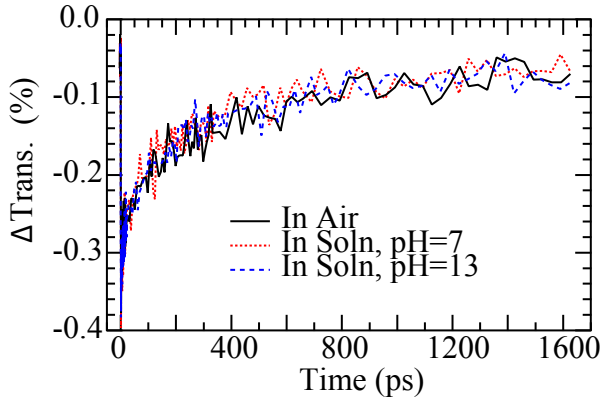

Figure A.1: Transient traces obtained from a 10 nm Co_3O_4 film on ITO-covered glass substrate. $\lambda_{exc} = 520$ nm; $F_{abs} \sim 0.4$ mJ cm^{-2} and probed at 600 nm.

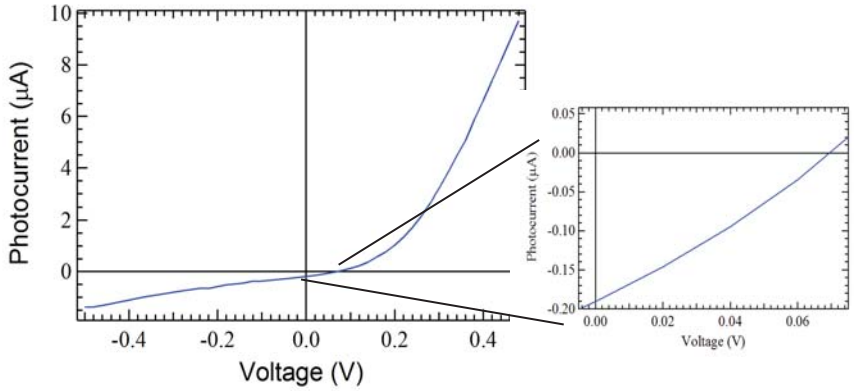

Figure A.2: Photocurrent-voltage curve of Co_3O_4/ZnO heterojunction.

from the recombination kinetics of Co_3O_4 and truly optimize this material for water oxidation catalysis. This necessitates utilizing a built-in electric field between Co_3O_4 and another material. A Co_3O_4/ZnO heterojunction was briefly explored to see if the kinetics could be altered in this way. The photocurrent-voltage relationship, shown in Fig. A.2 shows the rectifying behavior of the junction when illuminated with a continuous 405 nm diode. With positive applied potential, the system is forward biased and large current occurs. With a negative applied potential, the system is reversed bias and there is minimal charge flow. However, there is a presence of a small photocurrent in the reverse bias, suggesting that this device is photo-active. The transient decay curves are compared based on open circuit, forward bias, and reverse bias conditions (Fig. A.3) where only Co_3O_4 is probed at 600 nm and excited at 520 nm. The presence of the built-in electric field from the heterojunction shows the charge dynamics of Co_3O_4 can be altered to a small extent. Using the open circuit condition as a reference, the signal decays slower with -1 V reverse bias and faster with +1 V forward bias. A double exponential best fits the decay kinetics and shows an increasing τ going from 175 ps to 308 ps to 340 ps between +1 V, OC, and -1 V, respectively. As expected when a -1 V reverse bias is applied, the band bending at the space charge region grows, resulting in better separation of charge carriers leading to longer lifetime. In contrast, a forward bias decreases the electric field and recombination can occur more easily. These results set the stage for tuning the properties of TMOs with extensive mid-gap states using heterojunctions, possible in photovoltaic devices.

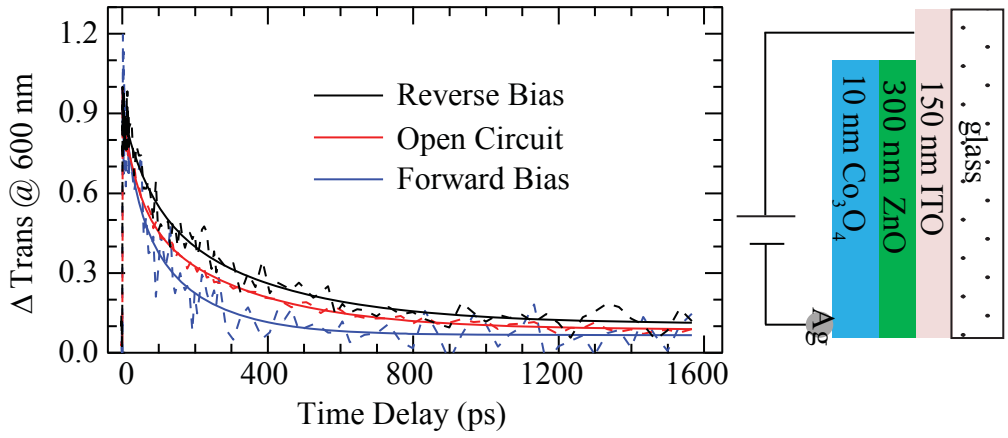

Figure A.3: Transient decay kinetics of Co_3O_4/ZnO heterojunction with bias (dotted) and double exponential fit (solid) along with schematic of heterojunction system.

Appendix B

Resonant Inelastic X-ray Scattering

Although XAS was unable to differentiate differences in the electronic structure of an active and non-active water oxidation catalyst as discussed in Chapter 4, RIXS may be a more sensitive technique to investigate the structure-activity relationship. RIXS is a two photon technique in which XAS is combined with X-ray emission spectroscopy, a schematic representation of the processes is shown in Fig. B.1. [105, 206] For RIXS, the incident X-ray energy E_i which corresponds to a resonance peak in the XAS spectrum is kept constant. The absorption of that X-ray photon results in an excitation and an intermediate state with a core hole. Radiative emission occurs when an electron in the valence state fills that core hole and the emission ω ($\neq E_i$) is energy resolved to form the RIXS spectrum. The RIXS spectrum, then, measures the energy difference between the conduction and valence band

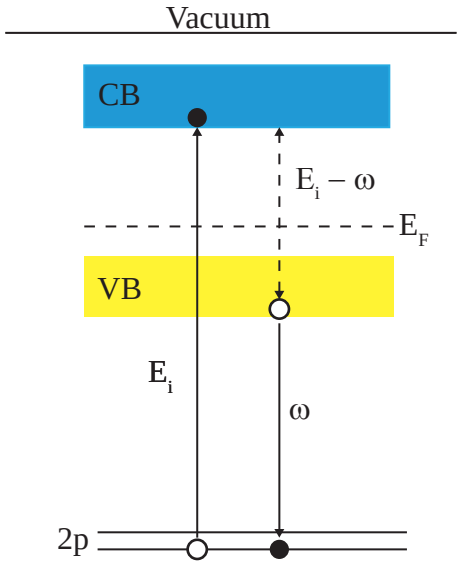

Figure B.1: Schematic representation of RIXS

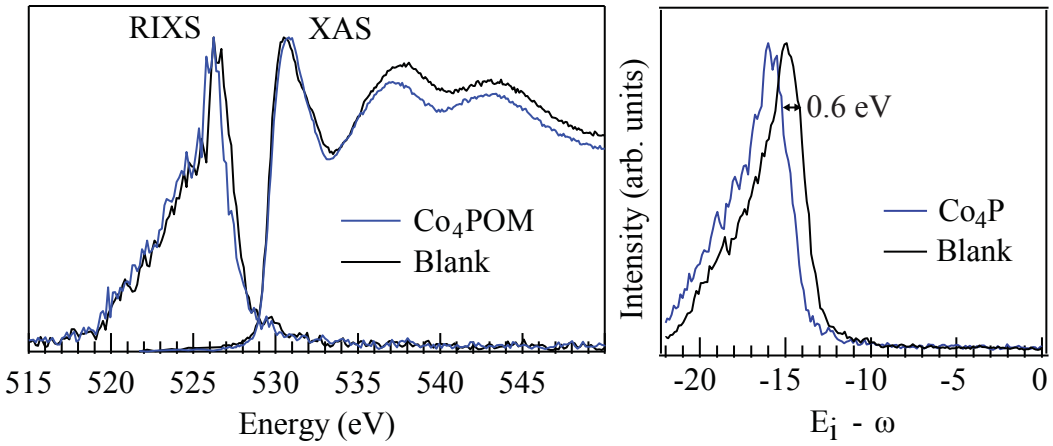

Figure B.2: Right: Comparison of RIXS and XAS at the O K-edge and left: close up comparison of O K-edge RIXS of a Co_4P and a blank POM.

based on E_i - ω which makes it a far more informative technique than XAS. In addition to RIXS, the O K-edge also holds additional information, *e.g.* metal-oxygen hybridization, that can be useful for differentiating the electronic structure of systems with similar metal atom valence state and geometry but differing in number of metal atoms and ligand identity. [207] Combining these two, *i.e.* O K-edge RIXS, has yielded interesting information that may possibly be linked to relevant $d-d$ transitions.

One example is given to show distinct energy differences within the O K-edge of the catalytically active Co_4P POM and a blank reference POM, $Na_9[A\text{-}PW_9O_{34}]$. The Co 3d electrons are not directly probed, rather the tungstate ligands surrounding the Co metal site are examined. Ligand effects on the metal site have been reported to play an integral role in tuning stability and catalytic activity, especially in the CoPOM complexes. [104] Fig. B.2 shows the XAS gives no shift in the rising O K-edge and minimal differences but RIXS is sensitive to the cobalt core and a notable change is observed. There is a 0.6 eV shift in the emission edge when $E_i \sim 540$ eV. This shift suggests that the Co_4P POM has a deeper (lower) valence band edge, resulting in a possibly higher potential to oxidize water. The Co-O core modifies the W-O distances in the tungstate ligands which moves the valence band edge. A lower $d-d$ transition from significant metal-oxygen charge transfer has been connected to greater catalytic activity. [208] These preliminary results show that a combination of RIXS and O K-edge XAS is a more sensitive X-ray technique to isolate the important electronic structure parameters affecting catalysis.

Bibliography

(1) IEA *World Energy Outlook 2010*; tech. rep.

(2) NOAA; tech. rep.; National Centers for Environmental Information, 2015.

(3) Lewis, N.; Nocera, D. Powering the Plant: Chemical Challenges in Solar Energy Utilization. *Proc. Natl. Acad. Sci. U.S.A.* **2006**, *103*, 15729–15735.

(4) Fujishima, A.; Honda, K. Electrochemical Photolysis of Water at a Semiconductor Electrode. *Nature* **1972**, *238*, 37–38.

(5) Yoneyama, H.; Sakamoto, H.; Tamura, H. A Photo-electrochemical Cell with Production of Hydrogen and Oxygen by a Cell Reaction. *Electrochim. Acta* **1975**, *20*, 341–345.

(6) Kainthla, R.; Zelenay, B.; Bockris, J. Significant Efficiency Increase in Self-Driven Photoelectrochemical Cell for Water Photoelectrolysis. *J. Electrochem. Soc.* **1987**, *134*, 841–845.

(7) Licht, S.; Wang, B.; Mukerji, S.; Soga, T.; Umeno, M.; Tributsch, H. Efficient Solar Water Splitting Exemplified by RuO_2-Catalyzed AlGaAs/Si Photoelectrolysis. *J. Phys. Chem. B* **2000**, *104*, 8920–8924.

(8) Nakamura, A.; Ota, Y.; Koike, K.; Hidaka, Y.; Nishioka, K.; Sugiyama, M.; Fujii, K. A 24.4% Solar to Hydrogen Energy Conversion Efficiency by Combining Concentrator Photovoltaic Modules and Electrochemical Cells. *Appl. Phys. Exp.* **2015**, *8*, 107101.

(9) Shockley, W.; Queisser, H. Detailed Balance Limit of Efficiency of *p*-*n* Junction Solar Cells. *J. Appl. Phys.* **1961**, *32*, 510–519.

(10) Harriman, A.; Pickering, I. J.; Thomas, J. M.; Christensen, P. A. Metal Oxides as Heterogeneous Catalysts for Oxygen Evolution under Photochemical Conditions. *J. Chem. Soc., Faraday Trans. 1* **1988**, *84*, 2795–2806.

(11) Elizarova, G.; Zhidomirov, G.; Parmon, V. Hydroxides of Transition Metals as Artificial Catalysts for Oxidation of Water to Dioxygen. *Catal. Today* **2000**, *58*, 71–88.

(12) Dau, H.; Limberg, C.; Reier, T.; Risch, M.; Roggan, S.; Strasser, P. The Mechanism of Water Oxidation: From Electrolysis via Homogeneous to Biological Catalysis. *Chem. Cat. Chem.* **2010**, *2*, 724–761.

(13) Brimblecombe, R.; Dismukes, G.; Swiegers, G.; Spiccia, L. Molecular Water-Oxidation Catalysts for Photoelectrochemical Cells. *Dalton Trans.* **2009**, 9374–9384.

(14) Townsend, T., *Inorganic Metal Oxide Nanocrystal Photocatalysts for Solar Fuel Generation from Water*; Springer: Heidelberg, 2014.

(15) Zhang, M.; Frei, H. Towards a Molecular Level Understanding of the Multi-Electron Catalysis of Water Oxidation on Metal Oxide Surfaces. *Catal. Lett.* **2015**, *145*, 420–435.

(16) Takashima, T.; Hashimoto, K.; Nakamura, R. Mechanisms of pH-Dependent Activity for Water Oxidation to Molecular Oxygen by MnO_2 Electrocatalysts. *J. Am. Chem. Soc.* **2011**, *134*, 1519–1527.

(17) Li, Y.-F.; Liu, Z.-P.; Liu, L.; Gao, W. Mechanism and Activity of Photocatalytic Oxygen Evolution on Titania Anatase in Aqueous Surroundings. *J. Am. Chem. Soc.* **2010**, *132*, 13008–13015.

(18) Zhang, Y.; Zhang, H.; Ji, H.; Ma, W.; Chen, C.; Zhao, J. Pivotal Role and Regulation of Proton Transfer in Water Oxidation on Hematite Photoanodes. *J. Am. Chem. Soc.* **2016**, *138*, 2705–2711.

(19) Herlihy, D.; Waegele, M.; Chen, X.; Pemmaraju, S.; Predergast, D.; Cuk, T. Uncovering the Oxyl Radical of Photocatalytic Water Oxidation by its Sub-Surface Vibration. *Nat. Chem.* **2016**, accepted.

(20) Zhang, M.; de Respinis, M.; Frei, H. Time-Resolved Observations of Water Oxidation Intermediates on a Cobalt Oxide Nanoparticle Catalyst. *Nat. Chem.* **2014**, *6*, 362–367.

(21) Surendranath, Y.; Kanan, M.; Nocera, D. Mechanistic Studies of the Oxygen Evolution Reaction by a Cobalt-Phosphate Catalyst at Neutral pH. *J. Am. Chem. Soc.* **2010**, *132*, 16501–16509.

(22) Wang, H.-Y.; Hung, S.-F.; Chen, H.-Y.; Chan, T.-S.; Chen, H.; Liu, B. In Operando Identification of Geometrical-Site-Dependent Water Oxidation Activity of Spinel Co_3O_4. *J. Am. Chem. Soc.* **2016**, *138*, 36–39.

(23) Bediako, D.; Surendranath, Y.; Nocera, D. Mechanistic Studies of the Oxygen Evolution Reaction Mediated by a Nickel-Borate Thin Film Electrocatalyst. *J. Am. Chem. Soc.* **2013**, *135*, 3662–3674.

(24) AlOtaibi, B.; Fan, S.; Vanka, S.; Kibria, M.; Mi, Z. A Metal-Nitride Nanowire Dual-Photoelectrode Device for Unassisted Solar-to-Hydrogen Conversion under Parallel Illumination. *Nano Lett.* **2015**, *15*, 6821–6828.

(25) Wang, D.; Pierre, A.; Kibria, M.; Cui, K.; Han, X.; Bevan, K.; Guo, H.; Paradis, S.; Hakima, A.-R.; Mi, Z. Wafer-Level Photocatalytic Water Splitting on GaN Nanowire Arrays Grown by Molecular Beam Epitaxy. *Nano Lett.* **2011**, *11*, 2353–2357.

(26) Li, B.; Zhao, J.; Onda, K.; Jordan, K.; Yang, J.; Petek, H. Ultrafast Interfacial Proton-Coupled Electron Transfer. *Science* **2006**, *311*, 1436–1440.

(27) Ashcroft, N.; Mermin, N., *Solid State Physics*, 1st; Saunders College: 1976.

(28) Luo, W.; Liu, B.; Li, Z.; Xie, Z.; Chen, D.; Zou, Z.; Zhang, R. Stable Response to Visible Light of InGaN Photoelectrodes. *Appl. Phys. Lett.* **2008**, *92*, 262110–3.

(29) Maeda, K.; Domen, K. Solid Solution of GaN and ZnO as a Stable Photocatalyst for Overall Water Splitting under Visible Light. *Chem. Mater.* **2010**, *22*, 612–623.

(30) Kanan, D.; Carter, E. Band Gap Engineering of MnO via ZnO Alloying: A Potential New Visible-Light Photocatalysts. *J. Phys. Chem. C* **2012**, *116*, 9876–9887.

(31) Kibria, M.; Zhao, S.; Chowdhury, F.; Wang, Q.; Nguyen, H.; Trudeau, M.; Guo H.and Mi, Z. Tuning the Surface Fermi Level on p-Type Gallium Nitride Nanowires for Efficient Overall Water Splitting. *Nat. Commun.* **2014**, *5*, 3825–6.

(32) Memming, R., *Semiconductor Electrochemistry*; Wiley-VCH: Weinheim, 2008.

(33) Scherrer, P. Bestimmung der Grösse und der inneren Struktur von Kolloidteilchen mittels Röntgenstrahlen. *Nachr. Ges. Wiss. Göttingen* **1918**, *26*, 98–100.

(34) Nozik, A.; Memming, R. Physical Chemistry of Semiconductors-Liquid Interfaces. *J. Phys. Chem.* **1996**, *100*, 13061–13078.

(35) Hodes, G., *Electrochemistry of Nanomaterials*; Wiley-VCH: Weinheim, 2001.

(36) Bard, A.; Faulkner, L., *Electrochemical Methods Fundamentals and Applications*, 2nd; John Wiley and Sons Ltd.: New York City, New York, 2002.

(37) Uosaki, K.; Kita, H. Effects of the Helmholtz Layer Capacitance on the Potential Distribution at Semiconductor/Electrolyte Interface and the Linearity of the Mott-Schottky Plot. *J. Electrochem. Soc.* **1983**, *130*, 895–897.

(38) Seo, M.; Dayeh, S.; Picraux, S.; Taylor, A.; Prasankumar, R. Mapping Carrier Diffusion in Single Silicon Core-Shell Nanowires with Ultrafast Optical Microscopy. *Nano Lett.* **2012**, *12*, 6334–6338.

(39) Le Formal, F.; Tétreault, N.; Cornuz, M.; Moehl, T.; Grätzel, M.; Sivula, K. Passivating Surface States on Water Splitting Hematite Photoanodes with Alumina Overlayers. *Chem. Sci.* **2011**, *2*, 737–743.

(40) Siripala, W.; Tomkiewicz, M. Interactions Between Photoinduced and Dark Charge Transfer Across n-TiO_2-Aqueous Electrolyte Interface. *J. Electrochem. Soc.* **1982**, *129*, 1240–1245.

(41) Nagasubramanian, G.; Wheeler, B.; Fan, F.-R.; Bard, A. XLII. Evidence for Fermi Level Pinning from Shifts in the Flatband Potential of p-Type Silicon in Acetonitrile Solutions with Different Redox Couples. *J. Electrochem. Soc.* **1982**, *129*, 1742–1745.

(42) Bockris, J.; Khan, S., *Surface Electrochemistry: A Molecular Level Approach*, 2nd; Plenum Press: New York City, New York, 1993, pp 59–202.

(43) Cardon, F.; Gomes, W. On the Determination of the Flat-Band Potential of a Semiconductor in Contact with a Metal or an Electrolyte from the Mott-Schottky Plot. *J. Phys. D. Appl. Phys.* **1978**, *11*, L63–L67.

(44) Oskam, G.; Hoffmann, P.; Schmidt, J.; Searson, P. Energetics and Kinetics of Surface States at n-Type Silicon Surfaces in Aqueous Fluoride Solutions. *J. Phys. Chem.* **1996**, *100*, 1801–1806.

(45) Jiao, F.; Frei, H. Nanostructured Cobalt Oxide Clusters in Mesoporous Silica as Efficient Oxygen-Evolving Catalysts. *Angew. Chem. Int. Ed.* **2009**, *48*, 1841–1844.

(46) Cherepy, N. J.; Liston, D. B.; Lovejoy, J. A.; Deng, H.; Zhang, J. Z. Ultrafast Studies of Photoexcited Electron Dynamics in γ- and α-Fe_2O_3 Semiconductor Nanoparticles. *J. Phys. Chem. B* **1998**, *102*, 770–776.

(47) He, Y.; Miao, Y.; Li, C.; Wang, S.; Cao, L.; Xie, S.; Yang, G.; Zou, B.; Burda, C. Size and Structure Effect on Optical Transitions of Iron Oxide Nanocrystals. *Phys. Rev. B* **2005**, *71*, 125411–9.

(48) Fan, H. M.; You, G. J.; Li, Y.; Zheng, Z.; Tan, H. R.; Shen, Z. X.; Tang, S. H.; Feng, Y. P. Shape-Controlled Synthesis of Single-Crystalline Fe_2O_3 Hollow Nanocrystals and Their Tunable Optical Properties. *J. Phys. Chem. C* **2009**, *113*, 9928–9935.

(49) Joly, A.; Williams, J.; Chambers, S.; Xiong, G.; Hess, W.; Laman, D. Carrier Dynamics in α-Fe_2O_3 (0001) Thin Films and Single Crystals Probed by Femtosecond Transient Absorption and Reflectivity. *J. Appl. Phys.* **2006**, *99*, 053521–6.

(50) Bauer, C.; Boschloo, G.; Mukhtar, E.; Hagfeldt, A. Ultrafast Relaxation Dynamics of Charge Carriers Relaxation in ZnO Nanocrystalline Thin Films. *Chem. Phys. Lett.* **2004**, *387*, 176–181.

(51) Huang, Z.; Lin, Y.; Xiang, X.; Rodríguez-Córdoba, W.; McDonald, K.; Hagen, K.; Choi, K.-S.; Brunschwig, B.; Musaev, D.; Hill, C.; Wang, D.; Lian, T. In Situ Probe of Photocarrier Dynamics in Water-Splitting Hematite (α-Fe_2O_3) Electrodes. *Energy Environ. Sci.* **2012**, *5*, 8923–8926.

(52) Cooper, J. K.; Ling, Y.; Longo, C.; Li, Y.; Zhang, J. Z. Effects of Hydrogen Treatment and Air Annealing on Ultrafast Charge Carrier Dynamics in ZnO Nanowires Under In Situ Photoelectrochemical Conditions. *J. Phys. Chem. C* **2012**, *116*, 17360–17368.

(53) Matsuda, K.; Hirabayashi, I.; Kawamoto, K.; Nabatame, T.; Tokizaki, T.; Nakamura, A. Femtosecond Spectroscopic Studies of the Ultrafast Relaxation Process in the Charge-Transfer State of Insulating Cuprates. *Phys. Rev. B* **1994**, *50*, 4097–4101.

(54) Okamoto, H.; Miyagoe, T.; Kobayashi, K.; Uemura, H.; Nishioka, H.; Matsuzaki, H.; Sawa, A.; Tokura, Y. Photoinduced Transition from Mott Insulator to Metal in the Undoped Cuprates Nd_2CuO_4 and La_2CuO_4. *Phys. Rev. B* **2011**, *83*, 125102–10.

(55) Ren, Y. H.; Zhao, H. B.; Lupke, G.; Hong, C. S.; Hur, N. H.; Hu, Y. F.; Li, Q. Ultrafast Photoinduced Reflectivity Transients in Doped Manganite. *J. Chem. Phys.* **2004**, *121*, 436–440.

(56) Liu, X.; Moritomo, Y.; Nakamura, A.; Tanaka, H.; Kawai, T. Critical Behavior of a Photodisordered Spin System in Doped Manganite. *Phys. Rev. B* **2001**, *64*, 100401–4.

(57) Moulton, P. Spectroscopic and Laser Characteristics of Ti:Al_2O_3. *J. Opt. Soc. Am. B* **1986**, *3*, 125–133.

(58) Furube, A.; Asahi, T.; Masuhara, H.; Yamashita, H. Charge Carrier Dynamics of Standard TiO_2 Catalysts Revealed by Femtosecond Diffuse Reflectance Spectroscopy. *J. Phys. Chem. B* **1999**, *103*, 3120–3127.

(59) Herman, I. P., *Optical Diagnostics for Thin Film Processing*; Academic Press, Inc.: San Diego, CA, 1996; Chapter 9.

(60) McIntyre, J.; Aspnes, D. Differential Reflection Spectroscopy of Very Thin Surface Films. *Surf. Sci.* **1971**, *24*, 417–434.

(61) Iwakura, C.; Honji, A.; Tamura, H. The Anodic Evolution of Oxygen on Co_3O_4 Film Electrodes in Alkaline Solutions. *Electrochim. Acta* **1981**, *26*, 1319–1326.

(62) Rasiyah, P.; Tseung, A. A Mechanistic Study of Oxygen Evolution on Li-Doped Co_3O_4. *J. Electrochem. Soc.* **1983**, *130*, 365–368.

(63) Schumacher, L.; Holzhueter, I.; Hill, I.; Dignam, M. Semiconducting and Electrocatalytic Properties of Sputtered Cobalt Oxide Films. *Electrochim. Acta* **1990**, *35*, 975–984.

(64) Chen, J.; Wu, X.; Selloni, A. Electronic Structure and Bonding Properties of Cobalt Oxide in the Spinel Structure. *Phys. Rev. B* **2011**, *83*, 245204–7.

(65) Vaz, C.; Wang, H.-Q.; Ahn, C.; Henrich, V.; Baykara, M.; Schwendemann, T.; Pilet, N.; Albers, B.; Schwarz, U.; Zhang, L.; Zhu, Y.; Wang, J.; Altman, E. Interface and Electronic Characterization of Thin Epitaxial Co_3O_4 Films. *Surf. Sci.* **2009**, *603*, 291–297.

(66) The Powder Difffraction File #04-014-7748., Newtown Square, PA, 2012.

(67) Kim, K. J.; Park, Y. R. Optical Investigation of Charge-Transfer Transitions in Spinel Co_3O_4. *Solid State Commun.* **2003**, *127*, 25–28.

(68) Athey, P.; Urban III, F.; Tabet, M.; McGahan, W. Optical Properties of Cobalt Oxide Films Deposited by Spray Pyrolysis. *J. Vac. Sci. Technol. A* **1996**, *14*, 685–692.

(69) Cook, J.; van der Meer, M. The Optical Properties of Sputtered Co_3O_4 Films. *Thin Solid Films* **1986**, *144*, 165–176.

(70) Xu, X.-L.; Chen, Z.-H.; Li, Y.; Chen, W.-K.; Li, J.-Q. Bulk and Surface Properties of Spinel Co_3O_4 by Density Functional Calculations. *Surf. Sci.* **2009**, *603*, 653–658.

(71) Miedzinska, K.; Hollebone, B.; Cook, J. An Assigment of the Optical Absorption Spectrum of Mixed Valence Co_3O_4 Spinel Films. *J. Phys. Chem. Solids* **1987**, *48*, 649–656.

(72) Redmond, G.; O'Keeffe, A.; Burgess, C.; MacHale, C.; Fitzmaurice, D. Spectroscopic Determination of the Flatband Potential of Transparent Nanocrystalline Zinc Oxide Films. *J. Phys. Chem.* **1993**, *97*, 11081–11086.

(73) Rothenberger, G.; Fitzmaurice, D.; Grätzel, M. Spectroscopy of Conduction Band Electrons in Transparent Metal Oxide Semiconductor Films: Optical Determination of the Flatband Potential of Colloidal Titanium Dioxide Films. *J. Phys. Chem.* **1992**, *96*, 5983–5986.

(74) Enright, B.; Fitzmaurice, D. Spectroscopic Determination of Electron and Hole Effective Masses in a Nanocrystalline Semiconductor Film. *J. Phys. Chem.* **1996**, *100*, 1027–1035.

(75) Barroso, M.; Pendlebury, S. R.; Cowan, A. J.; Durrant, J. R. Charge Carrier Trapping, Recombination and Transfer in Hematite Water Splitting Photoanodes. *Chem. Sci.* **2013**, *4*, 2724–2734.

(76) Haßel, M.; Kuhlenbeck, H.; Freund, H.-J.; Shi, S.; Freitag, A.; Staemmler, V.; Lütkehoff, S.; Neumann, M. Electronic Surface States of CoO(100): An Electron Energy Loss Study. *Chem. Phys. Lett.* **1995**, *240*, 205–209.

(77) Gorschlüter, A.; Merz, H. Localized d-d Excitations in NiO(100) and CoO(100). *Phys. Rev. B* **1994**, *49*, 17293–17302.

(78) Wheeler, D. A.; Wang, G.; Ling, Y.; Li, Y.; Zhang, J. Z. Nanostructured Hematite: Synthesis, Characterization, Charge Carrier Dynamics, and Photoelectrochemical Properties. *Energy Environ. Sci.* **2012**, *5*, 6682–6702.

(79) Kronawitter, C. X.; Bakke, J. R.; Wheeler, D. A.; Wang, W.-C.; Chang, C.; Antoun, B. R.; Zhang, J. Z.; Guo, J.; Bent, S. F.; Mao, S. S.; Vayssieres, L. Electron Enrichment in 3d Transition Metal Oxide Hetero-Nanostructures. *Nano Letters* **2011**, *11*, 3855–3861.

(80) Yoshihara, T.; Katoh, R.; Furube, A.; Tamaki, Y.; Murai, M.; Hara, K.; Murata, S.; Arakawa, H.; Tachiya, M. Identification of Reactive Species in Photoexcited Nanocrystalline TiO_2 Films by Wide-Wavelength-Range (400-2500 nm) Transient Absorption Spectroscopy. *J. Phys. Chem. B* **2004**, *108*, 3817–3823.

(81) Lohner, A.; Woerner, M.; Elsaesser, T.; Kaiser, W. Picosecond Capture of Photoexcited Holes by Shallow Acceptors in *p*-type GaAs. *Phys. Rev. Lett.* **June 1992**, *68*, 3920–3923.

(82) Streetman, B.; Banerjee, S., *Solid State Electronic Devices*, 6th edition; Prentice Hall: Upper Saddle River, NJ, 2005.

(83) Tyagi, M.; Overstraeten, R. V. Minority Carrier Recombination in Heavily-Doped Silicon. *Solid State Electron.* **1983**, *26*, 577–597.

(84) Sundaram, S.; Mazur, E. Inducing and Probing Non-Thermal Transitions in Semiconductors using Femtosecond Laser Pulses. *Nat. Mater.* **2002**, *1*, 217–224.

(85) Khriplovich, L.; Kholopov, E.; Paukov, I. Heat Capacity and Thermodynamic Properties of Co_3O_4 from 5 to 307 K Low-Temperature Transition. *J. Chem. Thermodyn.* **1982**, *14*, 207–217.

(86) Singh, V.; Kosa, M.; Majhi, K.; Major, D. Putting DFT to the Test: A First-Principles Study of Electronic, Magnetic, and Optical Properties of Co_3O_4. *J. Chem. Theory Comput.* **2015**, *11*, 64–72.

(87) Qiao, L.; Xiao, H.; Meyer, H.; Sun, J.; Rouleau, C.; Puretzky, A.; Geohegan, D.; Ivanov, L.; Yoon, M.; Weber, W.; Biegalski, M. Nature of the Band Gap and Origin of the Electro-/Photo-activity of Co_3O_4. *J. Mater. Chem. C* **2013**, *1*, 4628–4633.

(88) Dash, W.; Newman, R. Intrinsic Optical Absorption in Single Crystal Germanium and Silicon at 77 K and 300 K. *Phys. Rev.* **1955**, *99*, 1151–1155.

(89) Kolelilat, G.; Levina, L.; Shukla, H.; Myrskog, S.; Hinds, S.; Pattantyus-Abraham, A.; Sargent, E. Stable Infrared Photovoltaics Based on Solution-Cast Colloidal Quantum Dots. *ACS Nano* **2008**, *2*, 833–840.

(90) De Trizio, L.; Buonsanti, R.; Schimpf, A.; Llordes, A.; Gamelin, D.; Simonutti, R.; Milliron, D. Nb-Doped Colloidal TiO_2 Nanocrystals with Tunable Infrared Absorption. *Chem. Mater.* **2013**, *25*, 3383–3390.

(91) Thimsen, E.; Biswas, S.; Lo, C.; Biswas, P. Predicting the Band Structure of Mixed Transition Metal Oxides: Theory and Experiment. *J. Phys. Chem. C* **2009**, *113*, 2014–2021.

(92) Garcia-Mota, M.; Vojvodic, A.; Metiu, H.; Man, I.; Su, H.; Rossmeisl, J.; Norskov, J. Tailoring the Activity for Oxygen Evolution Electrocatalysts on Rutile TiO_2(110) by Transition-Metal Substitution. *Chem. Cat. Chem.* **2011**, *3*, 1607–1611.

(93) Su, J.; Guo, L.; Bao, N.; Grimes, C. Nanostructured WO_3/$BiVO_4$ Heterojunction Films for Efficient Photoelectrochemical Water Splitting. *Nano Lett.* **2011**, *11*, 1928–1933.

(94) Lu, Z.; Wang, H.; Kong, D.; Yan, K.; Hsu, P.; Zheng, G.; Yao, H.; Liang, Z.; Sun, X.; Cui, Y. Electrochemical Tuning of Layered Lithium Transition Metal Oxides for Improvement of Oxygen Evolution Reaction. *Nat. Comm.* **2014**, *5*, 4345–7.

(95) Hardin, W.; Mefford, J.; Slanac, D.; Patel, B.; Wang, X.; Dai, S.; Zhao, X.; Ruoff, R.; Johnston, K.; Stevenson, K. Tuning the Electrocatalytic Activity of Perovskites through Active Site Variation and Support Interactions. *J. Phys. Chem. C* **2012**, *116*, 9876–9887.

(96) Liu, H.; More, R.; Grundmann, H.; Cui, C.; Erni, R.; Patzke, G. Promoting Photochemical Water Oxidation with Metallic Band Structures. *J. Am. Chem. Soc.* **2016**, *138*, 1527–1535.

(97) Liu, Y.; Wang, H.; Lin, D.; Liu, C.; Hsu, P.-C.; Liu, W.; Chen, W.; Cui, Y. Electrochemical Tuning of Olivine-Type Lithium Transition-Metal Phosphates as Efficient Water Oxidation Catalysts. *Energy Environ. Sci.* **2015**, *8*, 1719–1724.

(98) Gardner, G.; Go, Y.; Robinson, D.; Smith, P.; Hadermann, J.; Abakumov, A.; Greenblatt, M.; Dismukes, G. Structural Requirements in Lithium Cobalt Oxides for the Catalytic Oxidation of Water. *Angew. Chem., Int. Ed.* **2012**, *51*, 1616–1619.

(99) Kanan, M.; Nocera, D. In Situ Formation of an Oxygen-Evolving Catalysts in Neutral Water Containing Phosphate and Co^{2+}. *Science* **2008**, *321*, 1072–1075.

(100) Yin, Q.; Tan, J.; Besson, C.; Geletii, Y.; Musaev, D.; Kuznetsov, A.; Luo, Z.; Hardcastle, K.; Hill, C. A Fast Soluble Carbon-Free Molecular Water Oxidation Catalyst Based on Abundant Metals. *Science* **2010**, *328*, 342–345.

(101) Lv, H.; Song, J.; Geletii, Y.; Vickers, J.; Sumliner, J.; Musaev, D.; Kögerler, P.; Zhuk, P.; Bacsa, J.; Zhu, G.; Hill, C. An Exceptionally Fast Homogeneous Carbon-Free Cobalt-Based Water Oxidation Catalyst. *J. Am. Chem. Soc.* **2014**, *136*, 9268–9271.

(102) Kanan, M.; Yano, J.; Surendranath, Y.; Dincă, M.; Yachandra, V.; Nocera, D. Structure and Valency of a Cobalt-Phosphate Water Oxidation Catalyst Determined by In Situ X-ray Spectroscopy. *J. Am. Chem. Soc.* **2010**, *132*, 13692–13701.

(103) Schiwon, R.; Klingan, K.; Dau, H.; Limberg, C. Shining Light on Integrity of a Tetracobalt-Polyoxometalate Water Oxidation Catalyst by X-ray Spectroscopy Before and After Catalysis. *Chem. Commun.* **2014**, *50*, 100–102.

(104) Ohlin, C.; Harley, S.; McAlpin, J.; Hocking, R.; Mercado, B.; Johnson, R.; Villa, E.; Fidler, M.; Olmstead, M.; Spiccia, L.; Britt, R.; Casey, W. Rates of Water Exchange for Two Cobalt(II) Heteropolyoxotungstate Compounds in Aqueous Solution. *Chem. Eur. J.* **2011**, *17*, 4408–4417.

(105) De Groot, F.; Kotani, A., *Core Level Spectroscopy of Solids*, 1st ed.; CRC Press: Boca Raton, FL, 2008.

(106) Fuggle, J.; Martensson, N. Core-Level Binding Energies in Metals. *J. Electron Spectrosc. Relat. Phenom.* **1980**, *21*, 275–281.

(107) Quackenbush, N.; Tashman, J.; Mundy, J.; Sallis, S.; Paik, H.; Misra, R.; Moyer, J.; Guo, J.-H.; Fischer, D.; Woicik, J.; Muller, D.; Schlom, D.; Piper, L. Nature of the Metal Insulator Transition in Ultrathin Epitaxial Vanadium Dioxide. *Nano Lett.* **2013**, *13*, 4857–4861.

(108) Cotton, F., *Chemical Applications of Group Theory*, 3rd ed.; John Wiley & Sons, Inc.: College Station, TX, 1990.

(109) Lee, Y.; de Jong, M.; van der Wiel, W. Electronic Structure of Co^{2+} Ions in Anatase Co:TiO_2 in Relation to Heterogeneity and Structural Defects. *Phys. Rev. B* **2011**, *83*, 134404–5.

(110) Van Schooneveld, M.; Kurian, R.; Juhin, A.; Zhou, K.; Schlappa, J.; Strocov, V.; Schmitt, T.; de Groot, F. Electronic Structure of CoO Nanocrystals and a Single Crystal Probed by Resonant X-ray Emission Spectroscopy. *J. Phys. Chem. C* **2012**, *116*, 15218–15230.

(111) Liu, H.; Guo, J.; Yin, Y.; Augustsson, A.; Dong, C.; Nordgren, J.; Chang, C.; Alivisatos, P.; Thornton, G.; Ogletree, D.; Requejo, F.; de Groot, F.; Salmeron, M. Electronic Structure of Cobalt Nanocrystals Suspended in Liquid. *Nano Lett.* **2007**, *7*, 1919–1922.

(112) Bonhommeau, S.; Pontius, N.; Cobo, S.; Salmon, L.; de Groot, F.; Molnar, G.; Bousseksou, A.; Durr, H.; Eberhardt, W. Metal-to-Ligand and Ligand-to-Metal Charge Transfer in Thin Films of Prussian Blue Analogues Investigated by X-ray Absorption Spectroscopy. *Phys. Chem. Chem. Phys.* **2008**, *10*, 5882–5889.

(113) Cartier dit Moulin, C.; Villain, F.; Bleuzen, A.; Arrio, M.-A.; Sainctavit, P.; Lomenech, C.; Escax, V.; Baudelet, F.; Dartyge, E.; Gallet, J.-J.; Verdaguer, M. Photoinduced Ferrimagnetic Systems in Prussian Blue Analogues ${C^I}_x Co_4[Fe(CN)_6]_y$ (C_I = Alkali Cation). 2. X-ray Absorption Spectroscopy of the Metastable State. *J. Am. Chem. Soc.* **2000**, *122*, 6653–6658.

(114) Stavitski, E.; de Groot, F. The CTM4XAS Program for EELS and XAS Spectral Shape Analysis of Transition Metal L Edges. *Micron* **2010**, *41*, 687–694.

(115) De Groot, F.; Fuggle, J.; Thole, B.; Sawatzky, G. 2p X-ray Absorption of 3d Transition-Metal Compounds: An Atomic Multiplet Description Including the Crystal Field. *Phys. Rev. B* **1990**, *42*, 5459–5468.

(116) Cowan, R. Theoretical Calculations of Atomic Spectra Using Digital Computers. *J. Opt. Soc. Am.* **1968**, *58*, 808–818.

(117) Thole, B.; Van Der Laan, G.; Butler, P. Spin-Mixed Ground State of Fe Phthalocyanine and the Temperature-Dependent Branching Ratio in X-ray Absorption Spectroscopy. *Chem. Phys. Lett.* **1988**, *149*, 295–299.

(118) Eisebitt, S.; Böske, T.; Rubensson, J.-E.; Eberhardt, W. Determination of Absorption Coefficients for Concentrated Samples by Fluorescence Detection. *Phys. Rev. B* **1993**, *47*, 14103–14109.

(119) Tröger, L.; Arvanitis, D.; Baberschke, K.; Michaelis, H.; Grimm, U.; Zschech, E. Full Correction of the Self-Absorption in Soft-Fluorescence Extended X-ray-Absorption Fine Structure. *Phys. Rev. B* **1992**, *46*, 3283–3289.

(120) Glass, E.; Fielden, J.; Kaledin, A.; Musaev, D.; Lian, T.; Hill, C. Extending Metal-to-Polyoxometalate Charge Transfer Lifetimes: The Effect of Heterometal Location. *Chem. Eur. J.* **2014**, *20*, 4297–4307.

(121) Müller, A.; Dloczik, L.; Diemann, E.; Pope, M. A Cyclic Voltammetric Study of Mangano(II)undecatungstosilicate: An Illustrative Example of the Reduction, Protonation and Disproportionation Pathways of Transition Metal Substituted Heteropolytungstates in Aqueous Solution. *Inorg. Chimica Acta* **1997**, *257*, 231–239.

(122) Simmons, V. Heteropoly Tungstocobaltoates and Tungstocobaltiates Based on CoO_4 Tetrahedra: Magnetic Properties, Spectra, Chemistry, and Structures., Ph.D. Dissertation, Boston University, Boston, 1953.

(123) Hadjiev, V.; Iliev, M.; Vergilov, I. The Raman Spectra of Co_3O_4. *J. Phys. C: Solid State Phys.* **1988**, *21*, L199–201.

(124) Flipse, C.; Rouwelaar, C.; de Groot, F. Magnetic Properties of CoO Nanoparticles. *Eur. Phys. J. D* **1999**, *9*, 479–481.

(125) Underwood, J.; Kim, K.-J.; Lindau, I.; Pianetta, P.; Winick, H.; Williams, G.; Scofield, J.; Thompson, A., *X-Ray Data Booklet*; Center for X-Ray Optics Advanced Light Source: Berkeley, CA, 2009.

(126) Lee, Y.; de Jong, M.; Jansen, R. Magnetism and Heterogeneity of Co in Anatase Co:TiO_2 Magnetic Semiconductor. *Appl. Phys. Lett.* **2010**, *96*, 082506–3.

(127) Lussier, A.; Dvorak, J.; Idzerda, Y.; Shinde, S.; Ogale, S.; Venkatesan, T. XAS Characterization of Growth Parameter Effects for Pulsed Laser Deposited $Co_xTi_{1-x}O_{2-\delta}$ Films. *Phys. Scr.* **2005**, *T115*, 623–625.

(128) Wu, J.; Walukiewicz, W.; Yu, K.; Ager III, J.; Haller, E.; Lu, H.; Schaff, W. Small Band Gap Bowing in $In_{1-x}Ga_xN$ Alloys. *Appl. Phys. Lett.* **2002**, *80*, 921–923.

(129) Kato, H.; Ueda, K.; Kobayashi, M.; Kakihana, M. Photocatalytic Water Oxidation under Visible Light by Valence Band Controlled Oxynitride Solid Solutions $LaTaON_2$-$SrTiO_3$. *J. Mater. Chem. A* **2015**, *3*, 11824–11829.

(130) Pattrick, R.; Van Der Laan, G.; Henderson, M.; Kuiper, P.; Dudzik, E.; Vaughan, D. Cation Site Occupancy in Spinel Ferrites Studied by X-ray Magnetic Circular Dichroism: Developing a Method for Mineralogists. *Eur. J. Mineral.* **2002**, *14*, 1095–1102.

(131) Tuxen, A. et al. Size-Dependent Dissociation of Carbon Monoxide on Cobalt Nanoparticles. *J. Am. Chem. Soc.* **2013**, *135*, 2273–2278.

(132) Joseph, D.; Basu, S.; Jha, S.; Bhatacharyya, D. Chemical Shifts of K-X-ray Absorption Edges on Copper in Different Compounds by X-ray Absorption Spectroscopy (XAS) with Synchrotron Radiation. *Nucl. Instrum. Meth. Phys. Res. B* **2012**, *274*, 126–128.

(133) Cramer, S.; de Groot, F.; Ma, Y.; Chen, C.; Sette, F.; Kipke, C.; Eichhorn, D.; Chan, M.; Armstrong, W. Ligand Field Strengths and Oxidation States from Manganese L-Edge Spectroscopy. *J. Am. Chem. Soc.* **1991**, *113*, 7937–7940.

(134) Heijboer, W.; et al. In-Situ Soft X-ray Absorption of Over-Exchanged Fe/ZSM5. *J. Phys. Chem. B* **2003**, *107*, 13069–13075.

(135) Nesbitt, H.; Bancroft, G. High Resolution Core- and Valence-Level XPS Studies of the Properties (Structural, Chemical and Bonding) of Silicate Minerals and Glasses. *Rev. Mineral. Geochem.* **2014**, *78*, 271–329.

(136) Tanabe, Y.; Sugano, S. On the Absorption Spectra of Complex Ions II. *J. Phys. Soc. Jpn.* **1954**, *9*, 766–779.

(137) Sugano, S.; Tanabe, Y.; Kamimura, H., *Multiplets of Transition-Metal Ions in Crystals*; Academic Press: New York, 1970.

(138) Dawson, B. The Structure of the 9(18)-Heteropoly Anion in Potassium 9(18)-Tungstophosphate, $K_6(P_2W_{18}O_{62})\cdot 14H_2O$. *Acta Cryst.* **1953**, *6*, 113–126.

(139) Kobayashi, A.; Sasaki, Y. The Crystal Structure of α-Barium 12-Tungstosilicate, α-$Ba_2SiW_{12}O_{40}\cdot 16H_2O$. *Bull. Chem. Soc. Jpn.* **1975**, *48*, 885–888.

(140) Nolan, A.; Allen, C.; Burns, R.; Craig, D.; Lawrance, G. X-ray Structural Studies of $K_6[Co^{II}W_{12}O_{40}]16H_2O$ and $K_5[Co^{III}W_{12}O_{40}]16H_2O$ and Structural Trends Along the $[XW_{12}O_{40}]^{n-}$ Series, where X = P^V, Si^{IV}, Co^{III} and Co^{II}. *Aust. J. Chem.* **2000**, *53*, 59–66.

(141) Brown, G.; Noe-Spirlet, M.-R.; Busing, W.; Levy, H. Dodecatungstophosphoric Acid Hexahydrate, $(H_5O_2{}^+)_3(PW_{12}O_{40}{}^{3-})$. The True Structure of Keggin's 'Pentahydrate' from Single-Crystal X-ray and Neutron Diffraction Data. *Acta. Cryst. Sec. B* **1977**, *33*, 1038–1046.

(142) De Groot, F.; Hu, Z.; Lopez, M.; Kaindl, G.; Guillot, F.; Tronc, M. Differences Between L_3 and L_2 X-ray Absorption Spectra of Transition Metal Compounds. *J. Chem. Phys.* **1994**, *101*, 6570–6576.

(143) Tchougréeff, A.; Dronskowski, R. Nephelauxetic Effect Revisited. *Int. J. Quantum Chem.* **2009**, *109*, 2606–2621.

(144) Griffith, J., *The Theory of Transition-Metal Ions*; Cambridge University Press: Cambridge, 2009.

(145) Kautek, W.; Gerischer, H.; Tributsch, H. The Role of Carrier Diffusion and Indirect Optical Transitions in the Photoelectrochemical Behavior of Layer Type d-Band Semiconductors. *J. Electrochem. Soc.* **1980**, *127*, 2471–2478.

(146) Lin, Y.-G.; Hsu, Y.-K.; Basilio, A.; Chen, Y.-T.; Chen, K.-H.; Chen, L.-C. Photoelectrochemical Activity on Ga-Polar and N-Polar GaN Surfaces for Energy Conversion. *Opt. Express* **2014**, *22*, A21–A27.

(147) Ščajev, P.; Jarašiūnas, K.; Okur, S.; Özgür, Ü.; Morkoç, H. Carrier Dynamics in Bulk GaN. *J. Appl. Phys.* **2012**, *111*, 023702–8.

(148) Malinauskas, T.; Jarašiūnas, K.; Miasojedovas, S.; Juršenas, S.; Beaumont, B.; Gibart, P. Optical Monitoring of Nonequilibrium Carrier Lifetime in Freestanding GaN by Time-Resolved Four-Wave Mixing and Photoluminescence Techniques. *Appl. Phys. Lett.* **2006**, *88*, 202109–3.

(149) Sjodin, T.; Li, C.; Petek, H.; Dai, H. Ultrafast Transient Grating Scattering Studies of Carrier Dynamics at a Silicon Surface. *Chem. Phys.* **2000**, *251*, 205–213.

(150) Jarasiunas, K.; Lovergine, N. Characterisation of Bulk Crystals and Structures by Light-Induced Transient Grating Technique. *Mater. Sci. Eng.* **2002**, *B91-92*, 100–104.

(151) Hoffman, C.; Jarašiūnas, K.; Gerritsen, H.; Nurmikko, A. Measurement of Surface Recombination Velocity in Semiconductors by Diffraction from Picosecond Transient Free-Carrier Gratings. *Appl. Phys. Lett.* **1978**, *33*, 536–539.

(152) Kasinski, J.; Gomez-Jahn, L.; Faran, K.; Gracewski, S.; Dwayne Miller, R. Picosecond Dynamics of Surface Electron Transfer Processes: Surface Restricted Transient Grating Studies of the n-TiO_2/H_2O Interface. *J. Chem. Phys.* **1989**, *90*, 1253–1269.

(153) Morishita, T.; Hibara, A.; Sawada, T.; Tsuyumoto, I. Ultrafast Charge Transfer at TiO_2/SCN^- (aq) Interfaces Investigated by Femtosecond Transient Reflecting Grating Method. *J. Phys. Chem. B* **1999**, *103*, 5984–5987.

(154) Nakabayashi, S.; Komuro, S.; Aoyagi, Y.; Kira, A. Transient Grating Method Applied to Electron-Transfer Dynamics at a Semiconductor/Liquid Interface. *J. Phys. Chem.* **1987**, *91*, 1696–1698.

(155) Gomez-Jahn, L.; Min, L.; Dwayne Miller, R. In Situ Picosecond Studies of Surface Reaction Dynamics at GaAs(100) Interfaces. *Mol. Cryst. Liq. Cryst.* **1991**, *194*, 181–190.

(156) Wang, D.; Buontempo, J.; Li, Z.; Miller, R. Picosecond Surface Restricted Grating Studies of n-GaAs (100) Liquid Junctions. Evidence for Interfacial Charge Transfer Approaching Adiabatic Limits. *Chem. Phys. Lett.* **1995**, *232*, 7–15.

(157) Moharam, M.; Gaylord, T.; Magnusson, R.; Young, L. Holographic Grating Formation in Photorefractive Crystals with Arbitrary Electron-Transport Lengths. *J. Appl. Phys.* **1979**, *50*, 5642–5651.

(158) Govorkov, S.; Schröder, T.; Shumay, I.; Heist, P. Transient Gratings and 2nd-Harmonic Probing of the Phase-Transformation of a GaAs Surface under Femtosecond Laser Irradiation. *Phys. Rev. B* **1992**, *46*, 6864–6868.

(159) Rose, T.; Wilson, W.; Wäckerle, G.; Fayer, M. Gas Phase Dynamics and Spectroscopy Probed with Picosecond Transient Grating Experiments. *J. Chem. Phys.* **1987**, *86*, 5370–5391.

(160) Hyde, P.; Ediger, M. Rotational Dynamics of Anthracene and 9,10-Dimethylanthracene in Polyisoprene. *J. Chem. Phys.* **1990**, *92*, 1036–1044.

(161) Vauthey, E. Picosecond Transient Grating Study of the Reorientation Dynamics of Nile Red in Different Classes of Solvent. *Chem. Phys. Lett.* **1993**, *216*, 530–536.

(162) Goodno, G.; Dadusc, G.; Miller, R. Ultrafast Heterodyne-Detected Transient-Grating Spectroscopy Using Diffractive Optics. *J. Opt. Soc. Am. B* **1998**, *15*, 1791–1794.

(163) Eichler, H.; Günter, P.; Pohl, D., *Laser-Induced Dynamic Gratings*; Springer-Verlag: Berlin, 1986.

(164) Xu, Q.-H.; Ma, Y.-Z.; Fleming, G. Heterodyne Detected Transient Grating Spectroscopy in Resonant and Non-Resonant Systems Using a Simplified Diffractive Optics Method. *Chem. Phys. Lett.* **2001**, *338*, 254–262.

(165) Gedik, N.; Orenstein, J. Absolute Phase Measurement in Heterodyne Detection of Transient Gratings. *Opt. Lett.* **2004**, *29*, 2109–2111.

(166) Scherer, N.; Carlson, R.; Matro, A.; Du, M.; Ruggiero, A.; Romero-Rochin, V.; Cina, J.; Fleming, G.; Rice, S. Fluorescence-Detected Wave Packet Interferometer: Time Resolved Molecular Spectroscopy with Sequences of Femtosecond Phase-Locked Pulses. *J. Chem. Phys.* **1991**, *95*, 1487–1511.

(167) Strauss, J.; Hundhausen, M.; Ley, L. An Optical Heterodyne Experiment for Sensitive Detection of Laser Induced Photocarrier Gratings Iin Semiconductors. *Appl. Phys. Lett.* **1996**, *69*, 875–877.

(168) Fujii, K.; Ohkawa, K. Photoelectrochemical Properties of p-Type GaN in Comparison with n-Type GaN. *Jap. J. Appl. Phys.* **2005**, *44*, L909–L911.

(169) Fujii, K.; Ohkawa, K. Hydrogen Generation from Aqueous Water using n-GaN by Photoassisted Electrolysis. *Phys. Stat. Sol. C* **2006**, *3*, 2270–2273.

(170) Ono, M.; Fujii, K.; Ito, T.; Iwaki, Y.; Hirako, A.; Yao, T.; Ohkawa, K. Photoelectrochemical Reaction and H_2 Generation at Zero Bias Optimized By Carrier Concentration of n-Type GaN. *J. Chem. Phys.* **2007**, *126*, 054708–6.

(171) Waki, I.; Cohen, D.; Lal, R.; Mishra, U.; DenBaars, S.; Nakamura, S. Direct Water Photoelectrolysis with Patterned n-GaN. *Appl. Phys. Lett.* **2007**, *91*, 093519–3.

(172) Kibria, M.; Nguyen, H.; Cui, K.; Zhao, S.; Liu, D.; Guo, H.; Trudeau, M.; Paradis, S.; Hakima, A.-R.; Mi, Z. One-Step Overall Water Splitting under Visible Light Using Multiband InGaN/GaN Nanowire Heterostructures. *ACS Nano* **2013**, *7*, 7886–7893.

(173) Hwang, Y.; Wu, C.; Hahn, C.; Jeong, H.; Yang, P. Si/InGaN Core/Shell Hierarchical Nanowire Arrays and their Photoelectrochemical Properties. *Nano Lett* **2012**, *12*, 1678–1682.

(174) Dahal, R.; Pantha, B.; Li, J.; Lin, J.; Jiang, H. Realizing InGaN Monolithic Solar-Photoelectrochemical Cells for Artificial Photosynthesis. *Appl. Phys. Lett.* **2014**, *104*, 143901–4.

(175) Kim, S.; Ebaid, M.; Kang, J.-H.; Ryu, S.-W. Improve Efficiency and Stability of GaN Photoanode in Photoelectrochemical Water Splitting by NiO Cocatalyst. *Appl. Surf. Sci.* **2014**, *305*, 638–641.

(176) Huygens, I.; Strubbe, K.; Gomes, W. Electrochemistry and Photoetching of n-GaN. *J. Electrochem. Soc.* **2000**, *147*, 1797–1802.

(177) Tseng, W.; van Dorp, D.; Lieten, R.; Vereecken, P.; Borghs, G. Anodic Etching of n-GaN Epilayer into Porous GaN and Its Photoelectrochemical Properties. *J. Phys. Chem. C* **2014**, *118*, 29492–29498.

(178) Fujii, K.; Karasawa, T.; Ohkawa, K. Hydrogen Gas Generation by Splitting Aqueous Water Using n-Type GaN Photoelectrode with Anodic Oxidation. *Jap. J. Appl. Phys.* **2005**, *44*, L543–L545.

(179) Huygens, I.; Theuwis, A.; Gomes, W.; Strubbe, K. Photoelectrochemical Reactions at the n-GaN Electrode in 1 M H_2SO_4 and in Acidic Solutions Containing Cl^- Ions. *Phys. Chem. Chem. Phys.* **2002**, *4*, 2301–2306.

(180) Li, M.; Luo, W.; Liu, B.; Zhao, X.; Li, Z.; Chen, D.; Yu, T.; Xie, Z.; Zhang, R.; Zou, Z. Remarkable Enhancement in Photocurrent of $In_{0.20}Ga_{0.80}N$ Photoanode by Using an Electrochemical Surface Treatment. *Appl. Phys. Lett.* **2011**, *99*, 112108–3.

(181) Chakrapani, V.; Chandrashekhar, P.; Kash, K.; Anderson, A.; Sunkara, M.; Angus, J. Electrochemical Pinning of the Fermi Level: Mediation of Photoluminescence from Gallium Nitride and Zinc Oxide. *J. Am. Chem. Soc.* **2008**, *130*, 12944–12952.

(182) Schäfer, S.; Koch, A.; Cavallini, A.; Stutzmann, M.; Sharp, I. Charge Transfer Across the n-Type GaN-Electrolyte Interface. *J. Phys. Chem. C* **2012**, *116*, 22281–22286.

(183) Waegele, M.; Chen, X.; Herlihy, D.; Cuk, T. How Surface Potential Determines the Kinetics of the First Hole Transfer of Photo-Catalytic Water Oxidation. *J. Am. Chem. Soc.* **2014**, *136*, 10632–10639.

(184) De Gryse, R.; Gomes, W.; Cardon, F.; Vennik, J. On the Interpretation of Mott-Schottky Plots Determined at Semiconductor/Electrolyte Systems. *J. Electrochem. Soc.* **1975**, *122*, 711–712.

(185) Schetzina, J.; McKelvey, J. Ambipolar Transport of Electrons and Holes in Anisotropic Crystals. *Phys. Rev. B* **1970**, *2*, 1869–1874.

(186) Reshchikov, M.; Morkoç, H.; Park, S.; Lee, K. Yellow and Green Luminescence in a Freestanding GaN Template. *Appl. Phys. Lett.* **2001**, *78*, 3041–3043.

(187) Jarašiūnas, K.; Ščajev, P.; Nargelas, S.; Malinauskas, T.; Kato, M.; Ivakin, E.; Nesladek, M.; Haenen, K.; Özgür, Ü.; Morkoç, H. Recombination and Diffusion Processes in Polar and Nonpolar Bulk GaN Investigated by Time-Resolved Photoluminescence and Nonlinear Optical Techniques. *Mat. Sci. Forums* **2012**, *717-720*, 309–312.

(188) Chen, Y.-W.; Kuo, J.-L. Density Functional Study of the First Wetting Layer on the GaN (0001) Surface. *J. Phys. Chem. C* **2013**, *117*, 8774–8783.

(189) Ye, H.; Chen, G.; Niu, H.; Zhu, Y.; Shao, L.; Qiao, Z. Structures and Mechanisms of Water Adsorption on ZnO(0001) and GaN(0001) Surface. *J. Phys. Chem. C* **2013**, *117*, 15976–15983.

(190) Chen, Y.-W.; Du, Y.; Kuo, J.-L. Removal of Water Adsorbates on GaN Surfaces via Hopping Processes and with the Aid of a Pt_4 Cluster: An Ab Initio Study. *J. Phys. Chem. C* **2014**, *118*, 20383–20392.

(191) Bermudez, V.; Long, J. Chemisorption of H_2O on GaN(0001). *Surf. Sci.* **2000**, *450*, 98–105.

(192) Lorenz, P.; Gutt, R.; Haensel, T.; Himmerlich, M.; Schaefer, J.; Krischok, S. Interaction of GaN(0001)-2×2 Surfaces with H_2O. *Phys. Stat. Sol. C* **2010**, *7*, 169–172.

(193) Akimov, A.; Muckerman, J.; Prezhdo, O. Nonadiabatic Dynamics of Positive Charge During Photocatalytic Water Splitting on GaN(10-10) Surface: Charge Localization Governs Splitting Efficiency. *J. Am. Chem. Soc.* **2013**, *135*, 8682–8691.

(194) Valentin, C.; Selloni, A. Bulk and Surface Polarons in Photoexcited Anatase TiO_2. *J. Phys. Chem. Lett.* **2011**, *2*, 2223–2228.

(195) Ambegaokar, V.; Halperin, B.; Langer, J. Hopping Conductivity in Disordered Systems. *Phys. Rev. B* **1971**, *4*, 2612–2620.

(196) Linnros, J.; Grivickas, V. Carrier-Diffusion Measurements in Silicon with a Fourier-Transient-Grating Method. *Phys. Rev. B* **1994**, *50*, 16943–16955.

(197) Kumakura, K.; Makimoto, T.; Kobayashi, N.; Hashizume, T.; Fukui, T.; Hasegawa, H. Minority Carrier Diffusion Length in GaN: Dislocation Density and Doping Concentration Dependence. *Appl. Phys. Lett.* **2005**, *86*, 052105–3.

(198) Scher, H.; Montroll, E. Anomalous Transit-Time Dispersion in Amorphous Solids. *Phys. Rev. B* **1975**, *12*, 2455–2477.

(199) Tiedje, T.; Rose, A. A Physical Interpretation of Dispersive Transport in Disordered Semiconductors. *Sol. Stat. Comm.* **1980**, *37*, 49–52.

(200) Yamakata, A.; Yoshida, M.; Kubota, J.; Osawa, M.; Domen, K. Potential-Dependent Recombination Kinetics of Photogenerated Electrons in n- and p-Type GaN Photoelectrodes Studied by Time-Resolved IR Absorption Spectroscopy. *J. Am. Chem. Soc.* **2011**, *133*, 11351–11357.

(201) Gutt, R.; Lorenz, P.; Tonisch, K.; Himmerlich, M.; Schaefer, J.; Krischok, S. Electronic Structure of GaN(0001)-2 × 2 Thin Films Grown by PAMBE. *Phys. Stat. Sol. (RRL)* **2008**, *2*, 212–214.

(202) Chen, R. Apparent Stretched-Exponential Luminescence Decay in Crystalline Solids. *J. Lumin.* **2003**, *102-103*, 510–518.

(203) Arkhipov, V.; Emel'yanova, E. Kinetics of the Diffraction Efficiency of Light-Induced Dynamic Gratings in Layers of Disordered Semiconductors. *Quantum Electron.* **1993**, *23*, 986–988.

(204) Kakalios, J.; Street, R.; Jackson, W. Stretched-Exponential Relaxation Arising from Dispersive Diffusion of Hydrogen in Amorphous Silicon. *Phys. Rev. Lett.* **1987**, *59*, 1037–1040.

(205) Dimitrijevic, N. M.; Saponjic, Z. V.; Bartels, D. M.; Thurnauer, M. C.; Tiede, D. M.; Rajh, T. Revealing the Nature of Trapping Sites in Nanocrystalline Titanium Dioxide by Selective Surface Modification. *J. Phys. Chem. B* **2003**, *107*, 7368–7375.

(206) De Groot, F.; Glatzel, P.; Bergmann, U.; van Aken, P.; Barrea, R.; Klemme, S.; Hävecker, M.; Knop-Gericke, A.; Heijboer, W.; Weckhuysen, B. 1s2p Resonant Inelastic X-ray Scattering of Iron Oxides. *J. Phys. Chem. B* **2005**, *109*, 20751–20762.

(207) Suntivich, J.; Hong, W.; Lee, Y.; Rondinelli, J.; Yang, W.; Goodenough, J.; Darbowski, B.; Freeland, J.; Shao-Horn, Y. Estimating Hybridization of Transition Metal and Oxygen States in Perovskites from O K-edge X-ray Absorption Spectroscopy. *J. Phys. Chem.* **2014**, *118*, 1856–1863.

(208) Khan, E.; Suljoti, E.; Singh, A.; Bonke, S.; Brandenburg, T.; Atak, K.; Golnack, R.; Spiccia, L.; Aziz, E. Electronic Structural Insights into Efficient MnOx Catalysts. *J. Mater. Chem. A* **2014**, *2*, 18199–18203.